Image-based Treatment Outcome Prediction and Intervention Guidance for Cardiovascular Diseases

Kristóf Ralovich

Technische Universität München
Department of Informatics
Chair for Computer Aided Medical Procedures and Augmented Reality

campar.cs.tum.edu

SIEMENS

Technische Universität München, Fakultät für Informatik
Chair for Computer-Aided Medical Procedures & Augmented Reality / I16

Image-based Treatment Outcome Prediction and Intervention Guidance for Cardiovascular Diseases

Kristóf Ralovich

Vollständiger Abdruck der von der Fakultät für Informatik der Technischen Universität München zur Erlangung des akademischen Grades eines

Doktors der Naturwissenschaften (Dr. rer. nat.)

genehmigten Dissertation.

Vorsitzende:	Prof. Dr.-Ing. Darius Burschka
Prüfer der Dissertation:	
1.	Prof. Dr. Nassir Navab
2.	Prof. Franjo Pernuš, Ph.D.

Die Dissertation wurde am 14.05.2018 bei der Technischen Universität München eingereicht und durch die Fakultät für Informatik am 19.09.2018 angenommen.

Abstract

Cardiovascular diseases (CVD) are among the leading causes of death worldwide. Clinical management of CVD seeks to improve patient outcomes and attempts to reduce treatment risks and costs throughout the whole life-cycle of the disorders, hence less-invasive and percutaneous techniques are continuously sought after.

This thesis is concentrating on two novel, image-based applications that aim to improve the existing clinical practice of CVD.

In the first application, an image-based blood pressure drop estimation method is proposed as a non-invasive alternative to the current gold standard invasive, catheter-based measurement. The framework combines statistical shape models of the arterial tree and a hemodynamic computational model of aortic blood flow. Robust machine learning is applied to fit model parameters to patient data. The introduced approach is evaluated on routine clinical images of human patients from multiple centers. Quantitative evaluation is performed in the context of the diagnosis, treatment planning (outcome prediction) and follow-up of coarctation of aorta. Experiments demonstrate that the workflow is fast and prediction is accurate and reproducible.

Second, a hybrid imaging system consisting of fluoroscopy and echocardiography is presented. Wherein we introduce a purely image-based method for peri-operative fusion of X-Ray fluoroscopy and volume intracardiac echocardiography (ICE). The proposed model-based registration algorithm allows 6 degrees of freedom pose estimation of catheters (equipped with radiopaque fiducials) from single X-Ray projection. The method is applied to a prototype ICE catheter whereby target registration error is investigated. Experiments performed on synthetic and porcine in-vivo data indicate initial feasibility. The complementary nature of the two modalities would potentially allow navigation and guidance during emerging cardiac interventions such as the therapy of structural heart disease. Furthermore, ICE carries the promise of removing sedation or general anesthesia associated with transesophageal echocardiography.

Zusammenfassung

Herz-Kreislauf-Erkrankungen gehören weltweit zu den häufigsten Todesursachen. Deswegen zielen klinische Anstrengungen kontinuierlich ab auf die Verbesserung der Therapieergebnisse dieser Erkrankungen, bei gleichzeitiger Reduktion der Risiken und Kosten entlang des gesamten Krankheitsverlaufs. Weniger invasive und perkutane Methoden stehen dabei im Mittelpunkt des Interesses. Vor diesem Hintergrund untersucht die vorliegende Arbeit zwei neuartige bildgebungsgestützte Verfahren. Mit beiden Verfahren wird eine Verbesserung der bestehenden klinischen Praxis für Herz-Kreislauf-Erkrankungen angestrebt.

Der erste Lösungsansatz stützt sich auf eine bildbasierte Methode zur Detektion von Blutdruckabfällen, als nicht-invasive Alternative zum derzeitigen Goldstandard der invasiven kathetrischen Messmethode. Dieser Ansatz kombiniert Statistische Formmodelle des arteriellen Gefäßbaums mit einem numerischen hämodynamischen Modell des Aortendurchflusses. Robustes Machine-Learning wird herangezogen, um die Modellparameter an die Patientendaten anzuschmiegen. Das eingeführte Verfahren wird auf Routineaufnahmen von Patienten verschiedener Kliniken getestet. Eine quantitative Evaluierung wird vorgenommen für die Bereiche Diagnose, Therapieplanung (Ergebnisvorhersage) und Nachsorge der Aortenisthmusstenose. Experimente zeigen die Schnelligkeit des Verfahrens und demonstrieren, dass seine Vorhersage genau und reproduzierbar ist.

Der zweite Lösungsansatz fußt auf hybrider Bildgebung aus Fluoroskopie und Echokardiographie. Hierzu wird eine rein bildbasierte Methode zur perioperativen Überlagerung von Röntgenfluoroskopie und intrakardialer Volumen-Echokardiographie (ICE) eingeführt. Anhand röntgendichter Landmarken auf dem Katheter schätzt der vorge-stellte modellbasierte Registrierungsalgorithmus die Katheterlage in sechs Freiheitsgraden aus einer einzigen Röntgenprojektion. Angewandt auf einen prototypischen ICE-Katheter, wird der Registrierungsfehler untersucht. Tests ausgeführt auf synthetischen und in-vivo-Schweinemodell-Bildern weisen auf eine grundsätzliche Tauglichkeit hin. Die sich ergänzenden beiden Bildmodalitäten sind so potenziell für die Lokalisierung und Navigation bei neu aufkommenden kardialen Engriffen geeignet - beispielsweise für die Behandlung struktureller Herzkrankheiten. Darüber hinaus hat eine so durchgeführte ICE das Potenzial, die Notwendigkeit einer Sedierung oder Vollnarkose bei transösophagealer Echokardiographie aufzuheben.

Acknowledgments

First of all, I would like to express my deepest gratitude to Prof. Nassir Navab for accepting me into his prestigious chair at TUM and allowing me freedom to undertake research. Also this incredible learning experience would have not been possible without Dorin Comaniciu of Siemens for generously funding my work for three years. I am immensely indebted to my advisers, Razvan Ionasec and Tobias Heimann. Razvan, thank you for trusting me after my internship. Tobias thank you for taking me under your wings! I would like to acknowledge Michal Sofka and Kevin S. Zhou for accepting me for an internship in Princeton setting the continuation of my studies in motion.

The CAMP group in Munich provided me a very welcoming atmosphere, I owe many thanks for the nice times we had with Tobias Reichl, Athanasios Karamalis, Stefan Holzer, Cedric Cagniart, Stefan Hinterstoisser, Christian Wachinger, Richard Brosig, José Gardiazabal, Mehmet Yigitsoy, Olivier Pauly, Jakob Vogel, Stefanie Demirci, Hauke Heibel, Nicolas Brieu, Loren Schwarz, Alexander Duliu, Ahmad Ahmadi and Peter Máday. Matthias Hanson, thank you for putting me in touch with a landlord in Munich, twice! I will never forget the soccer games in Englische Garten and the evening climbing sessions.

I feel privileged, that I could learn from the smartest colleagues at Siemens labs in Erlangen: María Costa, Ingmar Voigt, Dime Vitanovski, Sasa Grbic, Michael Kelm, late Alexey Tsymbal, Tim Horz, Martin Kramer, Dominik Neumann, Michael Wels and in Princeton: Bogdan Georgescu, Tommasso Mansi, Jingdan Zhang, Lucian Itu, Puneet Sharma, Viorel Mihalef, Ankur Kapoor, Rui Liao, Yefeng Zheng. Thank you Michael Sühling for supporting my application for the Ernst von Siemens stipendium. I owe Neil Birkbeck and Leslie Miller for lending me their bike, for letting me stay in their home in Princeton and for teaching me contemporary English!

Some of this work was financed by Siemens Healthcare business units who saw potential in the research collaboration: Matthias John (AX) and Estelle Camus (US). Thank you Markus Kaiser for helping with all matters related to C-arms.

I am very grateful for gaining direct clinical insights thanks to having the chance to work with cardiologists and cardiac surgeons: Giacomo Pongiglione (OPBG), Allen Everett (Johns Hopkins) and Thilo Noack (Herzzentrum Leipzig). It was fascinat-

ing the learn about the clinical potential of research work and the ability to attend procedures.

I am proud to have worked with some very bright students: Waldemar Krawtschuk, Matthias Fauconneau. I would also like to acknowledge Zhivko Dimitrov for his tireless annotation of X-Ray data sets.

Without the continuous help of Martina Hilla I do not think I would have been able to overcome the multitude of administrative tasks, especially during the first months in Germany! Great "thank you" goes to Tim Beyl and Robert Jakob for volunteering their time to review the draft of this thesis. I owe Harald Boschert for translating the abstract to German.

It was my girlfriend who supported me through always being the source of happiness and positivity and I will be always grateful for the memorable trips we have spent together. Thank you for listening to my thoughts even if they were negative!

Finally all this would not have been possible without my parents, who always wanted good for me, and my mother who supported my entrance exam preparation for university and my father for financial support during university years.

Contents

CHAPTER 1

Introduction

Today, we are living in a world characterized by increased life expectancy and aging population [140] where cardiovascular diseases (CVD) are the number one causes of human deaths [55, 138].

To address this phenomenon, medicine is shifting to become an interdisciplinary field of science. First, through research towards better understanding of the physiome (biology, diseases and pharmaceuticals) and second, through benefiting from health-care related innovative technical development (physics, electrical engineering and computer science). Continuous improvement of medical imaging and innovation in percutaneous therapies and devices are the two cornerstones of this progress.

1.1. Motivation

Recent statistics from 2013 [55] show that cardiovascular diseases (CVD) accounts for every third death in USA, and is the leading cause of death in Europe [138]. CVD consists of defects of the heart, diseases of the great vessels and the circulation. Patients effected by various types of CVD generally have shortened life expectancy, often require risky treatment and need costly medical care. In the USA alone, estimated cost of CVD in 2009 were: $312.6 billion, the highest cost among all disease groups [55]. Similar statistics from Europe state €195.5 billion on estimated economic costs of CVD [138] in 2012.

Besides loss of productivity and monetary aspects, CVD incurs significant social costs and difficulties for those affected. Often lifelong medical attention is required for patients.

CVD troubles such high numbers of the population [90], that inpatient operations and procedures increased 28% between the 2000-2010 decade [55]. This upsurge

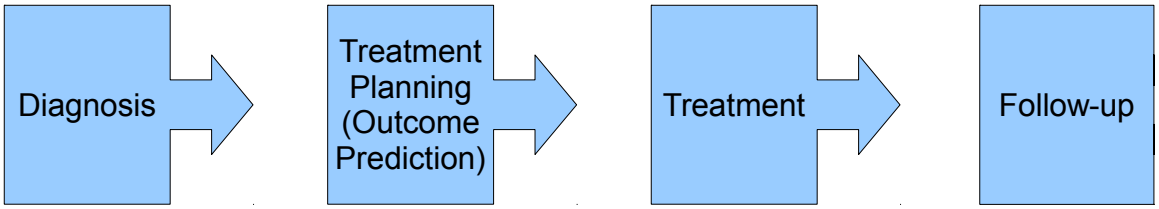

Figure 1.1.: Simplified management strategy including four phases of medical care for cardiovascular diseases.

was partly enabled by a revolution of wider applicability of minimally invasive, non-surgical treatment options.

Even though acquired form of CVD is considered a lifestyle disease, where prevention (changes in diet, physical activity, smoking) does help [207], forecast indicates increased CVD prevalence and costs [65, 158]. Effective strategy to CVD is needed to improve patient outcomes and control its projected burden.

The typical path CVD patients have to take, involves four phases of medical care (Fig. 1.1): diagnosis, treatment planning (outcome prediction), therapy and follow-up. The cycle of these steps may be repeated, depending on the response of the patient and severity, complexity and deterioration of heart defects.

Cardiovascular disease patients may be divided into two large groups.

The first is congenital heart defects (CHD) [72], covering patients born with heart structure abnormalities. Among congenital CVD, coarctation of the aorta (CoA) is the 5-6 most common defect lesion [36, 105]. Coarctation of aorta manifests itself as a stenosis (narrowing) of the aortic isthmus, creating a downstream blockage of the systemic circulation. Currently even the gold-standard for diagnostic severity assessment is an invasive method: blood pressure drop catheterization under ionizing X-Ray fluoroscopy. As CoA patients are predominantly treated at young age, non-invasive or less invasive alternative diagnostics procedures are of high importance.

The second subgroup is of patients with acquired CVD. Within this group a large portion of patients suffer from structural diseases of the heart (SHD) contracted at a later stage in life, such as valvular heart diseases or heart rhythm disorder. These patients are typically elderly, thus, certain medical treatment (such as open heart surgery) might pose high operative risk. Introduction of innovative prosthetic valves and closure devices allowed – starting with the highest-risk cohort – more and more of the patients to instead receive minimally invasive, percutaneous, catheter-based interventional therapy. During these operations direct view of the organs of interest is not possible and image-based guidance is needed. This led to development of "hybrid operating rooms" where a surgical suite is equipped with imaging instrument from a catheterization lab (C-arm mounted X-Ray fluoroscopy) and optionally a transesophageal echocardiography (TEE) machine. However TEE requires general anesthesia, and results in patient discomfort due to the large size of the echo transducer. Alternative echo imaging, that requires sedation only, could generally allow

faster discharge from the hospitals [8, 26, 92].

The above outlined reasons indicate, that less invasive options are sought after throughout the entire clinical management of CVD to reduce patient risk and procedure costs, enable faster interventions and improve effectiveness. It is also becoming clear, that the clinical management of CVD is increasingly relying on imaging, both outside and inside the operating room. This motivates the search for personalized methods involving less catheterization, reducing radiation and use of contrast agents and avoiding general anesthesia.

1.2. Objectives

Given the major trends presented in the previous section 1.1, this dissertation is focused on evolving all four stages of CVD health-care (Figure 1.1). This is demonstrated through two powerful, image-based, computer-aided applications.

As the first application (Chapter 3) we look at coarctation of aorta, a common congenital heart defect. We propose a non-invasive alternative method to the currently gold standard invasive measurement of blood pressure that is used for diagnostics and follow-up. Towards these goals, the following specific aims are pursued:

- Create a geometrical model of the aorta including the main branches of the aortic arch.
- Develop a robust method to estimate model parameters from routinely acquired non-invasive 3D MR images.
- Design a fast computational framework, coupling vessel geometry with hemodynamics to compute blood pressure conditions non-invasively *in-silico*.

The second application is aiming to propose a purely image-based, general anesthesia free guidance method for emerging beating heart (percutaneous off-pump) interventions (Chapter 4). The goal is to allow introduction of soft-tissue information in the traditionally X-Ray-based interventional navigation. The feasibility of this fused echo–X-Ray technique is investigated through the following objectives:

- Develop a fast and robust method to find and extract an echocardiography catheter from C-arm based X-Ray fluoroscopy images.
- Provide a registration approach of echocardiography and fluoroscopy for fused-image procedure guidance.
- Design an experimental setting to evaluate the accuracy of the registration method.

1.3. Challenges

To reach these goals, certain challenges have to be overcome. When proposing an alternative clinical method, it is desired that the new procedure is not excessive and minimizes introduction of demanding changes into existing clinical protocols and workflows.

In the context of the first application (non-invasive blood pressure estimation), the method should reduce invasiveness (less radiation, less catheterization). It should be robust and allow to use clinical images that match the quality of retrospective examinations, thus the methods needs to be general and able work on low resolution and noisy images, or images that are not capturing the best view of anatomy. Inter-patient and pathological variations of anatomy morphology should be robustly handled. Fast hemodynamic computations are desired, otherwise the method is difficult to incorporate into interactive clinical workflows. The method should be aiming to allow predictive, personalized use. Automation is sought after, to avoid manual parameter setting. Inside sterile environments (the operating theater) interaction is difficult and automated solutions are easier to accept.

During the second – intra-operative image fusion – part, different difficulties are to be addressed. Ideally the approach should reduce invasiveness (less use of contrast agent, avoidance of general anesthesia) and allow faster procedures through improved guidance. The method should allow registration of the two modalities from a single-shot of X-Ray view. The echocardiography catheter is small compared to the C-arm geometry. Fiducials are required to fit inside the rigid catheter tip. The fiducials may not increase the length of the catheter tip and should not interfere with the acoustic window. The method should be able to solve this ill-posed (close to collinear) problem and recover the catheter pose. The registration algorithm used for fusion should be real-time and ideally fully automatic.

1.4. Contributions

This dissertation attempts to advance the field with the above challenges in mind. The major contributions of this thesis along with the corresponding publications are summarized in the following two sections.

1.4.1. Non-invasive Blood Pressure Drop Estimation

Our aim is to minimize the invasiveness of blood pressure drop estimation. Covering the diagnosis, treatment planning and follow-up of coarctation of aorta (CoA) patients, we propose a fast, end-to-end workflow for non-invasive image-based hemodynamic CoA assessment. This includes robust arterial lumen/stent segmentation from MRI, that is suitable to make the (i) pre-operative diagnosis, (ii) follow-up stented CoA and to (iii) predict treatment outcomes through “virtual stenting”.

- **Define a statistical shape model of the geometry of the aorta and main branches.** The model is designed to be able to capture the shape of the aortic lumen, for both pathological, operated and healthy subjects. The geometry and shape are described in a hierarchy of coarse-to-fine details: the aortic root (Ro), aortic arch (Ar), walls of ascending- (AAo) and descending (DAo) aorta, the trunks of the brachiocephalic- (Br), left common carotid- (Lc) and left subclavian (Ls) arteries.

- **Introduce machine learning based parameter estimation of the model** (developed in previous step). Relying on volumetric image information (from standard cardio-thoracic examinations), model parameters are estimated in a Bayesian statistical inference framework to match patient-specific morphology [153, 199]. Robust, supervised machine learning based techniques are introduced for fast model estimation based on 3D images from various cardiac MRI protocols.

- **Parameterize a state-of-the-art hemodynamic circulation method** using the above aortic model and velocity encoded MR images, to allow fast and personalized hemodynamic computations, including estimation of blood pressure conditions. Coupling with both quasi-1D [153] and 3D [151, 156, 152] hemodynamic computations are investigated. The computational hemodynamic models are not developed as part of this thesis but were separately introduced by Itu and Sharma [84] and Mihalef [131, 130].

- **Design an experimental setting**, for qualitative analysis of non-invasively estimated and invasively measured blood pressure drop for coarctation of aorta (CoA) patients. Targeting three phases of CVD care: estimation for pre-operative (diagnostics), post-operative (follow-up) and "virtual stenting" (virtual treatment outcome prediction) we have evaluated our method [154] on retrospective data from 6 patients from multiple hospitals.

1.4.2. Peri-operative Image Fusion

In the context of image-based therapy guidance, a novel technique that does not require general anesthesia is devised. We introduce the first (to the best of our knowledge) purely image based peri-operative system to register intracardiac echocardiography (ICE) and X-Ray involving 6 degrees of freedom (DoF) pose recovery of an ICE catheter through the following:

- **Introduce a mathematical model of fiducials equipped ultrasound catheter.** The model is defined in the space of 2D projections of the catheter. Inside the catheter tip, the model describes the phased array (PHA) ultrasound transducer and 6 embedded ball marker fiducials [155].

- **Estimation of model parameters from interventional X-Ray images.** Parameters of the catheter model are estimated from single, interventional X-Ray projection images. Intra-operative applications require real-time performance of guidance algorithms, thus fast, machine learning based methods are used to discriminate background from devices. In addition, catheter-like hypotheses are robustly fused together with ball marker candidates to determine the true catheter.

- **Recover 3D pose of catheter with respect to X-Ray image,** to enable peri-operative registration (fusion) of intracardiac echo and X-Ray for procedure guidance [155]. Correspondence of extracted ball markers and perspective pose recovery of catheter model is solved in a joint formulation.

1.5. Thesis Overview and Reading Guidelines

Through two image-based applications, this thesis concentrates around improving all four steps in the life-cycle of CVD care (Figure 1.2). Based on the clinical, therapeutic and image analysis background introduced in Chapter 2, the two applications are described in chapters 3 and 4. These methodological chapters may be mostly independently read from one another. Chapter 5 concludes the thesis.

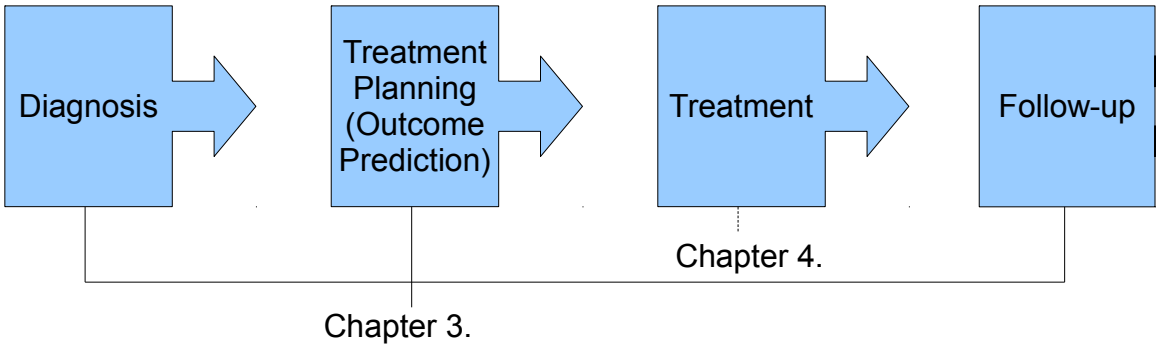

Figure 1.2.: Chapters 3 and 4 describe different phases of the life-cycle of CVD care and may be mostly independently read from one another. Chapter 3 proposes a method to be used in diagnosis, follow-up and treatment planning. Chapter 4 proposes a novel method for treatment.

A brief description of individual chapters included in this work is presented in the following.

Chapter 2: Background
In this chapter, we provide a brief introduction to the human circulatory system and prevalence of cardiovascular diseases. In particular congenital heart defects and structural heart diseases are reviewed together with current clinical practice for their diagnosis and treatment. Similarly, we review CVD related state-of-the-art medical procedures, devices and imaging equipment and their typical applications areas. Lastly an overview is provided on image analysis techniques (segmentation, image-based computations and registration/fusion) and applied machine learning that provide context for the following methodological chapters.

Chapter 3: Non-invasive Assessment of Aortic Coarctation for Diagnostics, Treatment Outcome Prediction and Follow-up
Coarctation of the aorta (CoA), is a congenital heart disease characterized by a abnormal narrowing of the proximal descending aorta. Severity of this pathology is quantified by the blood pressure drop ($\triangle P$) across the stenotic coarctation lesion. In order to evaluate the physiological significance of the pre-operative coarctation and to assess the post-operative results, the hemodynamic analysis is routinely performed

by measuring the blood pressure drop ($\triangle P$) across the coarctation site via invasive cardiac catheterization.

The focus of this chapter is to present an alternative, non-invasive measurement of blood pressure drop $\triangle P$ through the introduction of a fast, image-based workflow for personalized computational modeling of the CoA hemodynamics.

We propose an end-to-end system comprising of shape and computational models and their personalization setup using MR imaging. Supervised machine learning methods are employed to estimate model parameters based on imaging data. A fast, non-invasive method based on computational fluid dynamics (CFD) is discussed to estimate the pre- (diagnosis) and post-operative (follow-up) hemodynamics for coarctation patients. A virtual treatment (outcome prediction) method is investigated to assess the predictive power of our approach.

Chapter 4: Peri-operative Registration of X-Ray and ICE for Therapy Guidance

Hybrid imaging systems, consisting of fluoroscopy and echocardiography, are increasingly selected for intra-operative support of minimally invasive cardiac interventions. Intracardiac echocardiography (ICE) is an emerging modality with the promise of removing sedation or general anesthesia associated with transesophageal echocardiography (TEE).

We introduce a novel 6 degrees of freedom (DoF) pose estimation approach for catheters (equipped with radiopaque ball markers) in single X-Ray fluoroscopy projection and investigate the method's application to a prototype ICE catheter. Machine learning based catheter detection is implemented in a Bayesian hypothesis fusion framework, followed by refinement of ball marker locations through template matching. The $2D$-$3D$ image fusion task is formulated as a feature-based registration problem. Marker correspondence and $3D$ pose estimation are solved through iterative optimization of a least-squares type cost function.

The machine learning tools in this chapter build upon the methods introduced in Chapter 3.

Chapter 5: Conclusions

In the last chapter, the introduced methods are summarized. We reflect on the obtained results and their clinical relevance. For a truthful evaluation, limitations of the proposed techniques is discussed. Wider clinical applicability and required further validation is investigated.

CHAPTER 2

Background

2.1. Physiology, Pathology and Therapy

2.1.1. Human Cardiac Anatomy and Function

The heart is the central pump of blood flow, the key to circulation. The human heart is an approximately fist sized organ, built of heart muscle (endocardium and myocardium), surrounded by the sac of pericardium. The heart is located in the middle of the thorax (chest), behind the sternum, among the lungs and above the diaphragm. Its main function is to supply nutrients and gases through blood flow to the entire body.

The heart may be divided into two major parts, based on function: the left and right sides. The left side of the heart pumps oxygenated blood into the body (systemic circulation) to feed all tissue, while the right side collects oxygen poor blood - mostly through veins - and pushes it through the lungs (pulmonic circulation). Furthermore, each side of the heart consists of two cavities (the upper atria and lower ventricles) with heart valves regulating the flow at the entrance (atrioventricular valves) and outlet (semi-lunar valves) of the ventricles (see Figure 2.1a). The purpose of the regulation is to only allow antegrade flow and block retrograde flow.

Throughout its lifetime, the heart is repeating contraction (systole) and relaxation (diastole) phases to maintain the blood flow. The diastolic phase starts when the semi-lunar (aortic and pulmonic) valves close, followed by the isovolumetric relaxation of the ventricles, once the pressure inside the ventricles drops, the atrioventricular (mitral and tricuspid) valves open up to allow the blood to fill the ventricles from the atria. The last event of diastole is called atrial systole, when the atria contract to completely fill the ventricles. The atrioventricular valves close at this point, and

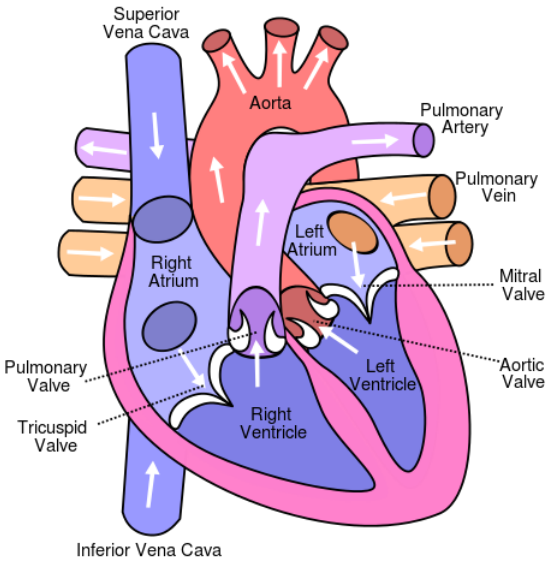

(a)

Figure 2.1.: Chambers, valves and in- and outlets of the heart (reproduced from [5]).

systole begins: the ventricular isovolumetric contraction starts to raise the blood pressure above that of the aorta and pulmonary artery. During the last (stroke) phase, the semi-lunar valves open, and the ventricular ejection pushes blood jets out of the heart. The pulsatile flow (pulse) is created by this periodic pumping into the arteries. Systematic activation of the heart contraction is driven by a regular electrical impulse originating from the sinus node. At rest, the average normal heart rate is around $60 - 80$ bpm, and the cardiac output (combined ejection of left and right sides) is approximately 5 L/min.

The aorta is the greatest vessel in the body, making the connection between the left ventricle of the heart and the systemic circulation. The average diameter of the ascending aorta is about $30 - 35$ mm in adults [119]. It goes above and descends posterior to (behind) the heart. All oxygenated blood is pumped through the aorta to supply the body tissue. The thoracic aorta has a characteristic inverted 'U' shape, divided into four parts: ascending aorta, aortic arch, aortic isthmus and descending aorta. The ascending aorta contains the coronary ostia and feeds the coronary arteries (and indirectly the myocardium) with blood, while the aortic arch usually has three main bifurcations: the supra-aortic arteries (SAoA) that supply the arms, neck and head. Typical arrangement of the SAoA is (along the flow of bloodstream) brachiocephalic trunk, left common carotid artery and left subclavian artery. The aortic isthmus is the part distal to the left subclavian bifurcation, connecting the arch with the descending aorta (see Figure 2.2a). The aorta further continues down the body, bifurcating into arteries to feed tissue of the whole body.

The walls of the aorta are built from elastic tissue types. During left ventricular

ejection, not all blood is pushed into the capillaries, but the aorta expands and stores the "surplus" volume. During diastole, the elastic vessel wall contracts, and this recoil is maintaining perfusion. This is called the windkessel effect and is shown in Figure 2.2b. The windkessel phenomena is damping the sharply fluctuating increase and decrease in blood pressure. The blood pressure is represented as a pair of numbers measuring the high (systolic) and low (diastolic) values, the normal values are in the 120/80 $mmHg$ range.

The veins close the loop of systemic circulation. These vessels collect oxygen poor blood from body tissues and deliver it back to the heart.

2.1.2. Congenital Heart Defects and Structural Heart Disease

Such a complex apparatus as the cardiovascular system has many different ways to malfunction, and a wide variety of disorders are documented. Among all cardiovascular diseases (CVD) we focus our investigation on congenital heart defects (CHD) and the field of structural heart disease (SHD). The umbrella term "structural heart disease" was coined only recently — in 1999 according to Steinberg et al. [183] — and SHD covers "non-coronary cardiac disease processes and related interventions".

With the advent and proliferation of various minimally invasive trans-catheter therapies the SHD population is growing. More patients and disorders become eligible for minimally invasive interventions. Thus, the prevalence of SHD is hard to accurately quantify. It may be described as the combined effect of congenital heart

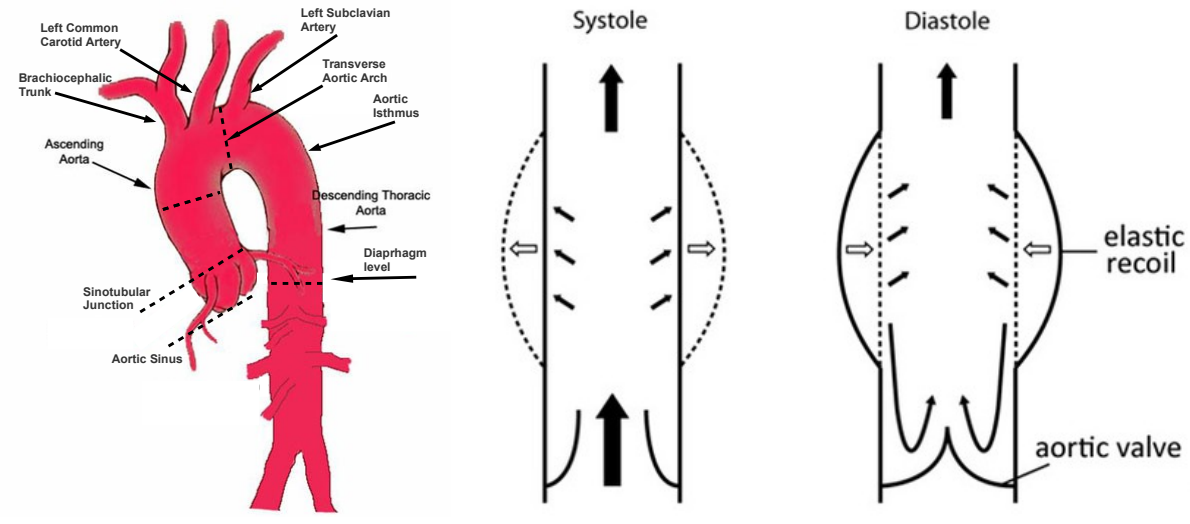

(a) (b)

Figure 2.2.: a) Anatomic regions of the thoracic aorta (reproduced from [4]). b) Windkessel effect of the elastic aortic walls (reproduced from [157]).

defects (CHD) and acquired non-coronary cardiac disorders [183]. The prevalence of the latter increases with age, and the elderly are the fastest growing subset of the SHD population. CHD is among the leading causes of birth-defect related deaths, affecting approximately 1 of 100 live births according to studies conducted in the USA [72], Europe [36] and Germany [105].

CHD and structural heart disease is rarely an individual condition, often multiple concomitant disorders are present. Many of these are abnormal connections between heart chambers as well as other blood vessels around the heart (e.g. aorta and pulmonary artery) [210, 28]. These abnormal connections may allow the mixture of unoxygenated and oxygenated blood, or may let oxygen poor blood to flow to the body instead of to the lungs, or allow oxygenated blood to flow to the pulmonic circulation instead of reaching the body. They reduce the efficiency of the pumping heart, and may also cause heart failure.

CHD and SHD are broad categories, where the most common examples of congenital heart defects (in infants and children) and structural cardiac diseases (in adults) include [183]:

- Heart valve defects. These may result in a narrowing of the valves (e.g. aortic stenosis, mitral valve stenosis, pulmonary valve stenosis), or a complete closure that obstructs normal blood flow. Bicuspid aortic valve (BAV) leaflets are the most common congenital aortic valve disease. Other valve defects include calcified or stenosed leaky valves that don't close properly thereby allowing retrograde blood flow. Such as mitral valve insufficiency (regurgitation with reduced coaptation area or prolapse) that may be caused by ruptured or elongated chordae tendineae. Repaired or replaced valves might not seal completely and allow paravalvular leaks to pass by.

- Defects in the walls between the atria and ventricles of the heart (atrial and ventricular septal defects, ASD and VSD, respectively). Holes or passageways between the heart's different cavities may allow abnormal intermixing of oxygenated and unoxygenated blood between the right and left sides of the heart or introduce altered structure of flow pattern. Similarly, patent foramen ovale (PFO) is a congenital shunt (hole) between the atria of the heart, that failed to close after birth. In adulthood septal rupture might develop.

- Patent ductus arteriosus (PDA) is a congenital disorder that allows blood to bypass the lungs, preventing oxygen from circulating throughout the body.

- Tetralogy of Fallot (ToF), a combination of four different heart defects that occur together at birth.

- Atrial fibrillation (AF) and left atrial appendage (LAA). AF is a sustained arrhythmia (irregular heartbeat) of the upper chambers (atria) of the heart. AF might create conditions in the appendage of the left atrium that prohibit

normal blood flow, and instead allow the pouch to be a source of thrombus (blood clot) formation. This carries the direct risk of thrombosis and arterial embolisms, and may lead to stroke. According to Möbius-Winkler et al. 90% of atrial fibrillation associated strokes are the result of emboli from the LAA [132].

- Coarctation of the aorta (CoA), detailed in the Section below.

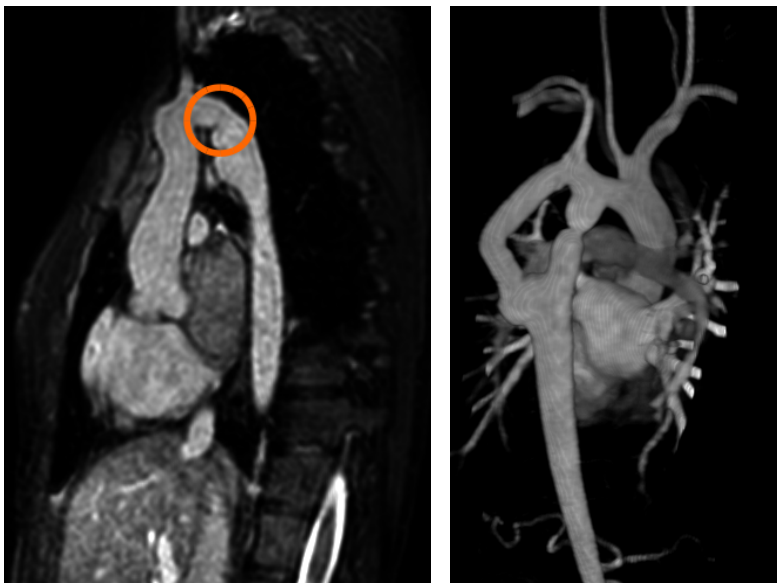

(a) (b)

Figure 2.3.: a) Coarctation of the aorta (CoA) as shown on 3D cardiac MR volume (circled); b) Volumetric reconstruction of MRI showing a pathological aortic isthmus, where a collateral bypass had developed around the narrowing of the CoA.

We pay particular interest to explain coarctation of aorta (CoA), as our method in Chapter 3 is aiming to propose a non-invasive method for quantitative characterization of blood pressure drop in this disease.

Coarctation of the aorta (CoA) is a congenital defect characterized by a severe narrowing of the aortic isthmus. CoA accounts for $5-8\%$ of the 8 of 1 000 congenital heart disease (that is $4-6$ of 10 000) live births [163, 162, 72] in the USA and an incidence of 3.6% (3.9 of 10 000) in Germany [105]. CoA is the fifth or sixth most common lesion in congenital heart disease (CHD) [189, 36] that still results in lower than average life expectancy for patients [202, 39, 98] due to hypertension, increased stroke risk, aneurysm development and early appearance of coronary artery disease (CAD).

The effect of CoA is a stenosis distal to the aortic arch (see Figure 2.3a), resulting in pathophysiological processes that restrict the circulation of oxigenated blood

through the narrowing. This necessitates increased cardiac output and may lead to left ventricular (LV) hypertrophy. Generally CoA results in persistent upper body hypertension and lower body hypotension.

Unrecognized or untreated coarctation may result in the development of collateral bypass vessels to maintain downstream perfusion, as illustrated in Figure 2.3b.

2.1.3. Diagnostic and Therapeutic Procedures

Generally three therapeutic options have been developed for the treatment of the congenital heart defects and in the context of structural heart disease: drug therapy, surgery and percutaneous intervention.

The clinical decision making for CHD and SHD starts with risk stratification activities. The New York Heart Association Functional Classification is used to categorize patient symptoms. In order to quantitatively manage the inherent challenges pertaining to comorbidities, various risk estimation system have been devised such as the EuroSCORE [167], STS-Score [68].

As there exist no medications specific to curing these diseases. Current drugs enable mostly stabilization of the condition and are limited to treating collateral symptoms in mild and very high risk patients [168, 132]: anti-coagulation (warfarin), antithrombotic therapy (dabigatran), heart rate ($\beta-$blockers) and rhythm control (amiodarone) and blood pressure regulation.

Patients born with CHD and CoA require lifelong medical care [189]. Depending on the severity of the case, age, size, general health and risk level of the patient the management strategy resorts to either open heart surgery, or – in patients where surgery is denied due to carrying high operative risk – percutaneous, minimally invasive procedures (MIP) are selected. In some cases invasive catheterization is required already for diagnostics (e.g. blood pressure measurement).

Surgery

Several different congenital heart defects are recognized and treated early in infancy. Traditionally, invasive open heart surgery is performed. In certain cases heart replacement is the last option with the highest likelihood of complications and operative risk.

During a cardiac surgery the cardiac region is accessed through a large, surgical opening of the chest (sternotomy or thoractomy). The patient might need to be connected to cardiopulmonary bypass (heart-lung machine or pump) to take over the function of the pumping heart and lungs. During surgery holes may be closed with stitches or a patch, location and form of vessels could be re-configured and arteries or valves could be opened wider. Sometimes multiple surgeries and interventions are needed to correct more complex anomalies.

The surgical repair options [11, 69, 143] of CoA include various forms of invasive aortoplasty. The first surgical correction was performed in 1944 in Sweden by Crafoord and Nylin [23] introducing the end-to-end anastomosis technique (see Figure 2.4a)

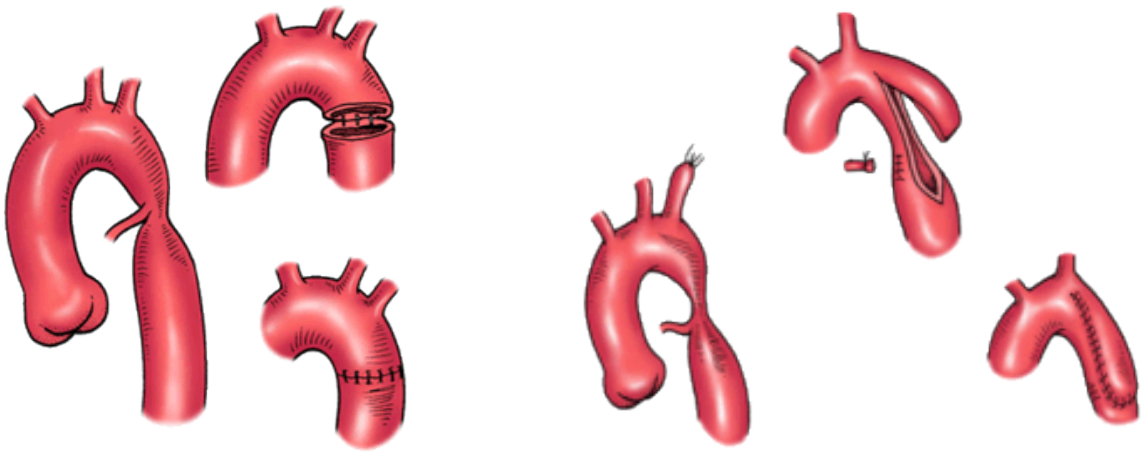

(a) (b)

Figure 2.4.: Invasive surgical repair techniques of CoA involving thoractomy: a) end-to-end anastomosis and b) subclavian flap procedure. (reproduced from [93, 94])

(a) (b) (c) (d)

Figure 2.5.: Transcatheter implantable SHD repair devices: a) AMPLATZER DUCT OCCLUDER II Patent Ductus Arteriosus (PDA) closure device on delivery system - *by St. Jude Medical* [128] b) CoreValve prosthetic heart valve - *by Medtronic* [129] c) Watchman LAA closure device - *by Boston Scientific* [171] d) MitraClip device - *by Abbott* [2]

to completely resect the narrowed wall segment. The subclavian flap angioplasty was introduced by Waldhausen in 1966 to spare the aortic wall and try to help avoid re-coarctation (see Figure 2.4b) [143].

Percutaneous Techniques

The first transcatheter valvuloplasty was performed by Rubio-Alvares, Limon and Soni in 1952 in Mexico [165]. This pioneering work is considered the beginning of

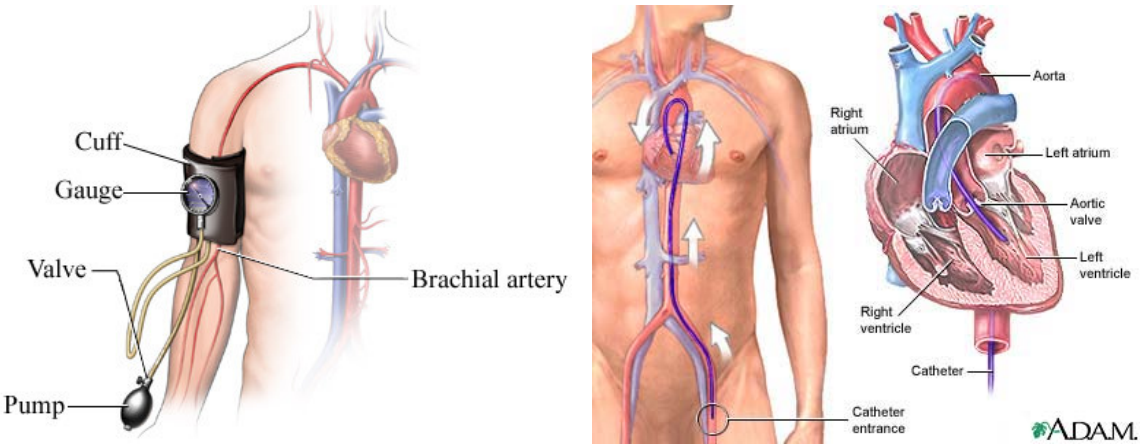

(a) (b)

Figure 2.6.: a) Cuff-based blood pressure is usually measured at extremities, typically at the arm - *by Nucleus Communications, Inc.* [139]; b) Currently invasive blood pressure measurement through cardiac catheterization is the gold standard for CoA severity assessment - *by ADAM Inc.* [78]

SHD therapy. Thanks to the procedural, technological and imaging advances, in the last twenty years cardiac catheterization has evolved from its primary diagnostic function towards therapeutic applications in a multitude of lesions [183]. To reduce invasiveness of surgery, hybrid procedures have been developed whereby skills from both pediatric surgeons and interventional pediatric cardiologists are required [6]. In these procedures direct view of all relevant anatomy is not be possible and require peri-operative imaging for guidance and navigation. The introduction of imaging devices (such as C-arm, echocardiography, CT, MR [158]) in the surgical suite allowed widespread adaptation of hybrid operating rooms.

During percutaneous MIP a small incision is made on the skin typically at the groins to access the femoral arteries/veins, through which a catheter guide wire is threaded to the site of the repair in the heart. In certain cases walls of the heart need to be crossed (septal puncture) to allow for necessary distance and angles for landing sites. Depending on the defect, a corrective device (such as a prosthetic valve, stent, balloon or closure device) is tunneled trough vessels along the catheter to be deployed. The interventionist is often navigating the catheter under X-Ray fluoroscopy (see Section 2.2.3) or echocardiography (see Section 2.2.2) guidance. During MIP the patient is under general anesthesia or sedation. The use of percutaneous transcatheter procedures are becoming available for patients in inoperable conditions too and generally promise easier recovery and quicker hospital discharge [183].

The foremost successes in SHD is probably the breakthrough transcatheter aortic valve implantation (TAVI) technology. In 2002 Alain Cribier performed the first TAVI procedure in a human [24]. TAVI is indicated for severe symptomatic aortic

stenosis in high-risk patients who are excluded from surgery. The procedure enjoys widespread adaptation: in Europe alone, an estimated more than 20 000 TAVI procedures were carried out between 2007 and 2011 [40]. Figure 2.5b shows an example of a contemporary prosthetic aortic valve. TAVI is actively researched, various prosthesis designs are under development and are aiming to improve deliverability and patient outcomes. Besides the most common angiographic guidance, echocardiography is investigated for TAVI [7, 8].

Surgical repair of mitral insufficiency usually require cardiopulmonary-bypass, but not all patients are eligible for such surgery. Endovascular clipping of a regurgitant mitral valve (MV) was first investigated in 2003 [180] using echo guidance. For patients denied surgery the MitraClip (see Figure 2.5d) device was cleared by the FDA in 2013, and recently the feasibility of MitraClip deployment using 3D intracardiac echo [147] was shown. Prolapsing MV may develop due to damaged chordae tendineae. As a less-invasive option to open-heart chordal surgery, a percutaneous, beating-heart repair was introduced with the NeoChord device [172]. This transapical procedure is guided with echocardiography, and performance of the repair and residual leaks are routinely assessed by Doppler echo.

Transcatheter closure devices were shown to be able to treat pathological blood passages of PDO, ASD, VSD and PFO (Sec. 2.1.2) percutaneously. Double-disk umbrella shaped devices such as the one shown in Figure 2.5a conform to various lesions. In AF patients, transcatheter occlusion of the LAA was shown to be a safe and feasible to alleviate the risk of thrombembolic stroke. Figure 2.5c depicts a closure device. Both types of devices allow tissue in-growth after the implantation.

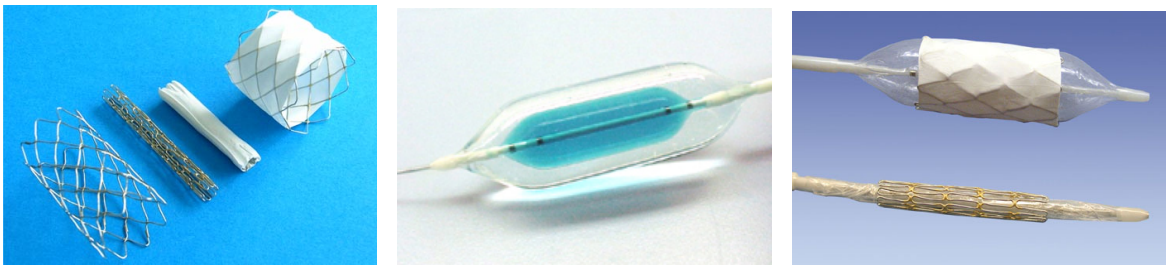

(a) (b) (c)

Figure 2.7.: a) Bare metal and graft covered Cheatham-Platinum (CP) stents for CoA repair; b) Balloon-in-balloon device used to uniformly expand the CP stent; c) CP stent mounted on delivery catheter in closed and inflated state - *by NuMED Inc.* [80, 79, 81]

Pre-operative evaluation of CoA severity relies predominately on non-invasive arm/leg blood pressure (see Figure 2.6a) drops or, if anatomy does not make that comparison feasible, estimation by Doppler ultrasonography. Alternatively CoA is characterized [202] by greater than 50% narrowing of the aorta as compared to the diaphragmatic aorta diameter based on radiographic measurements. Nevertheless, the clinical

gold-standard is obtained by invasive cardiac catheterization to measure $\triangle P$ across the coarctation site (see Figure 2.6b). Systolic blood pressure drop between the ascending aorta (AAo) and descending aorta (DAo) above 20 $mmHg$ characterizes severe CoA and serves as an indicator for treatment [202].

Besides invasive surgical repair – after the neonatal period – CoA treatment options [63, 31, 192, 37] include stent implantation (see Figures 2.7a,2.7c and 2.8) and balloon angioplasty (see Figure 2.7b).

2.2. Cardiovascular Imaging Modalities

Medical images provide insight into internal structures of the body, where direct view or access is not possible without opening the patient. Imaging evolved to help understanding the cardiac system: capturing morphology and dynamics (movement) of the heart together with measuring the blood flow. Clinical images are heavily relied on throughout the lifetime of cardiovascular disease management: from establishing diagnosis and assessment, through treatment planning and therapy guidance to follow-up.

The roots of medical imaging go back to the end of the 19th century, when Wilhelm Roentgen [166] described the first radiograph using ionizing X-Ray radiation. Starting with the early 1950s, the first successful medical ultrasound equipment was developed. A next major wave of innovation came in the 1970s, when commercial cross-section (tomographic) image scanners became available (X-Ray Computed Tomography and

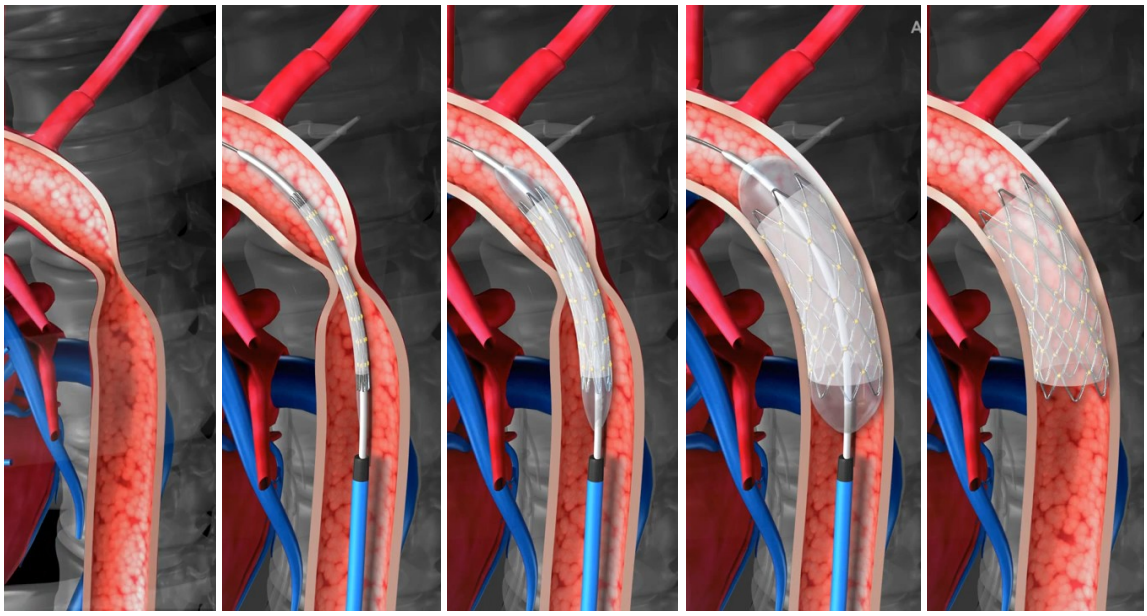

Figure 2.8.: Schematic overview of percutaneous CoA repair via balloon expandable graft covered stent - *by BVM Medical* [127]

Magnetic Resonance Imaging). In the 1980s digitization of the image reconstruction, processing and review pipelines started, while the 1990s brought wider availability of 3D imaging.

Depending on the underlying physical phenomena, individual modalities have advantages and limitations in assessing the cardiovascular system. Images are used not only to understand the anatomic morphology, but additionally certain imaging modalities provide temporal and functional information (such as tissue dynamics, chemical composition, metabolism or blood flow quantification) of cardiac status and performance or enable intra-operative navigation.

In the following sections we will provide a brief introduction to the cardiac imaging modalities that are relevant for the clinical context of coarctation of aorta (see Chapter 3) and image-guided cardiac interventions (see Chapter 4).

2.2.1. Cardiac Magnetic Resonance

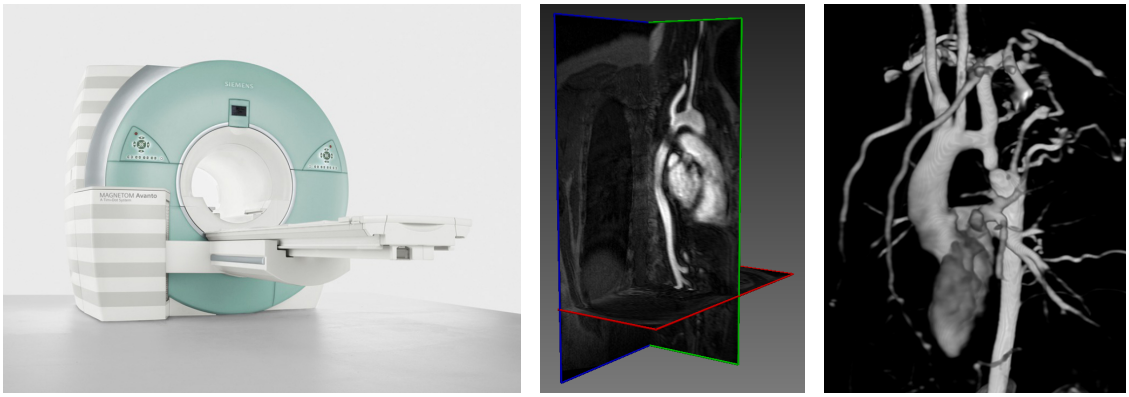

(a) (b) (c)

Figure 2.9.: (a) Modern MRI scanner (Magnetom, Siemens, Erlangen, Germany); (b) Contrast-enhanced MR angiogram (CE-MRA); (c) Volumetric reconstruction of 3D cardiac MRI, showing the aortic arch and surroundings in presence of CoA.

Cardiac magnetic resonance (CMR) is an imaging technique relying on high-strength magnetic fields and radio frequency (RF) waves to excite molecules and sense their resonance in the body. Current MRI equipment (such as seen on Figure 2.9a) is typically wide-bore: using cylindrical superconducting magnets to create uniform magnetic fields of 1.5 or 3 *Tesla* around the patient's body. The RF sequences/protocols used in MRI most often interact with Hydrogen nuclei in the body. This creates images depicting the water concentration in tissue. All material in the body contain water in varying amounts, thus MRI produces excellent tissue contrast.

MR provides flexible region-of-interest imaging: acquisition of arbitrary oblique planes and volume slabs are possible through application of RF excitation facilitating

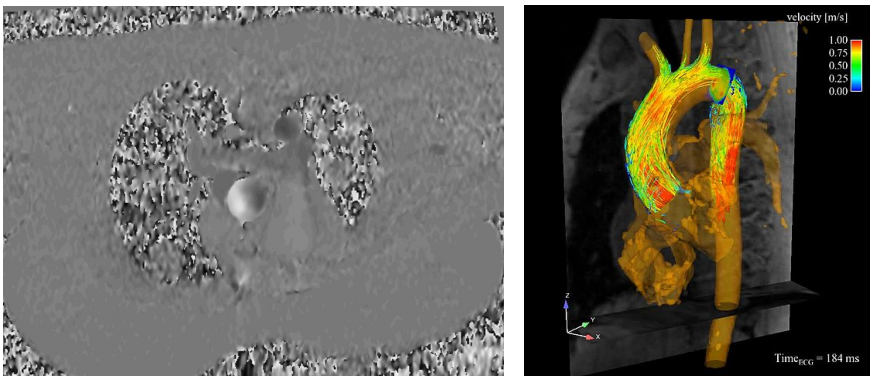

(a) (b)

Figure 2.10.: (a) In a flow encoded 2D phase contrast MR image stationary tissue appears gray, air appears as noise (lungs and outside of body) while bright and dark colors show through-plane flow in opposing directions (ascending and descending aorta); (b) The sparse 3D vector field captured by a "4D Flow" CMR image, is shown here as particle traces.

localized imaging of key cardiac structures. Besides static images, the typical cardiac MR imaging protocol is the cine mode: here the MR image acquisition is synchronized to the electrocardiogram (ECG) signal thus multiple frames within the cardiac cycle are captured. Cine MR is most often used to visualize the motion of heart walls, great vessels or valves over time. Thereby prevailing imaging of the heart is through stacks of short- or long-axis cine slices [150]. The aorta is typically imaged through 3D MR angiography (see Figures 2.9b and 2.9c) with gadolinium contrast agent administered into the blood stream.

MR is capable of functional cardiac imaging. Using "phase contrast" (PC) sequences, flow sensitive images are acquired, where image intensity is representing local spatial velocities instead of anatomic composition. Typical PC-MRI measures through-plane velocities in a 2D slice (see Figure 2.10a). Recently termed "4D Flow"[122, 121] measures velocities in all three spatial directions at each voxel of a sparse 3D volume (see Figure 2.10b). PC-MRI is typically used in cine mode to record the temporal evolution of blood flow during the entire cardiac cycle.

Besides widespread diagnostic applications, research was lately directed towards intra-operative uses of cardiac MRI to aid catheterization [158].

The advantages of MRI include excellent imaging of stationary structures, and high-quality 2D imaging of moving (cardiac) structures. 3D volume imaging of moving anatomy is still an emerging area. As a result of the above properties, MRI is one of the non-invasive reference imaging modalities for congenital heart disease patients. Nonetheless the cost of scanner machines and lengthy scan times limit the practicality of MRI. Further complication is the requirement for magnetically shielded rooms for MR equipment and incompatibility with ferromagnetic tools, devices and implants.

Risk factors pertaining to use MR contrast agents are still unclear, especially for patients with renal problems.

2.2.2. Echocardiography

Echocardiography (or echo) refers to the ultrasonic imaging of the cardiac anatomy. Echo is the routine examination used for assessment of cardiac anatomy, morphology, function and hemodynamics.

The principles of sonographic imaging are the same across cardiac and non-cardiac applications: the ultrasound transducer (probe) emits sound waves into the body tissue and receives their reflections. The resulting image is showing the acoustic structure of the underlying anatomy. Typical 2D and 3D imaging applications use frequencies above the audible range of humans, in between $1 - 15\ MHz$. Doppler echocardiography is able to create velocity encoded images by calculating the frequency shift in moving samples (e.g. blood flow).

Usual ultrasound equipment includes two key components, the transducer and a visualization platform, such as the SC2000 (Siemens Medical Solutions Inc., Mountain View, CA, USA, see Figure 2.11a).

Ultrasound imaging carries many advantages, among which the most important are: good image contrast in soft tissue, non-invasive and real-time image formation. Echo provides flexible pre-, intra- and post-operative imaging as echocardiography may be freely performed where the ultrasound machine is transported: in the catheter lab, in the interventional suite or at the bedside. Ultrasound equipment is usually more cost-effective in comparison to other modalities (e.g. MRI).

At the same time, sonography has a number of drawbacks including shallow penetration (maximum depth of $8 - 15\ cm$ from the transducer), limited field of view, operator and view dependent noisy images (speckle [38]) and restricted view behind bones (shadowing). Image compounding was shown to be a feasible but difficult way to increase the limited field of view [203] of ultrasound. Metallic devices and tools also result in image distortion. However there is great deal of knowledge, experience and techniques to manage the limitations and contribute greatly to the widespread availability of ultrasound.

Cardiologists are most often trained to use echo. Besides diagnostic use, echocardiography was introduced into the operating room to guide procedures [7, 172, 100] and navigate interventional devices. Intra-operative use of echo evolved from simple 2D TTE (Transthoracic Echocardiography) towards volumetric ICE and TEE (Transesophageal Echocardiography). While 2D imaging is limited to a single plane, 3D allows visualization of spatial context.

The main interventional and diagnostic uses of ultrasound in structural heart diseases are discussed in the following paragraphs.

Transthoracic Echocardiography (TTE)

Transthoracic Echocardiography (TTE) is historically the standard cardiac ultrasound imaging. The sonographer holds the transducer in his hand freely, pushes to the patient's thorax and finds an acoustic window between the ribs to image the heart through the chest. Current TTE probes allow acquisition of 2D or 3D images. Among other views, TTE is able to depict the structure of the heart, including all four chambers (see Figure 2.12a) and valves. It provides ways to determine the ejection fraction, quantify regurgitation [59] or perform stress imaging. However the back side of the heart is hard to image due to its distance the probe. Interventional application of TTE is limited due to compromise of the sterile field.

Transesophageal Echocardiography (TEE)

In Transesophageal Echocardiography (TEE), a special ultrasound transducer – only larger than a thumb (see Figure 2.12b) – is inserted into the patient's esophagus. It is fixed to an end of a flexible endoscopic tube. During TEE, the probe is pushed to a position behind the heart in the esophagus where the echo beam reaches the heart almost directly, without traveling and attenuating through thicker tissue. Rear parts of the heart, such as the left atrium are depicted clearly in TEE. This examination is semi-invasive and requires sedation/anesthesia due to swallowing discomfort, thus TEE is primarily used peri-operatively. Diagnostic TEE is indicated if the patient's anatomy or condition doesn't allow for TTE.

TEE is capable of acquiring color Doppler and B-mode (2D planar, bi-planar and volumetric) images. Modern TEE uses a matrix of piezo-electric elements to form echo beams to capture 3D images in real-time.

Intra-operative TEE is routinely used during structural heart disease interventions [7]. TEE images provide good view of the valvular morphology and vegetation (see Figure 2.12b). It was shown [41] that transcatheter aortic valve implantation (TAVI) is possible under TEE guidance and allows to avoid angiography (the use of contrast agent during Fluoroscopy). After TAVI, TEE also allows evaluation of the prosthesis function and detection of paravalvular leakages. Further, TEE may also be used to look for complications such as pericardial effusion or aortic dissection [62]. Lately transapical mitral valve leaflet prolapse repair with the NeoChord [172] device was presented under TEE guidance. Recently published guidelines and recommendations on the 3D echocardiography aim to standardize volumetric views and examination protocols [100].

Volumetric Intracardiac Echocardiography (ICE)

Through the miniaturization of electronics and advanced machining, phased-array echocardiography transducers have emerged [53, 208] that fit into the size of a cardiac catheter: intracardiac echocardiography (ICE). ICE was first introduced clinically in 1993[169] to provide real-time acquisition of images, from the inside of the heart

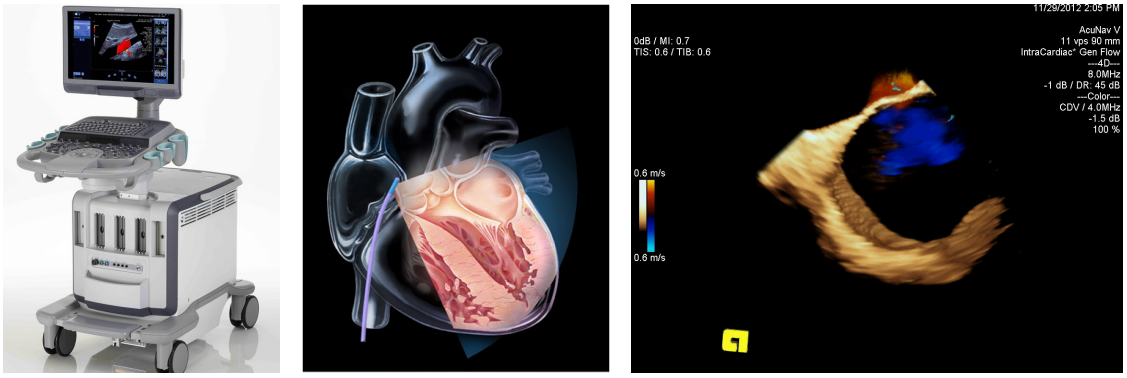

(a) (b) (c)

Figure 2.11.: (a) Siemens SC2000 Echocardiography system; (b) Schematic view of an ICE catheter in the heart, highlighting a possible 2D scan; (c) Flow-encoded 3D Doppler image of PFO syndrome captured by ICE catheter

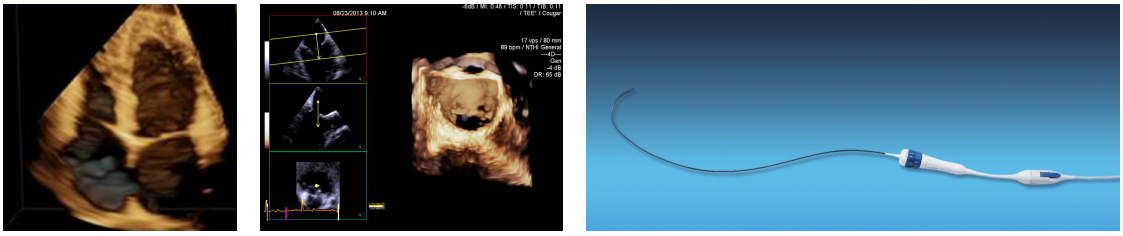

(a) (b) (c)

Figure 2.12.: (a) Transthoracic Echocardiogram (TTE) showing four-chamber view of the heart; (b) Volumetric TEE image of the mitral valve opening, and reformatted 2D slices through the anatomy; (c) Siemens AcuNav V volumetric ICE catheter with steering handle

(Figure 2.11b). ICE is often used in electrophysiology (EP) procedures and it may be navigated anywhere inside blood vessels where the lumen diameter is greater than the thickness of the catheter tip (e.g.: $10F$ or $3.3\,mm$). Modern ICE catheters, such as the AcuNav V (Siemens Medical Solutions, Mountain View, CA, USA) enable acquisition of 3D volumes (see Figure 2.12c) and Doppler measurements (Figure 2.11c) as well.

The approach for ICE catheter insertion is typically trans-femoral venous, alternatively through the jugular or subclavian veins. These methods allow positioning the probe in the right side of the heart through the vena cava.

The ICE catheter may be inserted under local anesthesia. The main benefit of ICE compared to trans-esophageal echo (TEE) is the removal of general anesthesia (GA) from the ultrasound imaging procedure. Furthermore it may be important for high-risk or elderly patients to breath freely on their own during the intervention,

as GA may interfere with cardiac functions and alter intra-cardiac pressures. Thus recent interventional literature suggests great potential to ICE [92, 95, 175] in guiding non-coronary cardiac interventions.

3D imaging provides real spatial context outside the standard 2D imaging plane enabling anatomy and instrument visualization. Furthermore 3D avoids the point-of-intersection ambiguity of a 2D imaging plane, where one e.g. can not tell the difference between a cross section of an instrument or the tip of the given tool. In Doppler acquisition mode ICE and TEE are the standard tools to locate and assess paravalvular leaks. TTE and TEE are most often used to quantify volume of valvular regurgitation. Figure 2.11c shows a three dimensional ICE image of blood flow through septal wall (in a patent foramen ovale (PFO) patient).

Intravascular Ultrasound

Intra-vascular ultrasound (IVUS) is an other catheter based ultrasound imaging modality. IVUS creates two-dimensional cross-sectional images at the tip of the catheter (see Figure 2.13a). These near field images are most frequently used to assess severity of plaque deposits within the coronary arteries to diagnose CAD. IVUS helps differentiate various types of plaques and allows detailed measurements of the magnitude of the plaque area, calcification, lumen morphology and vessel cross-section. To allow passing through small vessels, the typical IVUS diameter is $3.5F$ ($1.166mm$) - $4F$ ($1.333mm$).

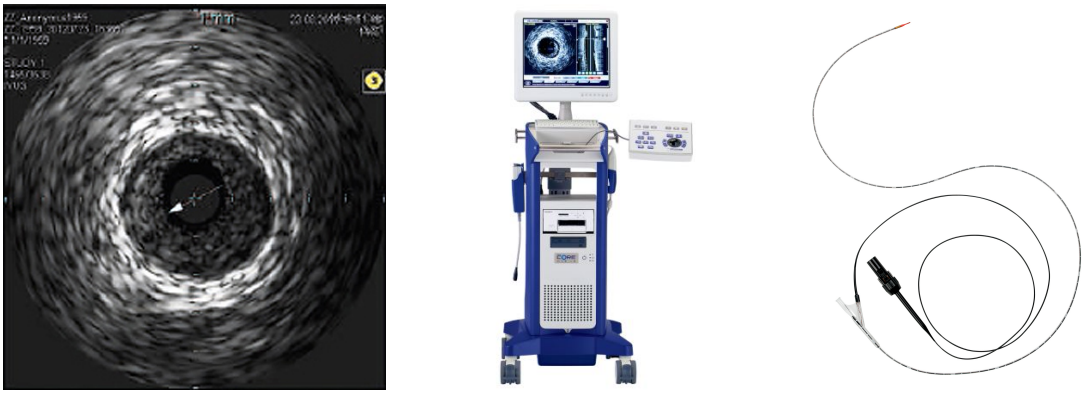

(a) (b) (c)

Figure 2.13.: (**a**) Screen capture from the Siemens IVUSmap clinical software, showing coronary artery wall structure in a cross-sectional view. (**b-c**) IVUS machine and catheter - *by Volcano Corporation* [22, 21]

2.2.3. X-Ray Fluoroscopy and Angiography

X-Ray (XR) Fluoroscopy is a type of imaging that uses ionizing X-Rays beamed through the patient to create a projection image. Image contrast is in proportion with attenuation of X-Rays as they travel through the body. As a consequence soft tissue appears brighter than bones, while metallic structures (such as guidewires, catheters, devices) have a dark appearance (see Figure2.14b). Due to their homogeneous radiopacity, soft tissues are rarely distinguishable in XR.

During a fluoroscopy procedure, XR images are acquired continuously, creating a cinematic "movie" projection of the patient. In angiography, radiopaque contrast agent is administered into the blood stream to highlight vessels, heart chambers or blood cavities in XR in more detail. Nowadays catheter labs are usually equipped

(a) (b) (c)

Figure 2.14.: (a) Siemens Zee robotic C-arm mounted interventional X-Ray system; (b) Typical X-Ray fluoroscopy (XR) image of a cardiac intervention: marginal contrast for soft tissue, low contrast for bones, excellent contrast for metallic tools, devices and implants; (c) Volumetric reconstruction of cardiac C-arm CT image.

with C-arc robotic arm mounted XR machines, consisting of a vacuum tube and a flat-panel digital XR detector. These instruments allow XR images to be taken through the patient in arbitrary directions. Widely available robotic C-arm systems – such as the Zee (Siemens AG, Forchheim, Germany) ceiling mounted system shown in Figure 2.14a – enable rotational angiography (C-arm CT, see Figure 2.14c) as well. During a C-arm CT scan, the arm is rotated and spinned around the patient. During the sweep a few hundred 2D images are acquired. This projection sequence is then used to reconstruct a 3D volume. Such systems usually allow the C-arm gantry to be retracted from the operating table to allow freeing up space around the patient when no imaging is performed.

The advantage of XR is real-time display and high resolution of the acquired images. On the downside patients receive a dose of ionizing radiation. However the risk carried by the therapy itself (e.g. catheterization, anesthesia, contrast agent) is usually greater than the radiation risk. Hence XR is the routine navigation tool for catheter insertion and manipulation, as well as stenting during minimally invasive

interventions. Due to the projective nature of the modality, XR provides limited visualization of 3D structures.

Fluoroscopy remains the dominant imaging modality interventional cardiologists and radiologists are trained to use: for patient selection, for intra-procedural navigation, and to assess procedural outcomes. Figure 2.15 shows a typical application of X-Ray Fluoroscopy in the catheterization lab: minimally invasive CoA stenting procedure. Here all steps are performed under XR guidance: threading the guide-wire into the aortic arch, placement of the closed stent and stent expansion for deployment. For percutaneous coronary interventions (PCI) fluoroscopy is the standard imaging

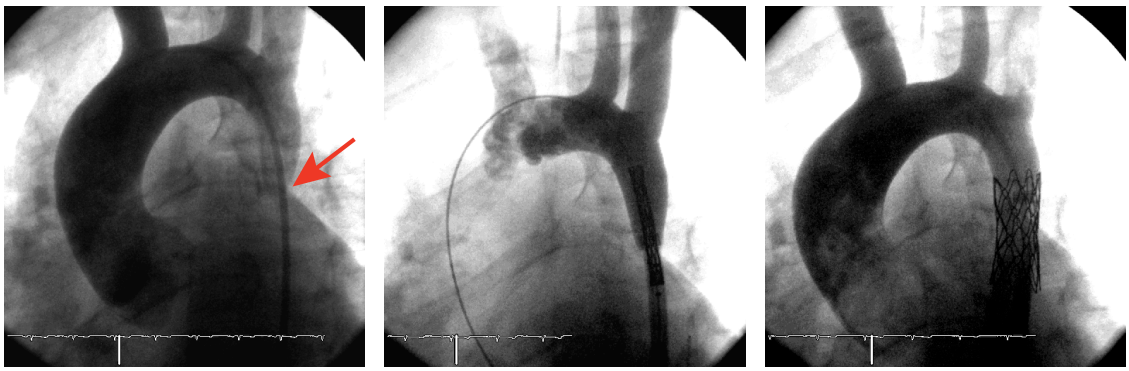

(a) (b) (c)

Figure 2.15.: Three steps of an endovascular stenting procedure observed through X-Ray angiography: a) guide-wire within the aorta, with arrow indicating location of coarctation lesion, and injected contrast agent showing the lumen outline; b) stent mounted on a balloon is positioned along the guide-wire to the CoA; c) the expanded stent restores unobstructed flow.

modality, but percutaneous SHD requires additionally soft tissue imaging.

2.2.4. Other modalities

In the previous sections, we have introduced the anatomical imaging modalities that are forming the foundations of the methods described in Chapters 3 and 4, however besides the above listed ones, there exist many more different imaging systems. For the completeness we briefly mention other major cardiac imaging modalities even though these modalities are not directly used in this work.

The working principles of Computed Tomography (CT) are very similar to XR (Sec. 2.2.3), in this case the rotating gantry with multiple detectors reside in a closed housing. Cardiac CT scans are typically 3D volumes or ECG gated 4D time-series of the cardiac cycle. In the cardiovascular space CT is predominantly used for pre-operative planning and modeling [212, 82].

3D radionuclide imaging techniques such as single-photon emission computed tomography (SPECT) or positron emission tomography (PET) are often used for myocardial muscle perfusion imaging to assess coronary artery disease (CAD) and to stratify risk of future cardiac events.

2.3. Overview of Medical Image Analysis

According to Frangi et al., over the last 40 years the field of medical image analysis "became a distinct discipline of its own" [48]. Medical image analysis is concerned with the acquisition, reconstruction, enhancement, visualization and semantic interpretation of medical images. The goal of these investigations is to derive clinical evidence from imaging data and to discover knowledge, for example to define image-based bio-markers, to perform measurements, enhance diagnosis, improve therapy or predict outcomes.

During the last decades substantial development in image acquisition and reconstructions has resulted in increased resolution of images and faster acquisition rates. Concomitantly images are increasingly being used outside of traditional diagnostic radiology, for telemedicine and digital pathology [97] and – more relevant to CVD – interventionally for peri-operative guidance and navigation [176]. Due to these tendencies less time is available for manual interpretation of images and automated analysis methods are sought after, especially interventionally to avoid extending procedure times [205].

Medical image analysis methods are built upon the achievements of computer vision, pattern recognition, machine learning and numerical methods. As these fields yielded more and more sophisticated tools, medical image analysis was transformed from processing of images to semantic analysis. This allowed the focus to be shifting towards systemic image interpretation through higher-level, data-driven, personalized models. Methods independent of the underlying imaging modality are of exceptional interest.

During the last decade so called "grand challenges" were established where representative data-sets are available to researchers. The goal is standardized evaluation and the challenges facilitate direct quantitative comparison of image analysis methods for a given task [46].

Our investigation is mainly concerned with semantic interpretation of cardiac images: segmentation and registration, using powerful machine learning algorithms. The next sections are dedicated to introducing a compact review of these research areas, their formalism and literature.

2.3.1. Image Segmentation and Object Detection

In computer vision, classically, image segmentation is concerned with partitioning an image into disjoint groups/sets of pixels where each set is labeled differently from

a discrete number of labels. By semantically partitioning the image into segments the goal is to identify meaningful structures against image background. The case of two labels defines a binary or foreground-background segmentation problem. In medical imaging these structures or regions of interest most often represent organs, lesions, pathologies, vessels, fiducials or devices. Due to the high variety of imaging modalities, varied image content and non-uniformity of image quality, there is no single method for medical image segmentation that performs in a satisfactory way on every image or modality. Medical and cardiac image segmentation is still an active field of investigation [47, 103, 150].

Segmentation methods may be classified from multiple perspectives. The mode of operation may either be automatic or require manual interaction. Frequently, in the clinical setting automatic segmentation methods are preferred. Automatic segmentation is key to reproducibility to avoid the bias of intra-user variability and allow autonomous operation during intra-operative navigation and guidance.

An other classification of segmentation methods is possible based on the employed mathematical formalism. Early works such as thresholding, morphological operations, watershed transform and clustering operate on image intensities directly without considering information from the problem domain or object of interest.

Graphical models have been successfully applied to segmentation, predominantly in the Markov Random Field formulation of graphs built from images. On such structured graphs well understood graph optimization is possible, for example using an efficient max-flow energy minimization algorithm [14] for binary segmentation or through random walks [58] for multi-class problems. These semi-automatic methods require some pre-specified seeds (labeled pixels) for initialization and subsequently assign a label to each unseeded pixel.

Deformable models evolve an initial surface or curve, ideally to the boundary of the object of interest [126]. The front moves under the influence of internal curvature constraints in addition to external, image-based forces. Deformable models may have explicit formulation including active contours [88], or implicit such as level sets of a higher dimensional scalar function [145]. Since 1995, when Cootes et al. [20] introduced it, active shape models (ASM) became popular for medical image segmentation. Statistical shape analysis and related techniques capture prior knowledge of shapes with statistical models of populations. Statistical shape models where successfully used to segment organs where topological changes need not be considered: such as the liver [66], the prostate [107], all chambers [212] and valves [83] of the heart and knee bones [209, 13]. During the training phase of the model, domain specific shape variations are learned. Whereas at evaluation time on unseen images the model is used for shape regularization to favor probable shapes. Active Appearance Models (AAM) encode – in addition to shape statistics – the variation of gray-scale appearance (texture) of the images too.

Segmentation algorithms that require manual initialization are efficiently combined with automatic object detection to provide initialization of the region of interest as global location and pose. In the 2000s the Viola-Jones object detection frame-

work [198] sparked a very successful line of object detection algorithms. The core of the method lies in an exhaustive, dense sliding window search, efficiently computed 2D Haar-like features and boosting-based learning algorithms. These methods have been successfully applied to face-detection [198] in computer vision and parsing of medical images of the heart [212, 82]. In order to avoid the sliding window search with a cascade of binary classifiers evaluated at each step, an elegant approach was proposed by Zhou et al. [219]. The authors build on the strong spatial context – relationship of organs – in medical images, and learn a boosted ridge regressor. For each image patch the regressor votes for the relative offset of an object of interest. Pauly et al. furthered the concept to simultaneous regression of multiple objects in 2011 using random forests [148].

Recently, neural networks have also shown promising results in challenging 3D object localization in volumetric medical data [217].

For cardiac images, tracking is an other important concept. Tracking considers image sequences over time (for example over the cardiac cycle) to identify objects and infer their motion. Tracking of the left ventricle [211] and heart valves [83, 220] was recently presented in 4D echocardiography.

2.3.2. Computational Image Analysis

Routinely in the treatment of cardiovascular diseases the primary clinical intention is to restore blood circulation to tissues. Often multiple therapy options are feasible and before performing an invasive repair physicians would like to predict possible outcomes. This creates demand for understanding geometry/anatomy information in conjunction the function and pathological processes as well.

Acknowledging this need, the development of multi-scale biophysical models was prioritized by various research councils. The European Union funded the Virtual Physiological Human program and the Physiome Project is commissioned by the International Union of Physiological Sciences. Common in these international efforts is the desire to pursue development of holistic, personalized computational models to enable predictive medicine.

Personalized computational models and numeric analysis emerged in a wide variety of problems in the context of structural heart disease (SHD) and cardiac diseases. Voigt et al. have demonstrated that a coupled image-based and biomechanical model of the mitral valve leaflets results in lower tracking errors [200]. Further, it was shown that a biomechanical model of the mitral leaflets might allow therapy planning and patient selection for the MitraClip procedure [118]. Mihalef et al. introduced a patient-specific organ level model of the human heart that integrates 4D CT based morphology, dynamics and computed haemodynamics [130]. It is key in cardiac resynchronization therapy (CRT) to understand the electrical properties of the patient's heart for efficient planning of the leads. In [173] a computational model was established for regional parameter estimation. Mansi et al. presented an image-based model of heart growth and remodeling to correlate with pathology in tetralogy

of Fallot patients [117]. Recently a method was disclosed to estimate the mechanical properties of the aortic wall (compliance, resistance) based on coupled fluid-structure interaction model [18] that may be fitted to "4D Flow" CMR (Sec. 2.2).

The effort to extract knowledge from cardiac images using computational methods is bearing fruit, one of the most prominent example of success is in coronary artery disease (CAD). The non-invasive estimation of fractional flow reserve (FFR) from cardiac CT angiographies [174, 191] allows severity assessment of coronary artery stenoses and likelihood of ischemia. The personalized coronary circulation is simulated with computational fluid dynamics (CFD) models of the blood flow in the patient specific coronary geometry segmented from 3D cardiac CT.

2.3.3. Interventional Image Registration and Fusion

During image registration the goal is to establish the spatial correspondence between the pixels of two or more images (for our investigation we focus on registration of two images, the target and reference). In other words, a correct alignment of the images is to be determined. The purpose of traditional registration is many-fold, e.g. to extend the field of view of images (mosaicing), to bring additional or complementary information into the same coordinate system, to compensate for organ motion or to facilitate atlas-based segmentation approaches.

The registration task relates the spaces of the target and reference images depending on the type of the geometrical transformation. The most important transforms may be categorized as rigid, affine, perspective projection, deformable models.

Another classification is possible depending on the basis of the registration: image intensity-based or feature-based (point-based and surface- or model-based).

In the operating room (OR), notably during SHD repair, we encounter two highly desired goals of interventional fusion. Solutions to the these problems are one of the key enablers of minimally invasive (trans-catheter) cardiac interventions and we will briefly review the literature of this active area of investigation.

First intent is to make diagnostic information (segmentation, anatomic models, measurements and plans) derived from high-quality pre-operative images available during a procedure where X-Ray fluoroscopy or C-arm CT (Sec. 2.2.3) lacks such detail. Based on the dimensionality of the involved images the registration problem may be classified as 3D-2D and 3D-3D. Recently Markelj et al. [120] provided an extensive survey and review of 3D-2D registration methods where 3D pre-operative MR/CT images are aligned to intra-operative X-Ray/fluoroscopy images through estimation of perspective projection. Grbić et al. demonstrated cardiac multimodal 3D-3D registration of pre-operative segmented CT images and intra-operative 3D C-arm CT using the trachea [60] and pericardium [136] models as anchor anatomy.

The second major objective is to enable image-based procedure guidance and tool navigation. Various trans-catheter structural heart diseases (SHD) interventions are enabled by information fusion in hybrid operating rooms with live C-arm and echo available. The complementary image information between multiple peri-operative

imaging modalities allows accurate co-visualization of tools and soft tissue in the same coordinate frame. In the context of TAVI, multiple groups have investigated registration of TEE and X-ray fluoroscopy. These techniques are based on the visibility of the TEE probe in X-ray projections. Peters and colleagues [99] introduced a fiducial-based pose estimation system. Intensity-based registration methods were demonstrated for probe tracking (Gao et al. [52]) and TEE mosaicing (Houdsen et al. [76]). Mountney et al. [133] evaluated machine learning based image fusion, while Heimann et al. had shown transfer learning as a way to augment limited labeled training data [67]. The feasibility of image-based registration of fiducial equipped ICE (Sec. 2.2.2) catheter and X-ray fluoroscopy was shown in 2014 [155].

In Chapter 4 further details of interventional image registration and fusion are surveyed and discussed.

2.3.4. Machine Learning in Medical Image Analysis

Originally developed in the field of artificial intelligence, machine learning has enjoyed a prosperous period in medical image analysis in the last two decades. Supervised learning methods have been proven to deliver expert-level performance in multiple medical image analysis problems [205], including object localization [178], segmentation [212] and registration [60, 136, 67].

In supervised learning the focus lies on discovering knowledge from labeled data to allow later applying the learned information to analyze unseen data. Learning-based methods have shown strong impact in areas where analytic solutions are not obtainable and defining rules that lead to the right decisions is not obvious but it is possible to learn from examples. The probabilistic Bayesian inference framework enables efficient maximum a posteriori (MAP) modeling in the high dimensional space of images.

Development of fast-to-compute 2D and 3D Haar-like and LBP image features [198, 193, 148] together with novel boosting and randomized decision forest algorithms [193, 148] have been shown to be able to effectively recognize patterns in the underlying data and estimate model parameters through image-based classification and regression. Decision trees are particularly efficient to run inference on. As a prerequisite to statistical learning, the training of efficient discriminative models require large, expert annotated database of examples.

It is generally expected that current machine learning methods would reach higher precision given larger labeled training data sets [205]. However this presents a challenge as high quality annotated databases are very time consuming and costly to build, and open databases are not yet available for most medical imaging problems. Crowd sourcing of image annotations and algorithmic techniques such as transfer learning [67] were recently shown as a possibility to address this limitation in certain domains.

2.4. Conclusions

The heart is the central pump of blood flow, driving the circulation in the entire body. It is a complex organ consisting of cavities with contracting walls, blood flow regulating valves and the largest vessel connections. The blood is locked and pumped periodically at high pressure in this closed system. Failure of the many components is inevitable, underlined by the fact that CVD is number one cause of human deaths worldwide.

No medications exist that are able to cure congenital heart defects and the progression of structural heart disease: drugs only help stabilizing conditions. Whereby cardiac surgery remains the operation carrying the highest likelihood of complications and operative risk. To extend the patient population for whom effective treatment options exist less invasive therapies are sought after.

Management of certain cardiovascular diseases require invasive intervention not only during therapy but for routine diagnostics too – such as the invasive blood pressure catheterization in severity assessment of CoA. Additionally, procedure planning relies on manual measurements and simplified approximate methods leading to suboptimal and non-reproducible results. Medical image analysis is expanding towards image interpretation through data-driven, personalized models to provide clinical information with predictive power. Image-based computational modeling of anatomy and function facilitate personalized *in-silico* evaluation of diagnostic and therapeutic procedures and treatment outcome prediction. Applied machine learning proved to be a very efficient tool in fitting these models to patient's data.

In parallel – during the last two decades – various percutaneous procedures and in particular transcatheter implantable devices and techniques have been introduced in cardiac medicine. These developments and widespread adaptation are enabled by procedural, technological and imaging advances. Improved imaging, the availability of peri-operative imaging modalities in hybrid operating rooms and better exploitation of complementary imaging information from intra-operative modalities through novel live fusion and image registration methods are being investigated to help to improve outcomes.

On one hand we expect future challenges to include further development of integrated anatomical, functional and computation models to derive clinical information to enable preventive, predictive, personalized medicine; on the other hand, we foresee the search for better patient outcomes through introduction of more effective and less-invasive procedures.

CHAPTER 3

Non-invasive Blood Pressure Drop Estimation

The effect of coarctation of the aorta (CoA, see Sec. 2.1.2) is a stenosis distal to the aortic arch, resulting in pathophysiological processes that restrict the circulation of oxigenated blood through the coarctation. This necessitates increased cardiac output, and may lead to left ventricular (LV) hypertrophy. Generally CoA results in persistent upper body hypertension and lower body hypotension. Patients born with CoA require lifelong medical/surgical care [189], that includes invasive and non-invasive imaging, drug therapy and if the CoA recurs, invasive catheterization or surgical intervention to reduce the blood pressure in the ascending aorta. Treatment options include various surgical repairs and after the neonatal period, stent implantation and balloon angioplasty [11, 63, 31, 192, 37, 69].

Pre-operative evaluation of CoA severity relies predominately on non-invasive arm-leg blood pressure gradients or, if anatomy does not make that comparison feasible, estimation by Doppler ultrasonography. Alternatively CoA is characterized [202] by greater than 50% narrowing of the aorta as compared to the diaphragmatic aorta diameter. Nevertheless the clinical gold-standard is obtained by invasive cardiac catheterization to measure $\triangle P$ across the coarctation site. However each catheterization carries the risk of thrombus formation, embolization and infection. Systolic blood pressure drop between the ascending aorta (AAo) and descending aorta (DAo) above 20 $mmHg$ characterizes severe CoA and serves as an indicator for treatment [202].

Recently, Doppler ultrasound [101] and phase contrast (PC) MRI based methods [149, 108, 122] have been proposed for a non-invasive estimation of $\triangle P$ by using simplified relationships (e.g. modified Bernoulli equation) between flow and pressure. However these methods were shown to be inaccurate [75].

Thus, there is a growing need for comprehensive and truthful morphological and hemodynamics analysis of CoA for diagnosis, intervention planning, outcome prediction and assessment of lesion progression. Our work in this chapter is directed at

these goals. Additionally, as the CoA population includes young patients, less invasive and less expensive (reducing fluoroscopy and catheterization) methods are sought after for $\triangle P$ estimation. For these reason our attention is turned to computational fluid dynamics (CFD) methods for more faithful characterization of blood flow in the aorta.

This chapter introduces morphological and hemodynamics models of the thoracic aorta and trunks of main branches. A novel technology is described to personalize the model parameters and fit the models to patient data. The model is used to estimate patient-specific blood pressure drop in CoA. The chapter is organized as follows.

Section 3.1 describes the morphology model of the thoracic aorta and main branches, the parts-based decomposition and compact statistical shape representation of patient population. An accurate geometrical representation of the lumen boundaries of the aorta and supra-aortic arteries is essential for subsequent hemodynamic computations. The goal of lumen estimation is to automate the vessel morphology measurement process, and should require manual intervention in a mostly supervisional manner. The aim of Section 3.2 is to present the machine learning-based, robust, patient-specific parameter estimation method that fits the morphological model to patient's imaging data.

In Section 3.3 a computational model of the thoracic aortic circulation is described. Personalization of the hemodynamic computational model is discussed in Section 3.4 based on patient-specific geometry, computational fluid dynamics (CFD) and fluid-structure interaction. Further, Section 3.4 discusses the extraction of the aortic lumen cross sections from 2D+t PC-MR, and the aortic in- and out-flow waveform computations. Lastly, the image-based personalization is introduced (Sec. 3.4.1) for three CoA use-cases: pre-operative (Sec. 3.4.2), post-stenting (Sec. 3.4.3) and "virtual stenting" (Sec. 3.4.4).

In the interest of easing translation of personalized CoA models into wider clinical practice we set out to meet certain expectations. In Section 3.5, 3D lumen geometry segmentation is demonstrated in 212 volumes (Sec. 3.5). Moreover, blood pressure drop is estimated in CoA: we examined six patients' retrospective data, acquired in multiple cardiac centers from USA and EU in various stages of CoA management: pre-operative assessment, treatment outcome prediction and post-operative follow-up.

Our results are discussed in Section 3.6. While, initial work on extensions of hemodynamic assessment is presented in Section 3.7.

3.1. Morphological model of the thoracic aorta

Non-invasively acquired images are a cornerstone of current management of CHD and SHD, however high resolution 3D images are not trivial to interpret directly. Modern medicine demands techniques to process large amounts of data into clinically relevant information in a precise, reproducible and fast manner. For cardiovascular defects such as CoA, the extraction of anatomical and functional bio-markers through

morphological and physiological models is indispensable for quantification, severity assessment and intervention planning.

3.1.1. Background

Ongoing imaging research has been directed at segmenting the thoracic aorta from 3D images. We provide a brief overview of existing aortic models reported in the literature. Work presented by Zhao et al. [214] applies level-sets and manual seed initialization to extract the aorta lumen from MR volumes. Recently, another marching-based method was introduced for aorta segmentation in MRI [45]. Machine learning based automatic aorta detection [216] was successfully combined with shape models and applied in intra-operative guidance, based on rotational C-arm CT volumes.

All three of these segmentation approaches consider the aorta only, excluding the supra-aortic arteries. For our investigation, the supra-aortic arteries are of great importance as the blood flow that leaves the aortic arch through these vessels (approximately 35%) should be considered in the subsequent hemodynamic computations.

On high resolution 3D CT angiograms the feasibility of accurate carotid artery segmentation was extensively demonstrated [61]. Segmentation of the aorta, including the supra-aortic arteries from MR volumes, was initially presented in our previous works [199, 153].

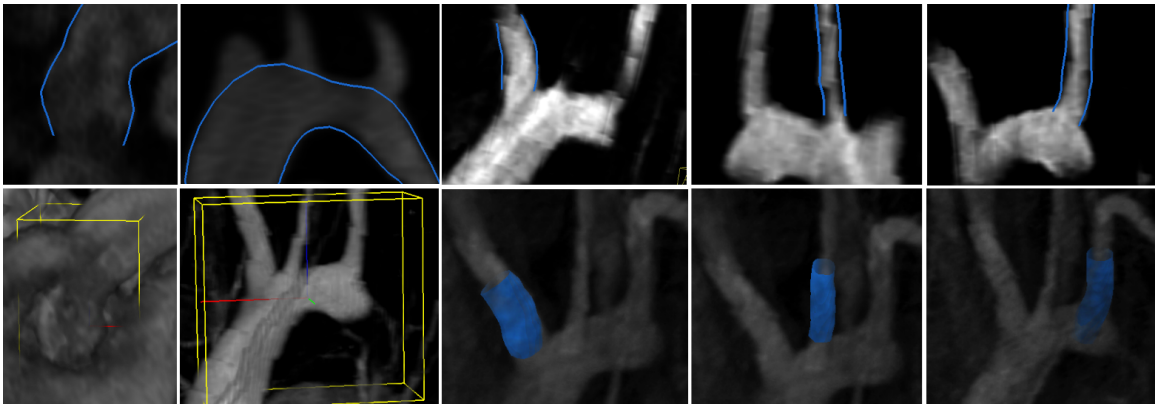

(a)

Figure 3.1.: Thoracic aorta parts in MR images: aortic root, aortic arch, trunk of brachiocephalic artery, trunk of left common carotid artery, trunk of left subclavian artery

3.1.2. Parts-based Model of Vessel Tree

In this section we introduce an organ-level morphological model of the aorta and the trunk of its main branches. The model is a mathematical description of patient-specific lumen geometry. For CoA investigation the definition of the spatial and

computational domain is the lumen of the thoracic arterial tree. The aorta (including the ascending and descending parts and the transverse arch) together with the trunk of its main branches (the supra-aortic arteries) are modeled to delineate the vascular morphology and geometry. The fitted model is used to perform clinical measurements, for assessment, diagnosis and therapy planning and to personalize the hemodynamic computational model in Sections 3.3 and 3.4.

The hierarchical, parts-based decomposition of the aorta model is shown in Figure 3.1. The model involves the following levels of abstraction in the hierarchy: i) global location and pose of parts and ii) lumen surface morphology. The surface model is dependent on and spatially linked to the global location and pose of the parts.

Parameterization

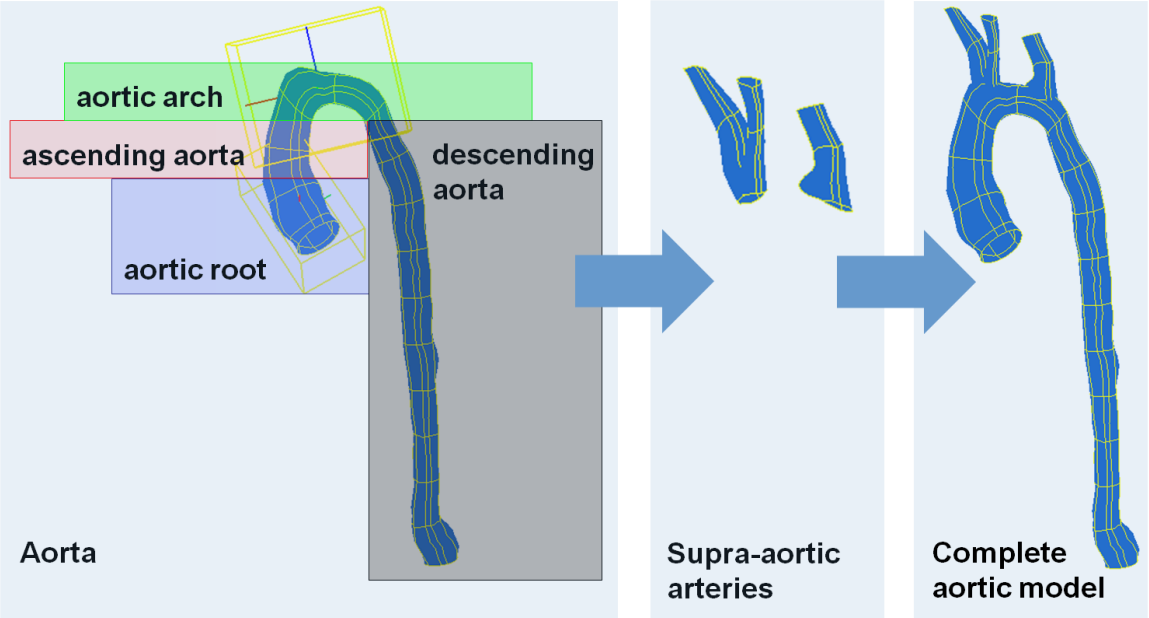

Figure 3.2.: Parts-based model of the thoracic aorta.

On the one side, the cardiac image scans vary in field of view and obliqueness, on the other side CVD patients present heterogeneous morphological morbidities of the heart and aorta. This necessitates parameterizing the global location and pose of the aorta parts to define a subsequent frame of reference in the volumetric images. The global location θ_p of the parts p are parameterized as a similarity transform in 3D space (Eq. 3.1),

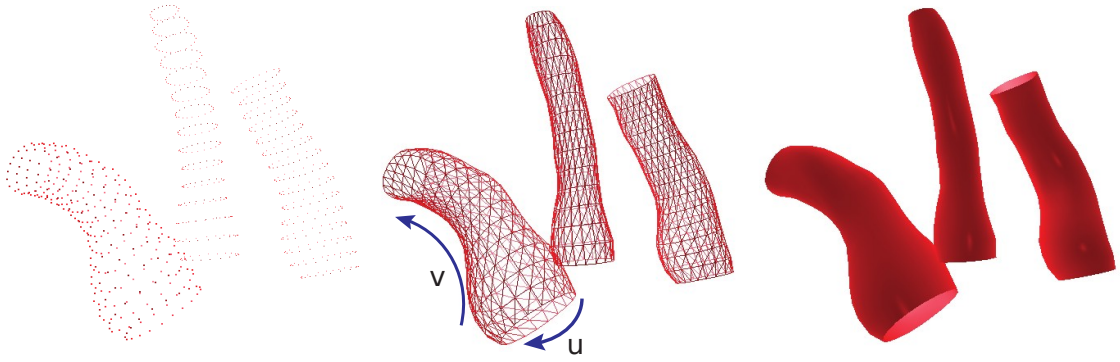

Figure 3.3.: UV parameterization of open cylinder illustrated through the trunk of the three supra aortic arteries. U defined around the circumference, V increases along the vessel in the direction of antegrade blood flow.

$$\theta_p = \left[\underbrace{\{t_x, t_y, t_z\}}_{\mathbf{t}_p}, \underbrace{\{\alpha, \beta, \gamma\}}_{\mathbf{r}_p}, \underbrace{\{s_x, s_y, s_z\}}_{\mathbf{s}_p}\right] \qquad \mathbf{t}_p, \mathbf{r}_p, \mathbf{s}_p \in \mathbb{R}^3,\ p \in \{Ro, Ar, Br, Lc, Ls\} \tag{3.1}$$

defined over nine pose parameters (three for position: $\mathbf{t}_p$, three for orientation: $\mathbf{r}_p$ and three for anisotropic scaling: $\mathbf{s}_p$). The $\mathbf{r}_p$ rotational parameters are expressed as Euler angles, describing rotation around the Cartesian coordinate axes in the fixed Z-axis, Y-axis and X-axis order. Our model of global location and pose includes the following anatomic parts: aortic root (Ro), aortic arch(Ar), and the trunk of supra-aortic arteries — brachiocephalic artery trunk (Br), left common carotid artery trunk (Lc), left subclavian artery trunk (Ls) — and lastly for post-operative cases the stent region (St).

$$\boldsymbol{\theta} \equiv [\theta_{Ro}, \theta_{Ar}, \theta_{Br}, \theta_{Lc}, \theta_{Ls}] \tag{3.2}$$

Thus the model $\boldsymbol{\theta}$ requires $5 \times 9 = 45$ parameters to describe the global location and pose of the five parts in a volume I.

The modeled vessel parts p are abstracted at two levels, first as their pose (similarity transform) and second, their lumen surface as a triangular surface meshes (Figure 3.2). All parts are associated with a surface describing the lumen boundaries in that vessel area[1], these surfaces are embedded in a bounding box defined by the above similarity transform. The deformable surfaces have a fixed point correspondence across subjects.

$$M_s(\boldsymbol{\theta}) = \{\mathbf{v}_1, \mathbf{v}_2, \cdots, \mathbf{v}_n\} \qquad \mathbf{v}_i \in \mathbb{R}^3,\ s \in \{Ro, Ar, Br, Lc, Ls, AAo, DAo\} \tag{3.3}$$

Surface meshes are defined with a fixed mesh topology (open cylinder – see Figure 3.3). The cylinders are parameterized as follows: V is defined along the vessel center-line increasing in the direction of antegrade flow, while U is defined along the

[1]However the walls of ascending (AAo) and descending aorta (DAo) do not have a global pose due to their variable lengths.

circumference of the vessel. The trunk of all three supra aortic arteries is represented by $U \times V = 16 \times 15 = 240$ vertices and 448 triangular faces. The aortic root is modeled by 32×17 vertices and 1024 triangles, while the aortic arch model contains 32×34 vertices 2112 triangles. The model does not implicitly define the V length of the ascending and descending aorta, but those parts contain $U = 32$ circumferential vertices as well.

$$\mathbf{M}(\boldsymbol{\theta}) \equiv [M_{Ro}, M_{Ar}, M_{Br}, M_{Lc}, M_{Ls}, M_{AAo}, M_{DAo}] \tag{3.4}$$

Anatomical definition of *Ro* is from the level of the aortic valve hinge points to the level of the left and right coronary ostia. The aortic root has a distinct scalloped shape, see Figure 3.1. The aortic arch *Ao* is defined by the transverse section of the aorta until the aortic isthmus.

Notable property of the model is that its parameters are independent of the imaging modality.

3.2. Patient-specific Parameter Estimation

In the previous Section 3.1 we presented a parts-based model of the lumen of the thoracic aorta and trunk of main branches, defining the target parameters and model of their spatial distribution. In this section we are aiming to introduce a coarse-to-fine approach to estimate patient-specific values for those parameters from non-invasive 3D images.

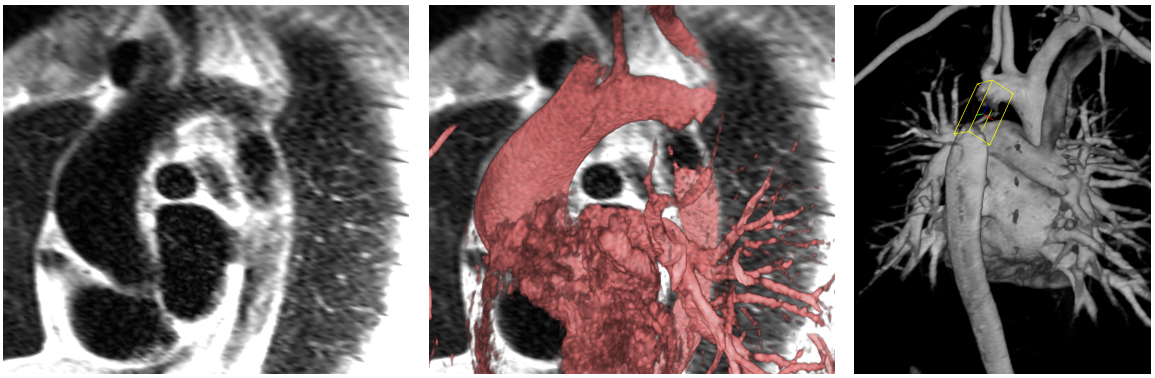

(a) (b) (c)

Figure 3.4.: Effects of implanted metallic stent on MR image quality. **Left**: 2D spin-echo MR image, note that the whole descending aortic lumen is continuously visible. **Middle**: In a 3D cardiac MR volume (typical to our investigation) of the same region (red volume), the metallic stent produces a signal "drop-out" artifact rendering the lumen visually missing. **Right**: Bounding box of a stent region θ_{St}.

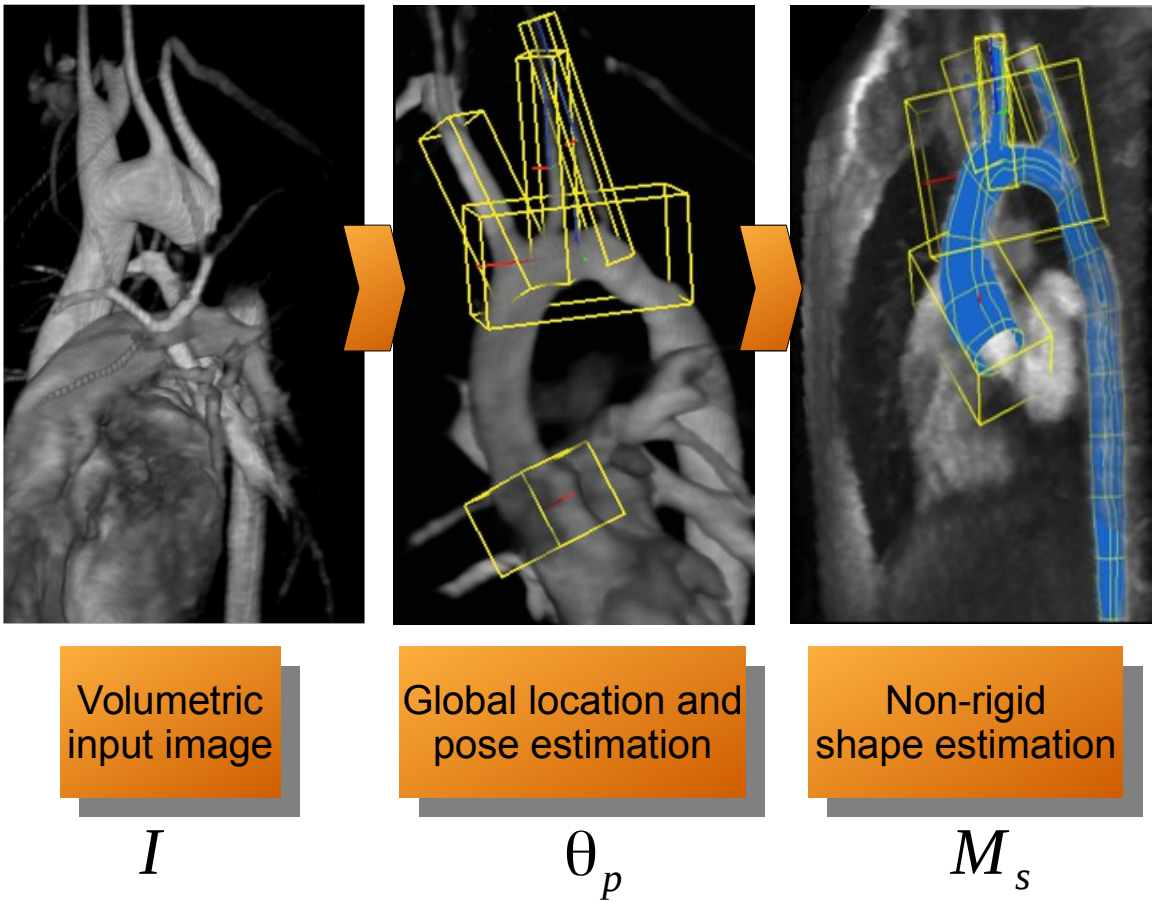

Figure 3.5.: Overview of estimation procedure for the parts-based thoracic aorta model. Given a cardiac volume, first a global search is performed to localize the parts and respective poses. Subsequently, deformable lumen boundaries are fitted in local context.

The estimation of the aorta model parameters $\boldsymbol{\theta}$ and $\mathbf{M}$ from an image I is a challenging task due to the large number of model parameters, the pathological variations presented by CVD patients, limited MR image quality and unconstrained field of view of the scans. Nevertheless, robust solutions are sought after that are able to fit the model to noisy clinical data. To make this problem more tractable it is inevitable to incorporate prior knowledge about the morphology. Supervised machine learning offers an effective technique to incorporate prior knowledge through expert annotated examples. In our case we had approximately 200 MR volumes available to perform statistical learning. We have seen in Section 2.3.4 that machine learning provides a powerful probabilistic framework in comparison to alternative image analysis methods.

The probabilistic Bayes' theorem provides a concise framework to describe param-

eters of a statistical model given data:

$$p\left(Parameters|Data\right) = \frac{p\left(Data|Parameters\right) \cdot p\left(Parameters\right)}{p\left(Data\right)} \tag{3.5}$$

Concretely, we may formulate our parameter estimation problem through Eq. 3.5:

$$p\left(\boldsymbol{\theta}, \mathbf{M}|I\right) = \frac{p\left(I|\boldsymbol{\theta}, \mathbf{M}\right) \cdot p\left(\boldsymbol{\theta}, \mathbf{M}\right)}{p\left(I\right)} \tag{3.6}$$

here $p\left(\boldsymbol{\theta}, \mathbf{M}|I\right)$ is the posterior probability, $p\left(I|\boldsymbol{\theta}, \mathbf{M}\right)$ is the likelihood and $p\left(\boldsymbol{\theta}, \mathbf{M}\right)$ the prior term (we assume the normalization factor $p\left(I\right)$ to be one).

A generative learning strategy would allow to approximate the likelihood probability $p\left(I|\boldsymbol{\theta}, \mathbf{M}\right)$ with parametric schemes. However, due to the above outlined complexities generative learning algorithms are generally out of reach for volumetric images: either too expensive to construct or rely on simplistic assumptions about the joint data distributions. Further, generative learning approaches are focused on producing the minimum variance, rather than prediction rules for the separation of classes. On the other hand, discriminative methods are trying to directly learn separation boundaries to partition classes [85, 137, 12]. This is ensured in MAP (maximum a posteriori) estimation by the fact that a discriminative estimator converges to the conditional probability density that minimizes the classification loss. During inference, the model is fitted to unseen images thereby hypotheses are being evaluated while iterating though the parameter space, and the target prediction is achieved by the maximization of the following objective function:

$$\boldsymbol{\theta}^*, \mathbf{M}^* = \underset{\boldsymbol{\theta}, \mathbf{M}}{\arg\max}\, p\left(\boldsymbol{\theta}, \mathbf{M}|I\right) \tag{3.7}$$

In order to simplify the objective function in Eq. 3.7, we propose decomposing the argument:

$$p\left(\boldsymbol{\theta}, \mathbf{M}|I\right) \approx \underbrace{p\left(\boldsymbol{\theta}|I\right)}_{\text{global pose}} \cdot \underbrace{p\left(\mathbf{M}|\boldsymbol{\theta}, I\right)}_{\text{deformable shape}} \tag{3.8}$$

The approximation transforms the segmentation problem into a sequence of two simpler estimation tasks in a coarse-to-fine fashion: global search and estimation of rigid object parameters (Section 3.2.1) and free form deformation of lumen boundaries (Section 3.2.2). Furthermore this decomposition matches the hierarchical model structure we have introduced in Section 3.1.

3.2.1. Discriminative Learning Techniques

According to the above reasoning we express the parameter estimation (Eq. 3.8) as a discriminative classification task to produce the posterior probability $p\left(\boldsymbol{\theta}|I\right)$ learned from image features during training.

An image I is most often defined as a mapping from d-dimensional space to a scalar:

$$I : \Omega \to \mathbb{R}, \quad \Omega \in \mathbb{N}^d \tag{3.9}$$

Images are representing a measurement of some physical quantity (Section 2.2) in a uniform grid of voxels in volumetric ($d = 3$) images (pixels for $d = 2$ planar images). Intensities of the voxel values are proportional to the measured physical quantity. In digital images the intensities as well as the spatial sampling is discretized.

We aim to discriminatively learn a binary, foreground-background classifier

$$H(V) = p(y|V) \tag{3.10}$$

to be used to evaluate image regions V, where $V \subseteq I$. Here the labeling $y \in \{-1, +1\}$ is describing the probability $p(y = +1|V)$ that the image region V contains the object of interest (foreground: a positive sample) and $p(y = -1|V)$ is the probability of image patch V not containing the object (belongs to the image background: negative sample).

Discriminative learning methods include support vector machine (SVM), boosting, randomized decision forests and neural networks. Thanks to its high generalization performance, in the rest of our investigation we will use variants of boosting as the supervised learning algorithm of our choice. Boosting is described in the next paragraph, while in the following paragraphs we will explain the different image-based features used for learning.

Boosting Algorithms

In this paragraph we show how a boosting procedure is able to learn a prediction function $H(V) = p(y|V)$ (Eq. 3.10) to minimize the mis-classification loss.

AdaBoost AdaBoost was introduced by Schapire and Freund in 1995 [49]. The basic principle is to boost the performance of "weak" learners to transform them into a "strong" learning algorithm.

Given a training set $S = \{(x_1, y_1), \cdots, (x_m, y_m)\}$ $x_i \in X, y \in \{+1, -1\}$ where each sample x_i belongs to some domain X, and each label y_i in some label set Y. The AdaBoost algorithm learns a "strong" classifier ($H(x)$) as a linear combination of "weak" classifiers (h_t):

$$H(x) = sign\left(\sum_{t=1}^{T} \alpha_t h_t(x)\right) \tag{3.11}$$

The only criterion against weak learners is that each has to perform better than random guessing (if one performs worse than random guessing a sign-flip allows it to be incorporated). We sequentially apply the weak learner to a repeatedly updated version of the data, thereby learning a sequence of weak classifiers $h_t(x)$ ($t = 1, 2, \ldots, T$). Here $\alpha_1, \alpha_2, \ldots, \alpha_T$ are the weights for the "weak" classifiers computed by boosting.

At step t of the iteration, the samples mis-classified by the previously trained $h_{t-1}(x)$ are assigned an increased weight, whereas the weights w_i $(i = 1, 2, \ldots, m)$ of the correctly classified training samples are decreased. This results in a iterative increase of influence of the samples that are difficult to classify. Effectively instructing the next classifier to focus on samples "overlooked" by earlier phases [50]. The final classifier

Algorithm 1: The adaptive boosting (AdaBoost) algorithm introduced by Freund and Schapire in [49]

Data: A training set $S = \{(x_1, y_1), \cdots, (x_m, y_m)\}; x_i \in X, y \in \{+1, -1\}$
Data: Number of iterations T
Initialize weight vector $w_1(i) = 1/m \quad i = 1, 2, \ldots, m$;
for *each iteration* $t = 1, 2, \ldots, T$ **do**
  Select weak classifier $h_t : X \to \{+1, -1\}$ to fit the weight distribution $\vec{w}_t$ with minimum error;
  Compute error using mis-classification loss:

$$\epsilon_t = \frac{\sum_{i=1}^{m} w_i sign\left[y_i \neq h_t\left(x_i\right)\right]}{\sum_{i=1}^{m} w_i}$$

  Update: $\alpha_t = log\left(\frac{1-\epsilon_m}{\epsilon_m}\right)$;
  for *each training sample* $i = 1, 2, \ldots, m$ **do**

$$w_{t+1}(i) = w_t(i) \cdot e^{\alpha_t \cdot sign[y_i \neq h_t(x_i)]}$$

Result: $H(x) = sign\left[\sum_{t=1}^{T} \alpha_t h_t\left(x\right)\right]$

$H(x)$ is the weighted average of the weak learners $h_t(x)$. AdaBoost has desirable properties, convergence of the scheme is guaranteed if $\epsilon_t < \frac{1}{2}$ with the training error approaching zero, and strong bounds for the generalization performance were also proven to help avoid over-fitting [50]. The training procedure for AdaBoost is shown schematically in Algorithm 1.

Probabilistic Boosting Tree If the distribution of the data set x_i is complex, the error ϵ_t approaches $\frac{1}{2}$ quickly thereby rendering converge of AdaBoost slow. To address this limitation, Zu [193] proposed probabilistic boosting tree (PBT) based on a divide and conquer strategy to keep the complexity of the training distribution tractable. Algorithm 2 illustrates the procedure to train PBT. During training, PBT is recursively building a tree (Figure 3.6a). For each node of the tree a strong classifier is learned, using e.g. AdaBoost with an early termination $\theta = 0.45$. All training samples of this node are evaluated with the currently learned classifier and an ϵ threshold to control over-fitting. The response of a strong classifier at sample x is denoted as

Algorithm 2: The probabilistic boosting-tree training procedure as introduced by Zhuowen Tu in [193]

Data: A training set

$$S = \{(x_1, y_1, w_1), \cdots, (x_m, y_m, w_m)\} \quad x_i \in X, y \in \{+1, -1\}, \sum_i w_i = 1$$

Data: Maximum tree depth L
Data: confusion tolerance ϵ (e.g. $\epsilon = 0.1$)
Data: early exit threshold θ (e.g. $\theta = 0.45$)
compute the empirical distribution $\hat{q}(y) = \sum_i w_i \delta(y_i = y)$;
while *current tree depth* $< L$ **do**
  On the training set S, train a strong classifier with a boosting algorithm with T weak classifier and exit early if $\epsilon_t > \theta$;
  Initialize two empty sets S_{Left} and S_{Right};
  For each sample (x_i, y_i) compute the probability $q(+1|x_i)$ and $q(-1|x_i)$ using the learned strong classifier;
  if $q(+1|x_i) - \frac{1}{2} > \epsilon$ **then**
    $(x_i, y_i, 1) \rightarrow S_{Right}$;
  else
    if $q(-1|x_i) - \frac{1}{2} > \epsilon$ **then**
      $(x_i, y_i, 1) \rightarrow S_{Left}$;
    else
      $(x_i, y_i, q(+1|x_i)) \rightarrow S_{Right}$;
      $(x_i, y_i, q(-1|x_i)) \rightarrow S_{Left}$;
  Normalize all weights of the samples in S_{Left}, repeat the procedure recursively;
  Normalize all weights of the samples in S_{Right}, repeat the procedure recursively;

follows: $q(+1|x) = \frac{e^{2H(x)}}{1+e^{2H(x)}}$ and $q(-1|x) = \frac{e^{-2H(x)}}{1+e^{-2H(x)}}$ and $\delta(x) = \begin{cases} 1, & x = \text{True} \\ 0, & \text{otherwise} \end{cases}$. Based on this, samples are assigned to the left or right sub-trees, while confusing samples failing this test are assigned to both children. Operating under this scheme, positive and negative samples are naturally clustered into sub-trees and thus reducing the complexity of the training distribution. In contrast to AdaBoost the tree structure preserves the order of the learned decisions (features), that may correspond to semantic patterns in the data. Tree depth and the T number of weak learners per node being two other parameter influencing over-fitting. Each weak learner is encoded as a pair of a binary histogram of polarities (α_t) over the responses during training and the feature identifier (Fig. 3.6b).

During inference (shown in Algorithm 3) PBT is evaluating the tree starting at its root node. Child nodes are trying to refine or "correct" the answer of the current node. It is important to note that boosting predicts not only a label y but also computes a probability score of confidence $p(y|x)$.

Algorithm 3: Evaluation of the probabilistic boosting-tree during inference as introduced by Zhuowen Tu in [193]

Data: Given tree node N
Data: Given sample x
compute $q_N(+1|x)$ and $q_N(-1|x)$ using the learned classifier at current tree node N;
if $q(+1|x) - \frac{1}{2} > \epsilon$ **then**
  $\tilde{p}_{Right}(y) = H_{Right(N)}(x, y)$;
  $\tilde{p}_{Left}(y) = \hat{q}_{Left(N)}(y)$;
else
  if $q(y+1|x_i) - \frac{1}{2} > \epsilon$ **then**
    $\tilde{p}_{Right}(y) = \hat{q}_{Right(N)}(y)$;
    $\tilde{p}_{Left}(y) = H_{Left(N)}(x, y)$;
  else
    $\tilde{p}_{Right}(y) = H_{Right(N)}(x, y)$;
    $\tilde{p}_{Left}(y) = H_{Left(N)}(x, y)$;
$\tilde{p}_N(y|x) = q_N(+1|x) \cdot \tilde{p}_{Right}(y) + q_N(-1|x) \cdot \tilde{p}_{Left}(y)$;
Result: $H_N(x, y) = \tilde{p}_N(y|x)$ at tree node N

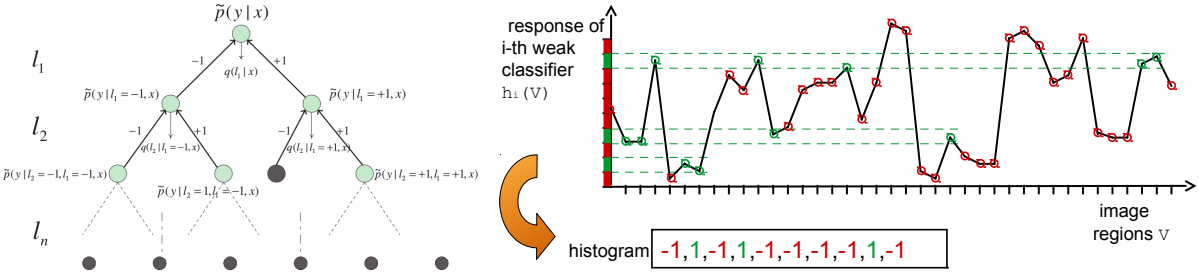

(a) (b)

Figure 3.6.: **Left**: Illustration of the probabilistic decisions stored in the tree. Each node corresponds to a strong classifier. Dark nodes are leaves. Reproduced from [193]. **Right**: Weak classifiers are encoded as a binary histogram of polarities (α_t).

Image-based Features

Image features are knowledge or evidence about an image. There is a large variety of image features that have been introduced in the pattern recognition literature. Prominent image feature descriptors are HoG [27], SIFT [110] and SURF [9]. These features provide high detection rates at the expense of computational time. We have seen in the previous examples that boosting only demands weak evidence from features. As boosting methods are very efficient at feature selection and picking discriminative features, in our investigation we prefer image features that are fast and easy to compute instead of being sophisticated constructs. Such features Haar-wavelet like templates, local binary patterns ([141]) and steerable feature patterns. In the next paragraphs we focus on introducing Haar-like and steerable features. Feature pool in a window centered around an image location with thousands of feature responses collected in a feature bank.

Haar-like features To represent image appearance, Haar wavelet like features have been reported as early as 1997 by Oren et al. [144] for pedestrian detection. In their seminal work, Viola and Jones applied them successfully to face detection [198] and Zheng et al. [212] extended the concept from 2D images to 3D (Figure 3.7). The response of a Haar feature is defined as the difference of the sum of intensities in neighboring cuboid regions. To increase the number of samples, the filter templates may be mirrored, translated, flipped or rotated by multiples of 90^o. On the one hand the concept appears rather simple and the responses are not rotationally invariant. On the other hand thousands of such features extracted in a local search window and filtered through boosting to select the most discriminative ones appears to enjoy a high predictive power for visual patterns in various computer vision and medical image analysis tasks [144, 198, 212, 83, 177, 200, 209, 178] for the last decade and half. We hypothesize that the robustness of Haar features is a result of operating on relative intensity changes instead of absolute values.

The second contributing factor to the success of Haar-like features is computational efficiency. Integral images (or summed area tables as reported in computer graphics literature) provide an efficient way to compute Haar-like features (see Figure 3.8). For a 3D volume, the summed area table $\mathcal{SAT}$ at image location (x, y, z) contains the sum of pixel values above and to the left of (x, y, z), inclusive (assuming the image origin lies in the upper left corner):

$$\mathcal{SAT}(x, y, z) = \sum_{x=1}^{Width} \sum_{y=1}^{Height} \sum_{z=1}^{Depth} I(x, y, z) \tag{3.12}$$

Using this formulation, it becomes obvious how to compute the value of 2D region A in Figure 3.8: $\sum A = \mathcal{SAT}(x_1, y_1) - \mathcal{SAT}(x_1, y_0) - \mathcal{SAT}(x_0, y_1) + \mathcal{SAT}(x_0, y_0)$. Further, it is possible to compute the response of any Haar-like feature as a matter of a few additions and subtractions. Additionally, the $\mathcal{SAT}$ is computed only once and reused during the computation of all feature responses from that image.

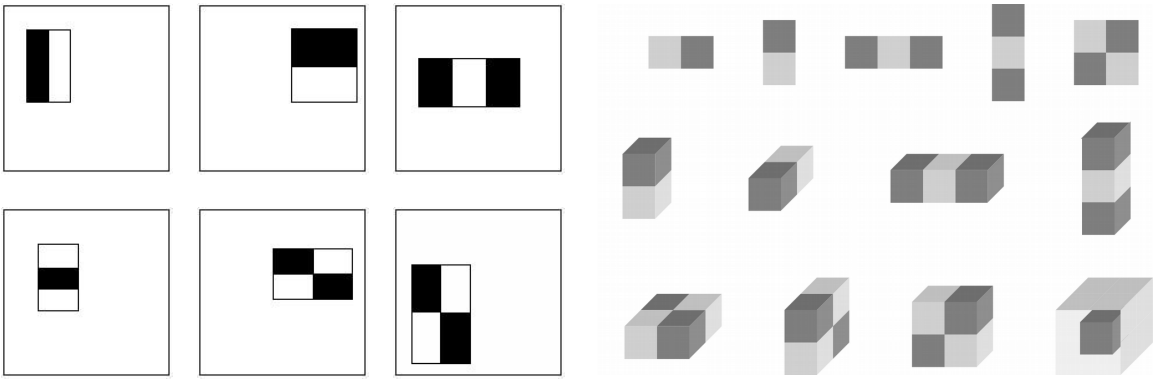

Figure 3.7.: Possible Haar-like 2d and 3d feature templates in a search window. The feature response is the difference of the sum of intensities in the dark and bright regions. Reproduced from [34].

Steerable features Computation of integral images and thus Haar features is only efficient parallel the image axes. Oblique or rotated templates would require expensive resampling of the original image. Zheng et al. [212] introduced steerable features to allow efficient capture of the orientation and scale of objects though a non-uniform grid sampling pattern. In contrast to Haar features, steerable features are naturally scalable and easy to rotate as shown in Figure 3.9. At each sampling point simple local features (e.g. voxel intensity, gradient) are extracted thereby capturing the distribution of orientation and scale at the sampling points.

For the parameterization of concrete hypothesis $[\{t_x, t_y, t_z\}, \{\alpha, \beta, \gamma\}, \{s_x, s_y, s_z\}]$ (e.g. from an aorta part in Eq. 3.1) the sampling patterns are centered at $\{t_x, t_y, t_z\}$. The orientation of the sampling axes are aligned with the local rotation factors $\{\alpha, \beta, \gamma\}$ and the size of the sampling grid is dictated by the scaling coefficients

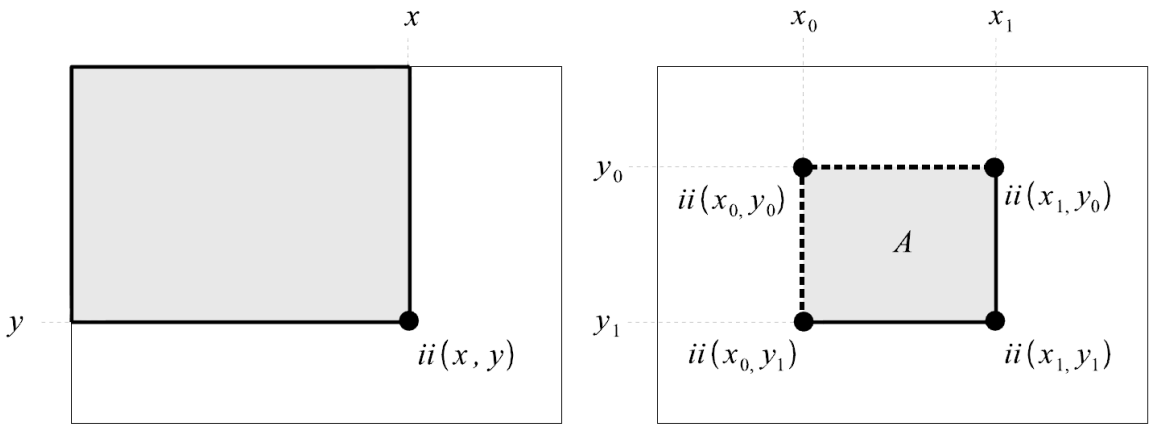

Figure 3.8.: A pixel (x, y) of the $\mathcal{SAT}$ summed area table (denoted ii in the figure) contains the sum of pixels above and to the left of (x, y), inclusive.

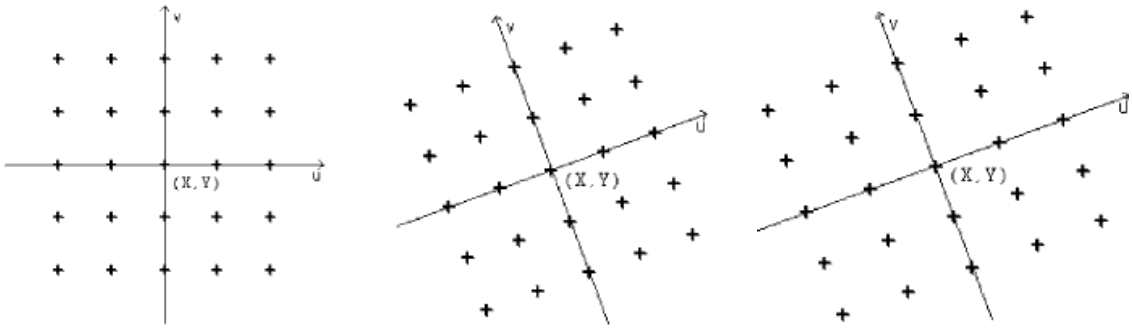

(a) (b) (c)

Figure 3.9.: Sampling points of a steerable feature in 2D. Sampling locations are denoted by +. **Left**: Pattern centered at location (x, y), **Middle**: Pattern additionally oriented to γ, **Right**: Next, the pattern scaled proportional to scaling parameters (s_x, s_y). Reproduced from [212].

$\{s_x, s_y, s_z\}$. The following 24 features are extracted at each sampling location (x, z, y): I, $\sqrt{I}$, $\sqrt[n]{I}$, I^2, I^3, $log(I)$, $\|g\|$, $\sqrt{\|g\|}$, $\sqrt[3]{\|g\|}$, $\|g\|^2$, $\|g\|^3$, $log(\|g\|)$, μ, $\sqrt{\mu}$, $\sqrt[3]{\mu}$, μ^2, μ^3, $log(\mu)$, g_x, g_y, g_z, $n_x \cdot g$, $n_y \cdot g$, $n_z \cdot g$ similar to Zheng et al. [212]. Where at a sampling location (x, z, y), I is the voxel intensity, $g = (g_x, g_y, g_z)$ the local intensity gradient and $\mu = \arccos(n_z \cdot g)$ the angle between the gradient g and the z axis of the object-oriented local coordinate system. Thus the feature response consists of $24 \times N^3$ values where N is the number of sampling point in one direction.

Marginal Space Learning

In this section we have looked at the $p(\boldsymbol{\theta}|I)$ estimation sub-task from Eq. 3.8. This step has to be carried out for each part of the vessel tree model (Eq. 3.2) and involves prediction of nine parameters per object (Eq. 3.1).

The exhaustive search of the nine dimensional parameter space would be prohibitively expensive. To reduce the high computational demands, Zheng et al. [212] introduced an elegant sequential [32] sampling strategy: marginal space learning (MSL). MSL is based on the observation that the nine dimensional parameter space is inherently clustered in many object detection problems. Moreover, to eliminate large parts of the search space MSL subdivides the original parameter domain $\sum$ into subsets of spaces with increasing dimensionality [199]:

$$\sum_1 \subset \sum_2 \subset \cdots \subset \sum_n \equiv \sum \tag{3.13}$$

This means that the classification task in $\sum_{i+1}$ is trained in a much smaller parameter domain than in $\sum_i$. For object pose estimation the search space is decomposed in the following manner: in the first phase only position hypotheses are regarded

$\sum_1 = \{t_x, t_y, t_z\} \in \mathbb{R}^3$ and the most probable candidate locations are passed on, in the second phase the search is augmented with rotational parameters at the candidate locations $\sum_2 = \{t_x, t_y, t_z, \alpha, \beta, \gamma\} \in \mathbb{R}^6$ and finally the different anisotropic scales are searched in $\sum_3 = \{t_x, t_y, t_z, \alpha, \beta, \gamma, s_x, s_y, s_z\} \in \mathbb{R}^9$. Between the subsequent phases of computations typically $50 - 100$ of the detection candidates with highest probability are preserved and propagated to the next level.

3.2.2. Statistical Shape Models

As we have seen in the previous Section 3.2.1, model-based estimation of rigid objects is well established. However the challenges presented by the estimation of deformable models ($p(\mathbf{M}|\boldsymbol{\theta}, I)$ from Eq. 3.8) require a different tool set. One desire against deformable models is to confine the search to characteristic variations of the object class. This is especially true for organs where topological changes are not expected in the patient population. The most influential result in statistical shape analysis may be the 1995 work of Cootes et al. [20] introducing active shape models (ASM).

In order to learn prior knowledge about patient populations ASM employs point distribution models (PDM) to encode shape information, and captures domain specific statistical variation. A PDM describes a shape by defining a number of points on the surface. For a 3D shape with n landmark points this leads to a vector $\mathbf{x}$:

$$\mathbf{x} = [x_1, x_2, \ldots, x_n, y_1, y_2, \ldots, y_n, z_1, z_2, \ldots, z_n]^T \qquad \mathbf{x} \in \mathbb{R}^{3n} \tag{3.14}$$

The first step of building a shape model is alignment of shapes. The goal of alignment is to establish a coordinate reference, to examine the shape statistics. This is achieved by filtering out all translational, rotational and scaling effects. To remove the variance in terms of similarity transform from the training shapes, a shape metric needs to be defined.

The most commonly used shape metric is the procrustes distance [20]. The procrustes shape metric D is least-squares type of distance metric [182] to describe the translational, rotational and scaling differences between two shapes $\mathbf{x}_1$ and $\mathbf{x}_2$. It is a precondition that the two shapes consist of the same number of points n and have an identical point correspondence.

$$D^2 = \sum_{j=1}^{n} \left[(x_{j1} - x_{j2})^2 + (y_{j1} - y_{j2})^2 + (z_{j1} - z_{j2})^2 \right] \tag{3.15}$$

First the centroid of the respective shapes is computed:

$$(\bar{x}, \bar{y}, \bar{z}) = \left(\frac{1}{n} \sum_{j=1}^{n} x_j, \frac{1}{n} \sum_{j=1}^{n} y_j, \frac{1}{n} \sum_{j=1}^{n} z_j \right) \tag{3.16}$$

Scaling is estimated through the size metric (using e.g. the 2-norm) based on the centroids:

$$S(\mathbf{x}) = \sqrt{\sum_{j=1}^{n} [(x_j - \bar{x})^2 + (y_j - \bar{y})^2 + (z_j - \bar{z})^2]} \tag{3.17}$$

After the two shapes are normalized in scale, translation is estimated through the centroids. To estimate the rotation between the two shapes, singular value decomposition (SVD) is used. Re-arranging $\vec{\mathbf{x}}_1$ and $\vec{\mathbf{x}}_2$ into $N \times 3$ matrices X_1, X_2 allows to perform SVD on $X_1^T X_2$ to calculate UDV^T. The rotation matrix for optimal alignment equals to VU^T [182].

Even though a closed-form analytic solution exists [74, 194], the alignment of the training set of shapes is computed iteratively through the generalized procrustes analysis (GPA) [56]. GPA involves four steps [182]:

1. Choose an initial estimate for the mean shape, e.g. $\mathbf{x}_1$, the first shape in the training set

2. Align all other training shapes to the current mean shape using the distance metric outlined above.

3. Re-estimate the mean shape from the newly aligned shapes

4. Iterate starting with 2) until convergence of the mean shape.

If the mean shape was not changed significantly during an iteration, the scheme is assumed to has converged and the shape alignment is complete. With the N aligned shapes, the procrustes mean shape can be expressed:

$$\bar{\mathbf{x}} = \frac{1}{N} \sum_{j=1}^{N} \mathbf{x}_j \tag{3.18}$$

With alignment of the training set of shapes $\vec{\mathbf{x}}_1, \vec{\mathbf{x}}_2, \ldots, \vec{\mathbf{x}}_N$ to the reference frame of the mean shape $\bar{\mathbf{x}}$, we may proceed to the next task: capturing the distribution of shape variation within that frame. The key insight from Cootes et al. [20] was to state that neighboring points of the PDM do not move independently across subjects – the authors have hypothesized that the landmark points are partially correlated. With the further assumption that the position of the landmarks follows a Gaussian distribution, we may compute the $3n \times 3n$ covariance matrix Σ:

$$\Sigma = \frac{1}{N} \sum_{i=1}^{N} (\mathbf{x}_i - \bar{\mathbf{x}})(\mathbf{x}_i - \bar{\mathbf{x}})^T \tag{3.19}$$

Using principal component analysis (PCA) on the symmetric matrix C, the eigenvalues λ_i and eigenvectors ϕ_i ($i = 1, 2, \ldots, 3N$) may be computed. The eigenvectors

corresponding to the largest eigenvalues describe the highest variation of landmarks. Thus, it is possible to approximate Σ with a matrix $\Phi = [\phi_1 \phi_2 \dots \phi_t]$ composed of the column eigenvectors (modes) corresponding to the t largest eigenvalues [20, 182, 25]. Using Φ it becomes possible to synthesize any instance $\mathbf{x}_A$ in the shape space of the training set with the following weighted linear combination:

$$\mathbf{x}_A \approx_t \bar{\mathbf{x}} + \Phi \mathbf{b} = \bar{\mathbf{x}} + \sum_{i=1}^{t} \phi_i b_i \tag{3.20}$$

where $\mathbf{b} = (b_1, b_2, \dots, b_t)^T$ is composed of model parameters describing the deformation (weights of principal components/eigenvectors). To confine $\mathbf{b}$ within three standard deviations of plausible shapes seen during model building, the constraint $3\sqrt{\lambda_i} \geq |b_i|$ is enforced during inference through regularization.

In summary, the learned statistical shape model consists of the mean shape and modes of variation $(\bar{\mathbf{x}}, \Phi)$.

3.2.3. Model Estimation - Segmentation

In supervised learning two stages are distinguished: training and inference. During the offline training procedure the database of labeled data (in our case a set of annotated 3D cardiac MR volumes) is processed with statistical learning algorithms to build "knowledge" in a compact form. During inference the "knowledge" is applied to an unseen volume to estimate model parameters.

Database Guided Model Estimation

We have previously developed [199, 153] a fast, machine learning based method to automatically extract the aortic lumen from 3D MR volumes. Here we will explain this segmentation algorithm.

Substituting Eq. 3.2 into the first term on the right hand side of Eq. 3.8 yields:

$$p\left(\boldsymbol{\theta}|I\right) = p\left(\theta_{Ro}, \theta_{Ar}, \theta_{Br}, \theta_{Lc}, \theta_{Ls}|I\right), \tag{3.21}$$

and we may write the complete pose parameter estimation as an optimization:

$$\begin{aligned} \boldsymbol{\theta}^* &\equiv [\theta^*_{Ro}, \theta^*_{Ar}, \theta^*_{Br}, \theta^*_{Lc}, \theta^*_{Ls}] \\ &= \underset{\theta_{Ro}, \theta_{Ar}, \theta_{Br}, \theta_{Lc}, \theta_{Ls}}{\arg\max} p\left(\theta_{Ro}, \theta_{Ar}, \theta_{Br}, \theta_{Lc}, \theta_{Ls}|I\right) \end{aligned} \tag{3.22}$$

where $\boldsymbol{\theta}^*$ represents the optimal pose parameters of the aorta model parts given a 3D MR volume I.

Unfortunately the joint estimation problem in Eq. 3.22 does not have an analytic solution in general. We address this by decomposing the argument, to be estimated sequentially.

By analyzing the database of our annotated volumes, we have observed that the aortic root and arch appear to be the most distinctive objects to be detected. However, their relative pose with respect to each other is strongly scattered due to disparate AAo morphology of patients. With differences in MRI field-of-view their position in I is also variable. Thus search for $\{Ro, Ar\}$ is performed independently, in the whole image I. On the other hand, the supra-aortic arteries are almost always branching off the same arch region and it makes sense to represent the prior knowledge of this anatomic dependency as spatial constraints (reduced search ranges) in our model. The same principle is true for the stented CoA region, that is located at the aortic isthmus with its pose in low variance relative to θ_{Ar}. This allows for a sequential decomposition, thus we may rewrite the argument of Eq. 3.22:

$$\begin{aligned} p\left(\theta_{Ro}, \theta_{Ar}, \theta_{Br}, \theta_{Lc}, \theta_{Ls}, \theta_{St}|I\right) = \\ p\left(\theta_{Ro}|I\right) p\left(\theta_{Ar}|I\right) \prod_{p_i \in \{Br,Lc,Ls,St\}} p\left(\theta_{p_i}|\theta_{Ar}, I\right) \end{aligned} \tag{3.23}$$

Anatomic dependencies between the parts allows us to reduce the search-space, and focus only on the most probable locations/poses during search, formalized in:

$$p\left(\theta_{p_i}|\theta_{Ar}, I\right) = f(\theta_{p_i}|\theta_{Ar}) p\left(\theta_{p_i}|I\right) \tag{3.24}$$

for parts $o_i \in \{Br, Lc, Ls, St\}$. In other words, we include a pair-wise prediction weight $f(\theta_{o_i}|\theta_{Ar})$ describing the likelihood of pose of o_i given the known pose of the aortic arch [177].

The vessel part estimation is expressed as the inference of the pose parameters from the MR volumes. To estimate the posterior distributions, we propose to use discriminative classifiers. $P(\theta|I) = f(+1|\theta, I)$ is the posterior probability of object presence at θ in a given image I, where f is the learned detector model (fitted using Probabilistic Boosting Tree [193] and 3D Haar-like and Steerable features). In order to efficiently search the 9D parameter space of similarity transforms describing a pose, we follow the sequential sampling strategy consistent with MSL:

$$p\left(\theta_p|I\right) = p(\vec{\mathbf{t}}_p|I) p(\vec{\mathbf{r}}_p|\vec{\mathbf{t}}_p, I) p(\vec{\mathbf{s}}_p|\vec{\mathbf{r}}_p, \vec{\mathbf{t}}_p, I) \tag{3.25}$$

thereby first focusing on location estimation, followed by orientation estimation at the most likely locations and subsequently estimation of object scale. The pair-wise spatial anatomic constraints ($f(\theta_i|\theta_j)$, the priors) are modeled as Gaussian distributions, that are aggregated over the available training data. Noting that Eq. 3.22 is similar to the the multi-object detection problem discussed in the context of the integrated detection network (IDN) framework [177], hence we have implemented the proposed solution to Eq. 3.7 in IDN.

On unseen images, the learned model is applied in a sliding window manner to detect the anatomic parts. In the hierarchical scheme from Eq. 3.24 we first estimate the pose of Ro and Ar (performed on the whole MR volume), then based on θ_{Ar} and the learned anatomic constraints the search spaces for the rest of the parts are predicted around the most likely locations. In the proximity of these candidate locations a localized search follows for $\{Br, Lc, Ls, St\}$.

Lumen Surface Estimation

The second phase of the segmentation procedure estimates the lumen boundaries as densely tessellated surfaces. Similar to the ASM [20] framework, landmark points in a PDM are displaced under regularization constraints (Section 3.2.2) in an iterative manner. This relies on the bounding boxes (θ_p) of the anatomic "skeleton" computed in the previous step, to initialize shape models and apply learning based boundary detectors [212, 216, 177] to refine them towards the true lumen boundaries. Similar to Eq. 3.21, the deformable shape search is decomposed to individual parts (Eq. 3.4):

$$p\left(\mathbf{M}|\boldsymbol{\theta}, I\right) = p\left(M_{Ro}, M_{Ar}, M_{Br}, M_{Lc}, M_{Ls}|\theta_{Ro}, \theta_{Ar}, \theta_{Br}, \theta_{Lc}, \theta_{Ls}, I\right) \tag{3.26}$$

and estimated sequentially for each part:

$$p\left(M_{Ro}, M_{Ar}, M_{Br}, M_{Lc}, M_{Ls}|\theta_{Ro}, \theta_{Ar}, \theta_{Br}, \theta_{Lc}, \theta_{Ls}, I\right) = \prod_{m_i \in \{Ro,Ar,Br,Lc,Ls\}} p\left(M_{m_i}|\theta_{m_i}, I\right) \tag{3.27}$$

To initialize the individual boundaries, we are warping the learned mean shape (Eq. 3.18) to the bounding box defined by the estimated similarity transform of respective model part p:

$$\mathbf{x}_p = f_{\vec{\mathbf{s}}_p} \circ f_{\vec{\mathbf{r}}_p} \circ f_{\vec{\mathbf{t}}_p}\left(\bar{\mathbf{x}}\right) \tag{3.28}$$

where $f_{\mathbf{s}_p}$, $f_{\mathbf{r}_p}$ and $f_{\mathbf{t}_p}$ perform the scaling, rotation and translation according to Eq. 3.25, thereby linking the rigid pose to the initialization of the deformable boundary [106].

Initialization of the shape subspace occurs in a similar way as rigid parameter estimation, and first proceeds by detecting a shape in a learned PCA sub-space [212, 106]. To describe the parameters in the shape space, a PCA detector is trained discriminatively to estimate the first three b_1, b_2, b_3 shape coefficients using PBT and Steerable features sampled at the vertices of the surface [177]:

$$(b_1, b_2, b_3)_p = \underset{-3\sqrt{\lambda_i} \leq b_{i_p} \leq 3\sqrt{\lambda_i}}{\arg\max} p(b_1, b_2, b_3|\theta_p, I). \tag{3.29}$$

During inference, the point distribution model is weighted with the estimated b_i following Eq.3.20 and three modes of variation:

$$\mathbf{x}_p = f_{\vec{\mathbf{s}}_p} \circ f_{\vec{\mathbf{r}}_p} \circ f_{\vec{\mathbf{t}}_p}\left(\bar{\mathbf{x}} + \sum_{i=1}^{3} \phi_i b_i\right). \tag{3.30}$$

producing the initial lumen segmentation.

The following step is an iterative free-form refinement of the initial lumen surface mesh regularized by shape prior [106, 177]. The mesh refinement deforms the boundary at the landmark points of the PDM. At each vertex $\mathbf{v}_i$ with surface normal $\mathbf{n}_i$ an offset d_i is estimated for the boundary displacement $\mathbf{v}_i \leftarrow \mathbf{v}_i + d_i\mathbf{n}_i$. While ASM [20]

relied on the strongest gradient along the normal, we have trained a discriminative model to obtain d_i:

$$d_i = \arg\max_{-\tau \leq d_i \leq \tau} p(d_i | \mathbf{v}_i, \mathbf{n}_i, I), \tag{3.31}$$

where τ is the search range along the normal. This update is followed by PCA shape-space projection, a second iteration of boundary displacement and surface smoothing and updating of the normal, n_i.

The walls of the ascending and descending aorta are treated separately. Their pathological morphology and large length variability do not allow for compact statistical representation. The surfaces of the AAo, DAo are assembled from individual circles, that are tracked on axial slices of the volume, to connect the root with the arch (for AAo), and descend from the arch to the diaphragm level (for DAo). Circles are initialized from the previous slice, and the contours are refined by in-plane radial boundary detectors, similar to the ones applied in the shape models [216].

The final lumen model is obtained by merging the separately estimated surfaces. From the lumen surface meshes, four connected centerlines are computed, one for the aorta and three for the supra-aortic arteries ($SAoA$).

The explicit modeling of the stented isthmus was necessitated by the fact that post-stenting 3D MR volumes have a signal drop-out inside the metallic stent, that "hides" the normal appearance of the aortic lumen, even when contrast agent is present (Figure 3.4). To address this, post-operative volumes are detected by checking the histogram of the volume along the center-line of the segmented aortic isthmus. Near-zero intensity regions are signifying the loss of MR signal, and in these cases the θ_{St} detector is applied. The stent is estimated as a linearly tapering tubular surface connecting the transverse arch and the lower descending aorta.

3.3. Computational model of the thoracic aorta

In this section, we would like to introduce the computational model of the thoracic aorta, that was constructed to describe hemodynamic conditions in CoA patients. To provide technical background to our work, in section 3.3.1 we provide a brief review of the literature of image-based hemodynamics computations conducted in connection with CoA and the thoracic aorta. Afterwards, Section 3.3.2 introduces the computational domain of the aortic vessel tree, derived from the segmented lumen surface.

3.3.1. Image-based Computational Modeling

The field of image-based personalized computational hemodynamics was pioneered in 1999 by Taylor et al. [190]. Since then the approach was adapted from vessels of lower extremities through cardiac hemodynamics [187, 130] to cerebral aneurysms of the brain [15, 185].

The first step in an image-based simulation is the definition of the computational domain. For CoA investigation, this is the lumen of the thoracic arterial tree. The aorta (including the ascending and descending parts and the arch together with the trunk of supra-aortic arteries) is segmented to delineate the vascular morphology.

Multiple groups have investigated CoA hemodynamics through computational modeling. Recent studies have suggested that good agreement may be reached between measured and simulated hemodynamic and morphologic indices if subject-specific boundary conditions are employed [51].

Coupling the aorta with a lumped parameter model of the left side of the heart, Kim et al. [91] applies realistic inflow boundary conditions to pre- and post-operative setup of two patients within resting and stress loaded conditions. This personalization scheme was extended by Coogan et al. [19] with elastic vessel wall properties to simulate effects of change of distensibility and stiffness in a virtually implanted stent against virtual surgical CoA repair. Even though development of these state-of-the-art boundary conditions and methods ensure high fidelity, the long computational times ($3-10$ days on a 96 core super computer) pose questions on widespread clinical application. LaDisa et al. [98] applies detailed boundary conditions and a similarly sophisticated simulation procedure, to conclude that stent implantation doesn't notably increase the LV workload. Imaging data was specifically acquired for the study, and potentially difficult to reproduce in standard exams.

A cohort of seven cases is examined by Valverde [195] and colleagues. Arterial in- and out-flow boundary conditions are prescribed from clinical measurements, employing simple heuristics at the supra aortic branches, the authors have reached good agreement of CoA $\triangle P$ at rest and moderate agreement at stress.

Recently a larger study [57] of 13 CoA patients was published. The authors' approach combined pre-operative CMR angiograms and peri-operative fluoroscopy images to define the aorta lumen boundaries. Simulation of pre-operative blood pressure was calculated with remarkable correlation. Furthermore, treatment outcome prediction was performed by adapting the pre-operative geometry with post-stenting fluoroscopy measurement of the restored aorta diameter.

Besides full 3D CFD simulations, reduced order circulation models have been investigated [142]. These models are known for their computational efficacy, and have been successfully applied to various problems [181, 160].

3.3.2. Axisymmetric Arterial Tree Model

MR examination of a coarctation patient usually involves at least two different images as shown in Fig. 3.10a: a 3D thorax scan and planar velocity encoded PC MR flow image (Sec. 2.2). While the 2D slice is later used to estimate personalized blood inflow, the 3D scan is used to segment the lumen surface (Fig. 3.10b). Subsequently the patient-specific lumen morphology is used to construct the domain of hemodynamic computations: along the center-lines, the combined lumen surface is partitioned into 9 segments (Fig. 3.10c). For each linear tapering tube segment the length l and

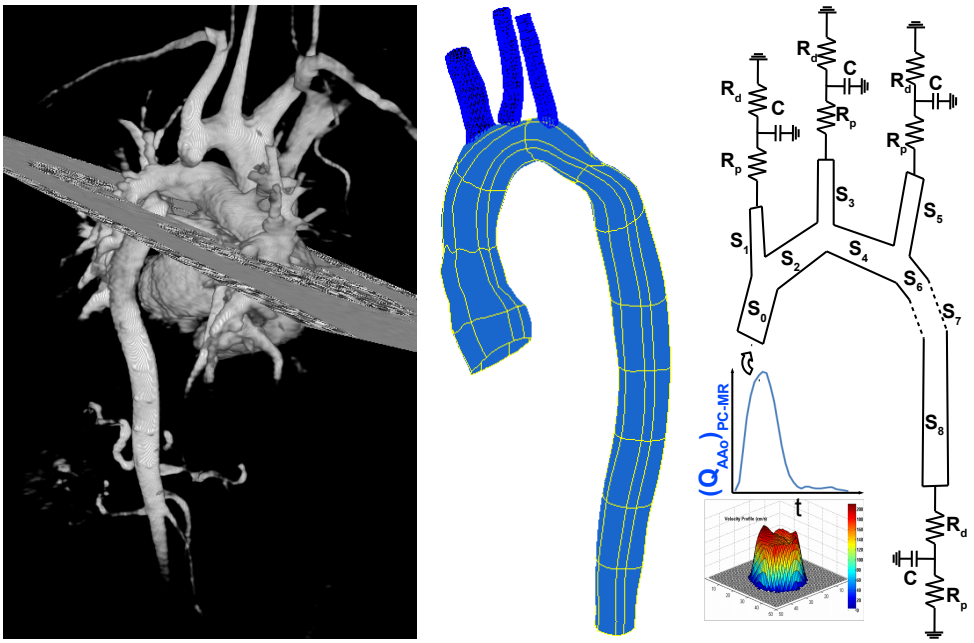

(a) (b) (c)

Figure 3.10.: **a**) Standard CoA MR exam with pair of images: 3D MRA and flow encoded 2D+t PC-MRI. **b**) Combined surface of segmented lumen of thoracic aorta and trunk of main branches. **c**) Semantic view of arterial tree with discrete axisymmetric segments and terminal boundary conditions.

proximal r_{in} and distal r_{out} radii are computed: $S_i = \{l, r_{in}, r_{out}\}, i \in \{0, \ldots, 8\}$ from the combined lumen surface. S_7 is either the CoA narrowing or the stent. The start and end cross-sections of the coarctation were taken as the locations where the radius decreases under 95% of the aorta diameter downstream the left-subclavian trunk, and respectively increases above 95% of the reference value for the diaphragmatic aorta.

3.4. Personalization of the computational model

The modeling apparatus introduced in the previous Section 3.3 requires patient-specific boundary conditions and parameterization to provide personalized assessment. The proposed clinical workflow and model personalization is introduced in this section. Figure 3.11 provides a graphical overview of the computational steps.

Estimation of the Patient-Specific Blood Flow From PC-MRI

To quantify each subject's measured aortic blood flow conditions, a single velocity encoded 2D+t PC-MRI cine image slice is used. These sequences contain through-

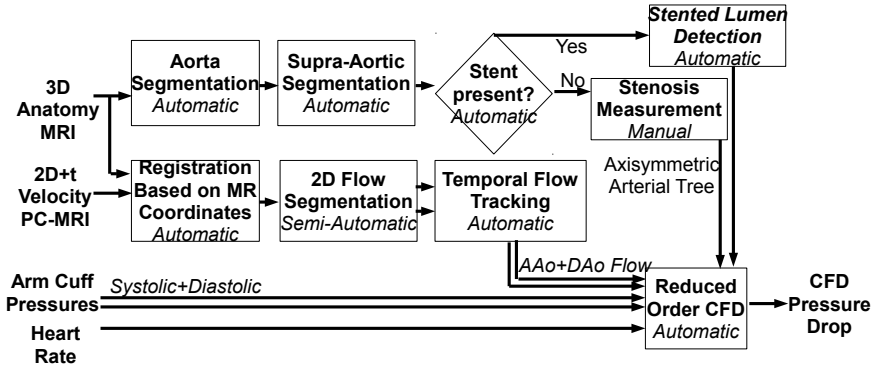

Figure 3.11.: Overview of our personalized image-based quasi 1D hemodynamic simulation workflow.

plane blood flow measurements in an oblique arrangement, intersecting the aorta twice: at the root of ascending aorta and in the region of the descending aorta distal from the CoA (Fig. 3.10a). As both MRI images are acquired with the assumption that the patient does not move in the scanner in between scans, MRI machine coordinates allow for a coarse registration of the MR anatomy and the PC-MR plane. Thus, given the centerline of the aorta calculated from the previous segmentation, delineation of aortic flow boundaries on the PC-MR image plane is initialized using the lumen contour from the 3D surface mesh (Sec. 3.2.3) . The single time-point segmentation is then tracked throughout the cardiac cycle, propagating the contour based on deformable registration[87] of the n time frames in the cine series. In the patches inside each contour, sampling of the PC-MR image is performed at the pixel centers to obtain velocity values over the entire cardiac cycle. These velocity fields are integrated over the area of the patches to derive the measured ascending- and descending aortic blood flow rates (q_{asc} and q_{desc}).

3.4.1. Axisymmetric Quasi 1D CFD

For pressure-drop computations in clinical settings, the total execution time of the algorithm is of paramount importance. Thus we have chosen a reduced-order, quasi 1D approach, which together with terminal windkessel elements represents a reduced-order circulation model for the aorta[2]. The quasi 1D fluid-structure interaction model consists of the mass (Eq. 3.32) and momentum (Eq. 3.33) conservation equations, and a state equation for wall deformation (Eq. 3.34). The vessel wall is modeled as a purely elastic material [160]:

$$\frac{\delta A(x,t)}{\delta t} + \frac{\delta q(x,t)}{\delta x} = 0 \tag{3.32}$$

$$\frac{\delta A(x,t)}{\delta t} + \frac{\delta}{\delta t}\left(\alpha \frac{q^2(x,t)}{A(x,t)}\right) + \frac{A(x,t)}{\rho}\frac{\delta p(x,t)}{\delta x} = K_R \frac{q(x,t)}{A(x,t)} \tag{3.33}$$

[2]Please refer to Appendix C for a complete listing of notation used.

$$p(x,t) = \frac{4}{3}\frac{E \cdot h_i}{r_0}\left(1 - \sqrt{\frac{A_0}{A(x,t)}}\right) + p_0 \tag{3.34}$$

where r_0 is the initial radius corresponding to diastolic pressure p_0. At the outlets, terminal windkessel elements are applied in order to close the system of equations:

$$\frac{\delta p}{\delta t} = R_p\frac{\delta q}{\delta t} - \frac{p}{R_d \cdot C} + \frac{q(R_p + R_d)}{R_d \cdot C}. \tag{3.35}$$

To build the discretized geometric mesh from the center-line and cross-sectional areas, we use an approach similar to previously introduced ones [181], wherein for each vessel of the arterial model, we use several distinct 1D segments S_i with longitudinally varying cross-sectional area values in order to obtain an axisymmetric geometry close to the 3D geometry acquired through MRI (Sec. 3.3.2).

Boundary conditions at the ascending aortic inlet are dictated by the time-varying flow rate q_{asc} computed from PC-MRI (Sec. 3.4).

We are using a finite difference solver with patient-specific fixed time step and explicit stability constraints [84].

In all of our computations we apply a Newtonian rheological model, where the blood density and dynamic viscosity are set to literature-based values for healthy individuals. The following sections describe the estimation of the wall properties and the windkessel parameters at the outlets.

3.4.2. Preoperative model personalization and configuration

The inlet boundary condition is prescribed by the time-varying flow rate determined through PC-MRI (Sec. 3.4), while the estimation of the wall properties and the windkessel parameters at the outlets is performed as described in the following. Physiologically motivated three-element windkessel boundary conditions [184, 197] require estimation of three quantities (two resistances: proximal - R_p, and distal - R_d, and one compliance - C) at each outlet from measured patient data. Mean arterial pressure ($\overline{P_A}$), defined as the average pressure over the cardiac cycle is responsible for perfusion: driving the blood into the distal vessels and ultimately into the tissues. $\overline{P_A}$ is related to the total distal resistance by the following expression: $\overline{P_A} = Q \cdot R$. Here Q is the average flow at a point in the arterial circulation, and R is the total distal arterial resistance. For the aorta, the following equation holds at each supra aortic outlet i: $\overline{P_A} = Q_i \cdot (R_t)_i$, where Q_i is the average flow rate through outlet i and $(R_t)_i$ is the total resistance, which is the sum of the two windkessel resistances ($R_t = R_p + R_d$). In the ascending aorta, $\overline{P_A}$ is estimated from the non-invasive cuff pressures [159], as: $\overline{P_A} = \overline{P_{di}} + \left[\frac{1}{3} + H_R \cdot 0.0012\right] \cdot (\overline{P_{sy}} - \overline{P_{di}})$ where H_R is the heart rate and $\overline{P_{sy}}$ ($\overline{P_{di}}$) are the systolic (diastolic) blood pressures. The time-averaged flow rates at the ascending (Q_{asc}) and at the descending aorta (Q_{desc}) are measured from the PC-MRI slices. Thus the combined flow to the three supra-aortic outlet vessels ($Q_{supra-aortic}$) is determined by $Q_{supra-aortic} = Q_{asc} - Q_{desc}$. We use the square law of

Zamir et al. [213] stating that for the first few branches starting from the aortic root, the flow (Q_i) is distributed to the branching vessels proportionally to the square of the radius. Thus,

$$Q_i = Q_{supra-aortic} \cdot r_i^2 / \sum_{j=1}^{3} r_j^2 \tag{3.36}$$

where r_i is the radius of the supra-aortic branch i. Since the pressure difference between the ascending aorta and the three supra-aortic branches is minimal (the viscous losses are negligible), the same average pressure is used to estimate the total resistance of each supra aortic branch:

$$(R_t)_i = \overline{P_A}/Q_i. \tag{3.37}$$

For the CoA patients, the above assumption does not hold true for the descending aorta because the narrowing at the coarctation site introduces a pressure-drop along the length of the aorta, which can be translated into a flow-dependent resistance $R_c(q)$. Accordingly, the total resistance, which represents the sum of the resistance of the coarctation and that of the outlet windkessel model, is estimated as follows:

$$(R_t)_{desc} + R_c(q) = \overline{P_A}/Q_{desc}. \tag{3.38}$$

One of the assumptions made during the derivation of the reduced-order model is that the axial velocity is dominant and the radial components are negligible. This assumption holds well for normal, healthy vessels, but in case of sudden changes in lumen diameter, e.g. for a narrowing like the coarctation, the radial components can no longer be excluded. Thus, for the coarctation segment we use the previously introduced comprehensive pressure drop model [84]:

$$\begin{aligned} \Delta P = K_v(\omega) R_{vc} q + \frac{\rho K_t}{2A_{DiAo}^2} \left(\frac{A_{DiAo}}{A_c} - 1 \right)^2 |q| q \\ + K_u L_u \frac{\delta q}{\delta t} + K_c(\omega) R_{vc} q \end{aligned} \tag{3.39}$$

where the first term captures the viscous energy losses, the second term captures the turbulent energy losses due to sudden expansion, the third term represents the inertial effect and the fourth term is a continuous pressure-flow component. $K_v = 1 + 0.053 \cdot \omega^2 A_c / A_{DiAo}$ is the viscosity coefficient and $R_{vc} = \frac{8\mu}{\pi} \int_0^{L_c} \frac{1}{r^4(l)} dl$ is the viscous resistance and $L_u = \frac{\rho}{\pi} \int_0^{L_c} \frac{1}{r^2(l)} dl$ is the inertance; $K_c = 0.0018\omega^2$ is a continuous coefficient. Similarly, the morphologic CoA stenosis rate (T_{CoA}) is computed from the segmented lumen surfaces as $T_{CoA} = (1 - A_c/A_{DiAo})$ (see Appendix C for notation). The flow-dependent resistance of the coarctation segment S_7 is computed by averaging

the resistance values of each time frame:

$$R_c(q) = \left(\sum_{1}^{n} \frac{\triangle P(q_{desc}(t))}{q_{desc}(t)} \right) / n \tag{3.40}$$

where $\triangle P(\bullet)$ is computed through Eq. 3.39. For the estimation of compliance values, we first compute the total compliance of the systemic circulation (C_{tot}) similar to Stergiopulos et al. [184]. Next, the compliance of the proximal vessels (C_{prox}) is computed by summing up the volume compliances of each proximal segment. Finally, the total outlet compliance (C_{out}) is determined by subtracting C_{prox} from C_{tot}, which is then distributed to the four outlets based on the cross-sectional area values at the outlets.

An important aspect of blood flow computations with compliant vessels is the estimation of the mechanical properties of the aortic wall. We use a method based on wave-speed computation [142], where the wave-speed c is related to the properties of the aortic wall by the following expression:

$$c = \sqrt{\frac{2}{3\rho} \frac{E \cdot h_i}{r_0}}. \tag{3.41}$$

To estimate the wave speed, we use the transit-time method [77], whereby $c = \triangle x / \triangle t$. Here $\triangle x$ is the distance (measured along the center-line) between the inflow at the aortic root and the outlet at the descending aorta, and $\triangle t$ is the time taken by the flow waveform to travel from the inlet to the outlet location. Once the wave speed is known, for all aortic segments the quantity $\frac{E \cdot h_i}{r_0}$, in Eq. 3.41, is computed as:

$$\frac{E \cdot h_i}{r_0} = \frac{3\rho c^2}{2}. \tag{3.42}$$

The wall properties of all the aortic segments are determined using this equation.

Since the time-varying flow rate (and thus pulse transit information) at the individual supra-aortic branches is not known, a different method is applied for these vessels. The estimation of their wall properties is based on the supposition that arterial bifurcations lead to minimal reflections of forward propagating waves[89]. Hence, first the reflection coefficient at bifurcation k is computed using [134]:

$$\Gamma_k = \frac{Y_p - \sum_i (Y_d)_i}{Y_p + \sum_i (Y_d)_i} \tag{3.43}$$

where Y_p and Y_d represent the characteristic admittance (inverse of the characteristic resistance) of the parent and daughter vessels respectively. Next, the characteristic resistance of the daughter vessel which is a supra-aortic branch is determined by setting Γ equal to 0:

$$R_{supra-aortic} = \frac{R_{aorta-p} \cdot R_{aorta-d}}{R_{aorta-d} \cdot R_{aorta-p}}. \tag{3.44}$$

Finally, the wall properties ($\frac{E \cdot h_i}{r_0}$) for the supra-aortic branch i are determined as [84]:

$$\frac{E \cdot h_i}{r_0} = \frac{3 \cdot Z_i \cdot \pi^2 \cdot r_0^4}{2 \cdot \rho}. \tag{3.45}$$

3.4.3. Postoperative model personalization and configuration

In the post-operative configuration, since the same type of information is available as for the pre-operative configuration, the model personalization is performed similarly. None of the post-operative models had residual coarctations. As a result: (i) The stented coarctation segments are modeled as regular 1D segments, with large stiffness (the wave speed is approx. 15-times higher than the wave speed of a regular healthy aortic segment). Since the wave speed of the stent is fixed and the length is known, the transit time along the stented segment can be computed directly (the stented segment is excluded from the computation of wave speed in Eq. 3.41), (ii) $R_c(q)$ is considered negligible and the total resistance of the windkessel model applied at the outlet of the descending aorta is computed directly from Eq. 3.38.

3.4.4. Virtual stenting configuration

A third configuration considered in this study consists of performing a virtual stenting procedure on the pre-operative aortic model. For prediction of blood pressure drop change after stent implantation, the pre-operative model is altered, by replacing the stenosed segment (S_7) of the arterial tree with a segment of the same length that is interpolating the cross-section information between the diameters of segments S_6 and S_8. This is meant to model the implantation of a straight stent into the aortic isthmus. The inflow rate is identical to the one used in the pre-operative configuration and the model personalization from the post-operative configuration is reused.

3.5. Experiments and Results

To validate our CoA assessment workflow, we have evaluated our models on *in-vivo* patient data. Clinical data was retrospectively collected from cardiac institutes around the world: (i) the FDA approved multi-center COAST [163] (Coarctation of Aorta Stent Trial) trial and (ii) OPBG (Ospedale Pediatrico Bambino Gesù). We have conducted two main experiments, one to quantify the accuracy of 3D lumen segmentation (Section 3.2) and a second one to characterize the blood pressure drop estimation (Section 3.4).

3.5.1. Clinical Protocol

The standard CoA protocol at our clinical partners includes the following: acquisition of MR images of the thorax and aortic flow, measurement of the blood pressure with

catheterization, heart rate, and cuff measurement at the upper extremities.

MR patient data was acquired using a heterogeneous set of protocols and vendors (Siemens, Philips, GE), employing 1.5 *Tesla* scanners. The 3D MR volumes are usually oblique stacks of dimension 256×256 to 512×640 with $56 - 140$ slices, in-plane resolution isotropic $0.605 - 1.562$ mm, slice thickness of $0.889 - 1.8$ mm. Among the 3D volumes were contrast enhanced MR angiogram (CE-MRA) and Balanced Turbo Field Echo (BTFE) acquisition protocols. Patients were at resting conditions during imaging, and the 3D volumes only consisted of a single, static time frame.

The ECG gated Cine PC MR images are typically oblique axial time-series encoding through-plane velocities in the isotropic resolution of $0.742 - 2.083$ mm, dimension 126×144 to 384×512, VENC found in the range of $140 - 300$ cm/s (it has been ensured that velocity magnitude wrap-around was not present in the PC-MR data). The slices are routinely positioned to provide two different aorta cross-sections, one somewhere around the aortic root, the other in the DAo (if there is a stent implant, in the direction of the blood flow below the stent location) as illustrated in Figure 3.10a. Each time-series corresponds to one heart cycle and has $n = 20 - 40$ frames per cycle. The heart rates of the examined patients range from $H_R = 60 - 114$ bpm.

The invasive pressure catheterization was performed in a pullback procedure. The systolic $\overline{P_{sy}}$ and diastolic $\overline{P_{di}}$ cuff measurements were taken at the arms.

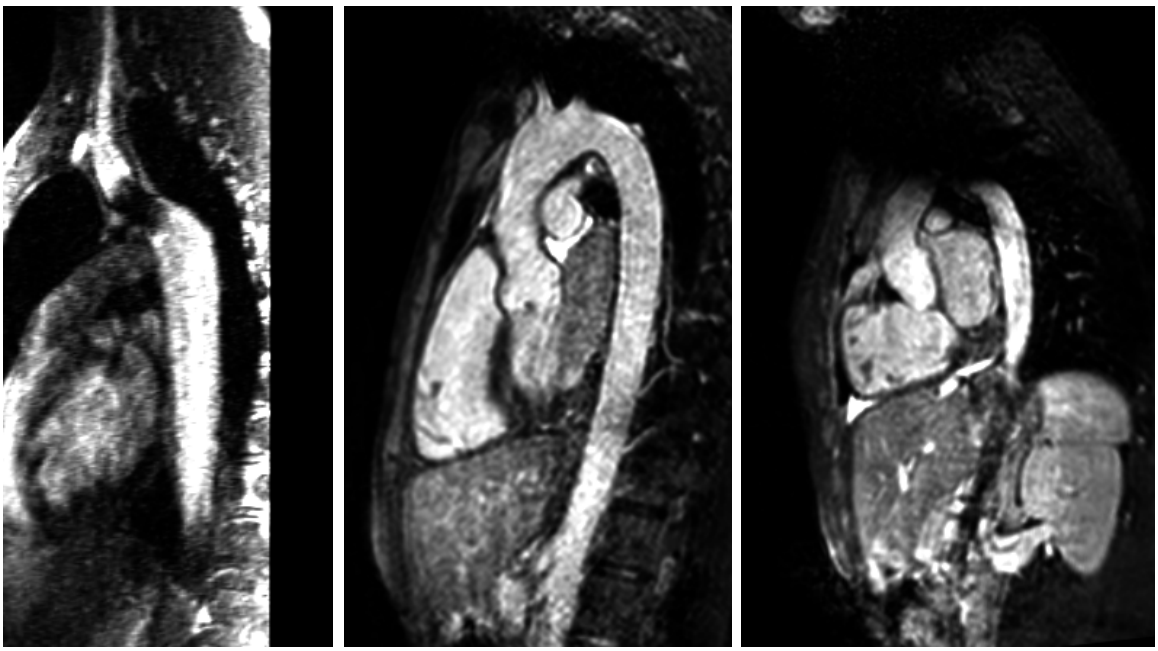

Figure 3.12.: Illustration of heterogeneous image quality and varying field of view of cardiac MRI. **Left**: Signal "drop-out" due to stent implanted in aortic isthmus. **Center**: Oblique acquisition. **Right**: Noisy scan quality around the aortic arch.

3.5.2. Segmentation Experiments

In this section, we evaluate the proposed method for aorta segmentation on 212 volumes of 99 patients. The data sets capture CoA patients who often present co-morbidities, such as various severity of aortic dilation and bicuspid aortic valves. The goal is to demonstrate the performance of the model-based estimation approach by fitting $(\boldsymbol{\theta}, \mathbf{M})$ to patient images. In each volume, the lumen surface of the aorta and main branches were delineated by an expert operator, and converted to a triangular mesh. This annotation was considered as Ground Truth during model training and testing.

All MR studies were performed in supine position of the patient, which allowed the oblique volumes to be resampled to a stack of axial slices, and reduce variance in the aorta appearance before segmentation. The anisotropic volumes were sub-sampled on a $3mm - 1mm$ Gaussian pyramid of uniform grids. The similarity transform of the vessel parts are detected on $3mm$ images, while the boundary detector is run on the finer $1mm$ volume (Table 3.1). The symmetric point-to-mesh [215] distance

E_{p2m}	**Mean±SD** (mm)	**Median** (mm)
aorta $(M_{Ro}, M_{AAo}, M_{Ar}, M_{DAo})$	1.80 ± 0.26	1.82
brachiocephalic trunk (M_{Br})	3.40 ± 1.89	2.90
left common trunk (M_{Lc})	4.59 ± 3.58	3.16
left subclavian trunk (M_{Ls})	4.64 ± 3.33	3.06
complete aortic model	3.00 ± 1.58	2.43

Table 3.1.: Lumen surface segmentation accuracy averaged from four-fold cross validation of 212 3D MR volumes. Displayed as symmetric point-to-mesh [215] distance metric in mm.

metric E_{p2m} is used to measure match in boundary delineation of surfaces. At each vertex of a surface, the closest point (not necessarily a vertex) is computed on the other surface using L_2 (Euclidean) distance. The metric is symmetric, because the calculation is performed in both direction between the two meshes (Ground Truth and detected result).

Moreover, the quantitative capabilities of our system are demonstrated on 32 patients with aortic anomalies (age: $5 - 36$ years, 17 with CoA and 15 with bicuspid aortic valve (BAV) and ascending aortic dilation) by comparing a set of morphological measurements [146] automatically derived by our personalized model to measurements manually extracted by our cardiologist collaborators. The aortic smallest (E_{dmin}) and largest (E_{dmax}) diameters were measured on a plane perpendicular to the aortic center-line at five landmark cross sectional locations (dashed lines in Fig. 2.2a): aortic sinus (**AS**), sino-tubular junction (**STJ**), ascending aorta (**AAO**), transverse arch (**TA**), and descending aorta (**DA**). Table 3.2 summarizes the mean measurement errors for each landmark locations separately.

	AS (mm)	**STJ** (mm)	**AAo** (mm)	**TAA** (mm)	**DAo** (mm)
E_{dmin}	1.61 ± 0.9	2.07 ± 1.5	1.61 ± 1.9 min	1.70 ± 1.2	0.8 ± 0.5
E_{dmax}	1.56 ± 1.3	1.28 ± 1.0	1.56 ± 1.3max	1.34 ± 1.1	0.92 ± 0.6

Table 3.2.: Comparison between manual and model-based clinical diameter measurements at five landmark locations along the aorta (mm).

3.5.3. Experiments on CoA Blood Pressure Drop Estimation

Patient	**Stenting Age**	**Sex**	**Stenosis Rate (T_{CoA})**	*AAo* **inflow change after stenting (MRI)**	*DAo* **outflow change after stenting (MRI)**
#1	18	F	59.14%	−24.96%	15.89%
#3	27	M	37.05%	87.56%	13.45%
#4	12	F	42.86%	7.83%	−2.32%
#5	15	M	37.48%	−32.52%	−6.75%
#6	22	M	41.47%	37.98%[1]	17.75%
#9	11	F	27.61%	14.12%	−1.07%

Table 3.3.: General information on the population of 6 coarctation patients assessed with our blood pressure drop computation method. Flow rate changes are given over a period of one minute.

For the demonstration of the proposed workflow for non-invasive blood pressure drop assessment, we investigated data-sets from 6 CoA patients. From the above mentioned 99 patients, we extracted 9 subjects, for whom the database contained both pre-operative and post-stenting state: MR volumes, MR flow measurements and invasive pressure catheterization, heart rate and cuff based $\overline{P_{sy}}$ and $\overline{P_{di}}$ measurements. Three of these subjects developed collateral circulation around the coarctation and were excluded from the experiment, leaving 5 patients from COAST and 1 patient from OPBG (Table 3.3).

Using the pipeline introduced in Sections 3.2 and 3.4 the patient-specific geometric arterial tree model and corresponding time-resolved flow profiles were estimated from the MR images. To make sure that segmentation errors do not influence the simulation outcomes, the vessel tree geometry was reviewed by a manual operator in all cases before simulation.

Given the patient-specific anatomy, measured flow rates at the AAo and DAo, the flow transit time, systolic and diastolic cuff pressures and heart rate, we performed a non-invasive parameter estimation of the boundary conditions for each patient. Afterwards the simulation (Sec. 3.4.1) was performed without any further tuning of the parameters. The blood pressure drop estimates across $TAA - DAo$ is reported between the end of segment S_2 and the start of segment S_8, whereas the clinically

more relevant $AAo - DAo$ are measured between the end of segment S_0 and the start of segment S_8 of the axisymmetric arterial tree. The pressure differences are determined at the time-instant when the flow rate through the descending aorta is maximal (peak-to-peak).

[1]See discussion (Sec. 3.6) for details.

Estimation of Pre-operative CoA Pressure Drop

Patient	AAo-DAo			TAA-DAo		
	$\triangle \mathbf{P}^{\mathbf{pre}}_{\mathbf{CFD}}$	$\triangle \mathbf{P}^{\mathbf{pre}}_{\mathbf{ICATH}}$	$\lvert\triangle \mathbf{P}\rvert$	$\triangle \mathbf{P}^{\mathbf{pre}}_{\mathbf{CFD}}$	$\triangle \mathbf{P}^{\mathbf{pre}}_{\mathbf{ICATH}}$	$\lvert\triangle \mathbf{P}\rvert$
#1	53.85	55	1.14	53.35	53	0.35
#3	11.32	8	3.32	12.10	8	4.10
#4	27.36	30	2.63	31.94	28	3.94
#5	15.74	14	1.74	13.04	18	4.95
#6	7.26	39	31.73	7.43	43	35.56
#9	11.07	8	3.07	11.06	N/A	N/A
$\overline{\lvert\triangle \mathbf{P}^{\mathbf{pre}}\rvert}$			[2]2.38 ± 0.82			[2,3]3.33 ± 1.76

Table 3.4.: Comparison of the pressure obtained from invasive catheterization [1] ($\triangle P^{pre}_{ICATH}$) and our proposed non-invasive method ($\triangle P^{pre}_{CFD}$): peak-to-peak blood pressure drops ($mmHg$) between AAo-DAo and transverse aortic arch TAA-DAo in pre-operative CoA.

The results obtained for the non-invasive pressure drop (CFD) in pre-operative CoA are summarized in Table 3.4, together with the invasive pressures obtained from cardiac catheterization ($ICATH$).

Estimation of Post-stenting CoA Pressure Drop

Patient	AAo-DAo			TAA-DAo		
	$\triangle \mathbf{P}^{\mathbf{post}}_{\mathbf{CFD}}$	$\triangle \mathbf{P}^{\mathbf{post}}_{\mathbf{ICATH}}$	$\lvert\triangle \mathbf{P}\rvert$	$\triangle \mathbf{P}^{\mathbf{post}}_{\mathbf{CFD}}$	$\triangle \mathbf{P}^{\mathbf{post}}_{\mathbf{ICATH}}$	$\lvert\triangle \mathbf{P}\rvert$
# 1	7.15	8	0.84	5.38	6	0.61
# 3	-0.92	-2	1.07	-0.14	-9	8.85
# 4	1.23	2	0.76	0.70	-1	1.70
# 5	1.26	0	1.26	1.02	0	1.02
# 6	3.69	4	0.30	0.92	3	2.07
# 9	2.35	0	2.35	1.20	N/A	N/A
$\overline{\lvert\triangle \mathbf{P}^{\mathbf{post}}\rvert}$			1.10 ± 0.63			[3]2.85 ± 3.04

Table 3.5.: Peak-to-peak post-stenting pressure drop in $mmHg$. Comparison of invasive catheterization ($\triangle P^{post}_{ICATH}$) measurement and estimate by our non-invasive method ($\triangle P^{post}_{CFD}$) in post-stenting CoA.

During treatment of the 6 subjects, the stenoses received repair through balloon angioplasty and stent implantation. After the intervention the patients underwent

[2]Excluding case #6 (*see the discussion in Section 3.6 for details*).
[3]Excluding case #9, as $\triangle \mathbf{P}_{\mathbf{ICATH}}$ between **TAA-DAo** was not measured clinically.

follow-up examination — similar to the first exam — to acquire MR images of the thorax and aortic flow, to measure the blood pressure with catheterization, and to perform cuff measurement at the upper extremities. Analogous to the pre-operative case, we have performed the processing pipeline (Sec. 3.4.3) to estimate the post-stenting hemodynamic conditions. The comparison of measured and estimated blood pressure drop results is displayed in Table 3.5. Pre- and post-operative evolution of computed aortic flow is show in Fig. 3.14.

CoA Virtual Stenting Experiment

Patient	AAo-DAo			TAA-DAo		
	$\triangle \mathbf{P}^{\mathbf{vs}}_{\mathbf{CFD}}$	$\triangle \mathbf{P}^{\mathbf{post}}_{\mathbf{ICATH}}$	$\lvert\triangle \mathbf{P}\rvert$	$\triangle \mathbf{P}^{\mathbf{vs}}_{\mathbf{CFD}}$	$\triangle \mathbf{P}^{\mathbf{post}}_{\mathbf{ICATH}}$	$\lvert\triangle \mathbf{P}\rvert$
# 1	-1.10	8	9.10	-0.79	6	6.79
# 3	-0.93	-2	1.06	-0.54	-9	8.45
# 4	7.91	2	3.82	4.51	-1	3.83
# 5	-2.84	0	3.12	-2.03	0	2.25
# 6	0.06	4	4.25	-0.04	3	3.17
# 9	7.98	0	7.85	7.88	N/A	N/A
$\overline{\lvert\triangle \mathbf{P}^{\mathbf{vs}}\rvert}$	$^{2}4.99 \pm 3.00$			$^{2,3}5.33 \pm 2.42$		

Table 3.6.: Virtual stenting analysis: comparison of computed ($\triangle P^{vs}_{CFD}$) and invasively measured post-stenting pressure drop ($\triangle P^{post}_{ICATH}$).

The last clinical use-case is aimed at "predicting" the blood pressure drop of post-stenting conditions prior to the treatment. By applying the introduced methodology (Sec. 3.4.4) to pre-operative data, clinicians would be able to virtually evaluate the outcome of the stenting in terms of aortic blood pressure drop (Tab. 3.6). Figure 3.13a and 3.13b show the blood pressure drop results for all three configurations graphically, while pre- and post-operative evolution of computed aortic flow is shown in Figure 3.14.

3.6. Discussion

This chapter has introduced a non-invasive method to estimate patient-specific aorta morphology and predict personalized blood pressure in the thoracic aorta. In the previously explained experiments (in Section 3.5) we have quantified the performance of our computational pipeline, in this section we will further elaborate on the results.

3.6.1. Lumen Segmentation

Firstly, we studied the static 3D lumen surface extraction accuracy on a wide set of volumes. Note that our 3D lumen segmentation method is capable of processing a

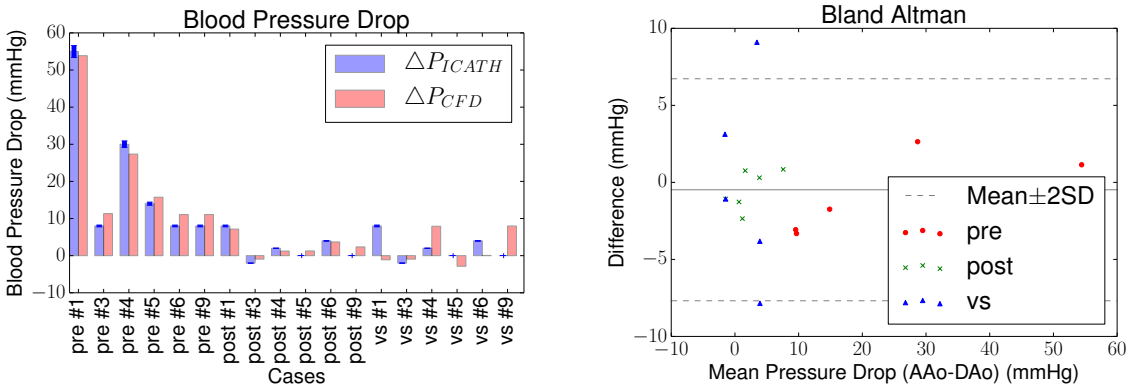

(a) (b)

Figure 3.13.: **a**) Absolute values of pre-, post- and virtual-stenting blood pressure drop estimates. Allowed uncertainty of $\triangle P_{ICATH}$ data also shown [1]. **b**) Bland-Altman plot of pressure drop differences[2].

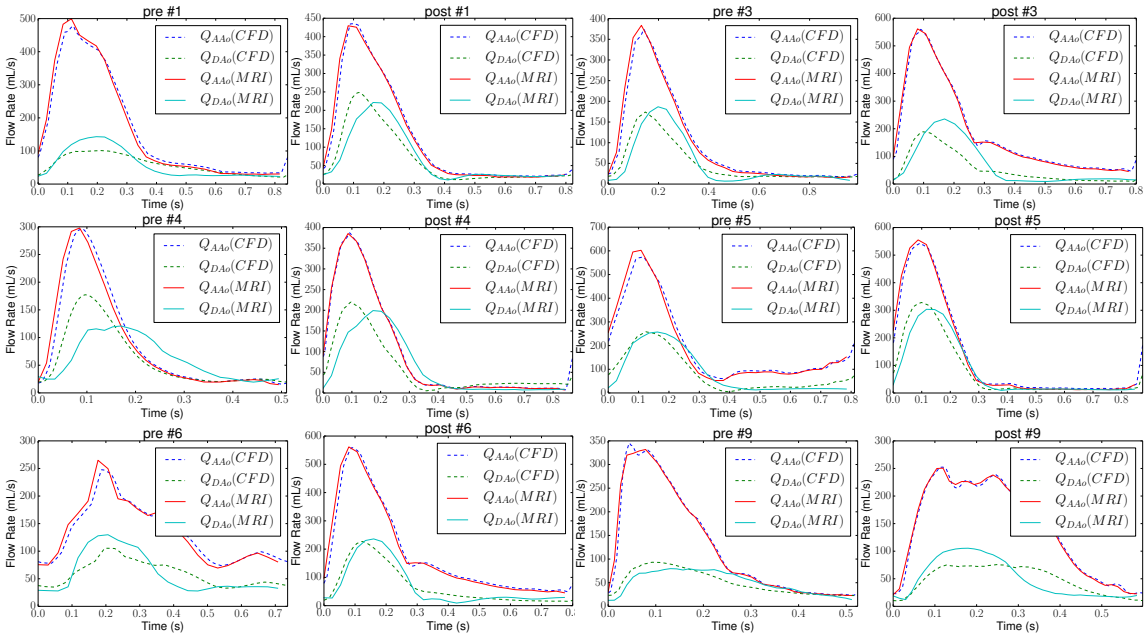

Figure 3.14.: Temporal evolution of measured (dashed lines) and computed (solid lines) pre- and post-stenting flow rates.

wide range of morphological and pathological aorta variations, not only coarctation patients. The accuracy of the fused aortic vessel tree segmentation was evaluated by using the symmetric point-to-mesh distance [215] metric (Table 3.1) in four-fold cross validation setup of the 212 cases, which shows a good agreement of segmentation results. Due to the morphologic variation of the supra-aortic arteries, their lumen segmentation accuracy is below that of the aorta. It was generally observable that the

MR images exhibit some loss of signal towards the borders of the volume (e.g. towards the neck of the patient), which resulted in reduced contrast around the supra-aortic arteries. This is a possible explanation for the difference in accuracy.

As shown in Table 3.2, the clinically relevant measurements on the aortic lumen show good agreement between the model-based and manually measured minimum and maximum aorta diameters. These measurements are crucial in clinical management of aortic diseases for optimal treatment selection and decision making [11].

In the model-based segmentation approach we have presented, neither the morphological model itself nor the estimation method is tied to the MR imaging modality often used in CVD. The approach should be applicable to other imaging modalities too. Automatic feature selection performed in the PBT learning method ensures that the most discriminating cues are retained during training.

3.6.2. Hemodynamic Computations

As can be seen from the results (Tab. 3.4, Fig. 3.13a), the proposed method performs well for most of the pre-operative cases. For patients #1, #3, #4, #5 and #9, our simulation ($\triangle P^{pre}_{CFD}$) reproduces the catheterization blood pressure drop ($\triangle P^{pre}_{ICATH}$) within a narrow margin: mean absolute error of $\overline{|\triangle P^{pre}|} = 2.38 \pm 0.82\ mmHg$. During the review of our results for pre-operative case #6, we observed an incorrect PC-MR acquisition plane (intersecting the aortic valve and left ventricular outflow tract instead of the AAo) that results in an erroneous inflow boundary condition initialization (see lower left panel of Fig. 3.14) and drives the simulation off the course of real aortic inflow. We have included this case in the results for symmetry with the other experiments, and to demonstrate the behavior of the method when fed inconsistent data. Our results are comparable to $ICATH$, especially in the light of the allowed uncertainty involved in $ICATH$ measurements. According to the IEC standard [1], invasive blood pressure catheters are required to be accurate within ± 3 % of the absolute value of blood pressure. Looking at the patient data, we may observe that a variety of both mild ($\triangle P_{ICATH} = 8$) and severe ($\triangle P_{ICATH} = 55$) CoA patients are included and that our method is able to accurately recover the blood pressure drop independent of graveness of this condition (Fig. 3.13b).

The goal of stent implantation is to reduce the difference in blood pressure between the upper and lower body, optimally to completely eliminate the pressure drop. Thus it is reasonable to expect close-to-zero $\triangle P$ values in the post-stenting subjects. However, in some cases residual blood pressure drop persists. Our simulation model for post-stenting (Tab. 3.5) was able to compute very truthful estimates, marked by $\overline{|\triangle P^{post}|} = 1.10 \pm 0.63\ mmHg$. As shown on the lower right panel of Fig. 3.14, the PC-MR inflow for post-stenting patient #9 does not resemble the characteristic ejection curve of the heart. In this case — similar to pre-op patient #6 — the MR inflow plane was acquired too low, it does not measure the ascending blood velocity at the aortic root, but includes the leaflet motion of the valve. Nevertheless, the $\triangle P$ estimates even for #9 are quite accurate, because most of the PC-MR inflow

was still captured correctly. We believe that our stiff stent-wall post-operative model configuration produces results consistent with the effects of stenting.

To predict the intervention outcome in terms of residual blood pressure drop, we proposed "virtual stenting" (Sec. 3.5.3). Here our model was parameterized to "predict" the pressure drop change attributed to the removal of the obstruction lesion. In Fig. 3.14, virtual-stenting flow is not shown, because a high degree of match between pre-operative measured flow and post-stenting simulated flow is not our principal aim for this configuration. Instead, this use-case is better characterized by the AAo-DAo pressure drop comparison. The estimated $\triangle P$ is tabulated in Table 3.6 and shows a reasonable ($4.99 \pm 3.00\ mmHg$) agreement with the invasively measured post-stenting catheter values. It is a well observed process that remodeling of the post-stenting aorta is not limited to the vessel wall reinforced by the stent struts: nearby aortic lumen morphology often changes as well, and collateral arteries might reduce or disappear. Without modeling these changes, the mere replacement of the stenosis segment S_7 of the arterial tree will not perfectly forecast the real post-stenting vessel and pressure drop, as seen on Fig. 3.13b. Accurate morphological measurement of the stenosis and inflow-rate were shown [16] to have the strongest influence on $\triangle P$ in image-based hemodynamic simulations. As our measured data indicates (Table 3.3), aortic flow rates do change after stenting. This creates an additional challenge for the VS analysis, as only pre-operative flow is available for outcome prediction. We believe that this is the second factor behind the largest average error obtained in the VS experiment.

Within these analyses, we have considered all important phases of CoA stenting where currently invasive catheterization is required (severity assessment and post-treatment follow-up) or data is not available (virtual stenting). Our non-invasive results are clinically relevant, especially in comparison with the 20 $mmHg$ clinical cut-off value, and agree with invasive measurements.

Besides accuracy, the aspect of fast computations is highly desirable in the general clinical practice, and our work provides a first effort to reduce the runtime of CoA simulation workflows. Average detection time of the combined lumen model (for all surfaces) is in the range of 8 seconds. The semi-automatic PC-MR flow segmentation and contour tracking takes approximately one minute per case. Our reduced order CFD model is much faster ($8 - 10$ minutes) than conventional unsteady 3D flow computations (all times measured on an Intel Core i7 laptop computer).

Finally, Table 3.7 shows a quantitative review of state-of-the-art investigations of CoA hemodynamics and illustrates the position of our contributions against literature. The table provides an overview of the questions recent research has addressed, such as the type of clinical use-cases, number of subjects examined, included methods and their run-times. We should note that the subjects are different, and therefore a direct comparison of pressure drop results is not feasible across the different works.

[4]normal cases were considered in the same group as post-operative (as we expect near-zero $\triangle P$).
[5]approximated from similar complexity reports[91, 19].
[6]Excluding case #6 (*see the discussion in Section 3.6 for details*).

	number of cases			runtime (hours)			pressure drop error ($mmHg$)		
	PRE	PST	VS	SEG	MES	CFD	PRE	PST	VS
LaDisa et al.[98]	2	[4]3	-	-	-	[5]days	-1.5 ± 4.94	1.66 ± 1.15	-
Valverde et al.[195]	5	[4]2	-	-	-	-	-4.2 ± 4.9	1.0 ± 1.0	-
Ralovich et al.[153]	4	-	-	0.5	0.5	8-10	4.57 ± 5.53	-	-
Itu et al.[84]	4	-	-	-	-	0.13-0.16	1.45 ± 0.76	-	-
Goubergrits et al.[57]	13	-	13	1-4	-	8	-0.5 ± 0.33	-	3.0 ± 2.91
current work	[6]6	6	[6]6	0.5	0.25	0.13-0.16	[6]2.38 ± 0.82	1.10 ± 0.63	[6]4.99 ± 3.00

Table 3.7.: Review of similar computational hemodynamic CoA assessment research. Abbreviations used: pre-operative (PRE), post-operative or normal (PST), virtual stenting (VS), segmentation (SEG), meshing (MES), computational fluid dynamics (CFD).

Closest to our work is the recent study [57] of 13 patients. The authors performed image-based rigid wall 3D simulations of CoA patients. Their investigation included two CoA use-cases, one for pre-treatment estimation of blood pressure drop (very similar to our first experiment), and a second experiment that falls in between our post-stenting and virtual stenting use-cases. In the latter, the authors have reconstructed the post-operative aorta geometry from X-Ray images after the treatment and used the pre-operative PC-MR inflow. As this configuration uses pre-operative inflow and post-intervention geometry, we compare it against our third experiment. Even though their average error of pressure estimation is lower than ours, several aspects limit the benefits of their workflow: first, the simulation time is an order of magnitude larger than ours, second, the blood flow is simulated only at a single time point (systolic state), and third, their high quality vessel measurements require ionizing fluoroscopy.

In general, most hemodynamic simulation studies investigate cases where the whole patient data acquisition is driven by specific computational needs. On the other hand, our methods work on real clinical images that were acquired retrospectively and not specifically for this computation study. As shown, this comes with its own challenges, for example the sensitivity of positioning the PC-MR plane or sub-optimal image quality. However, a solid advantage is that further validation of our methods would be possible using existing (previously acquired) data.

3.7. Extensions

3.7.1. Patient-specific 3D CFD Simulations

In their article titled "Cardiology Is Flow" Richter et al. [161] argue that restoration of blood flow and understanding of flow patterns should be the primary form to elucidate CVD lesions. Our work towards blood pressure drop assessment was conceived in this fashion. The blood pressure assessment method devised in Section 3.4 uses a reduced order quasi 1D model of hemodynamics and fluid-structure interaction. This computational model only provides spatial information about flow along the centerlines of the vessel tree.

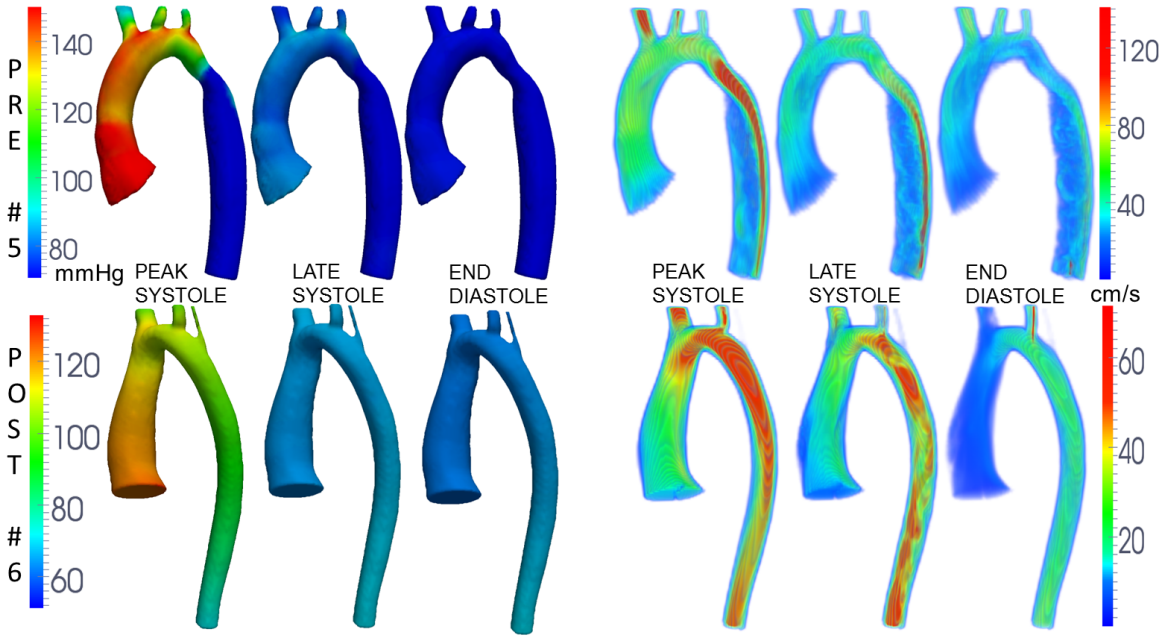

Figure 3.15.: **Left**: Blood pressure distribution mapped on lumen boundary, **Right**: Volume rendered velocity magnitude (for cases pre-operative #5, post-operative #6). Note the different scales.

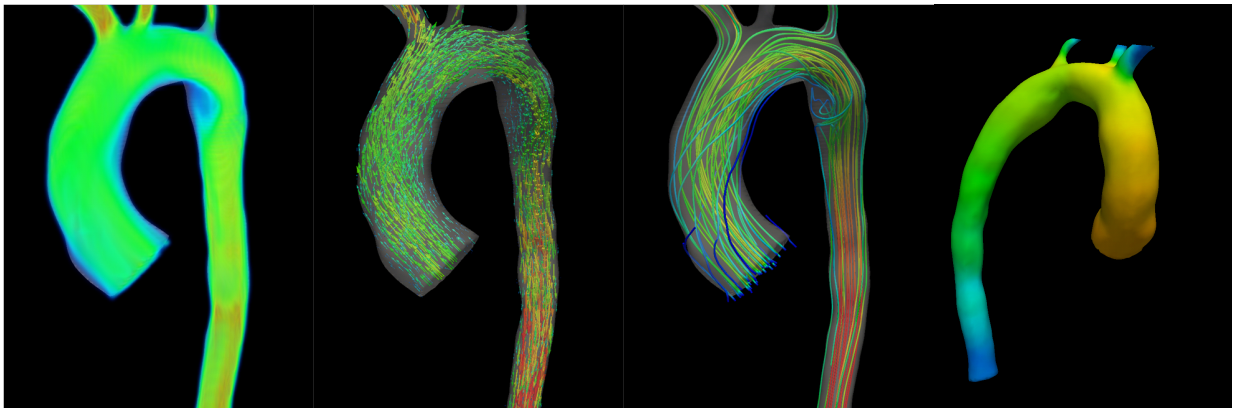

(a)

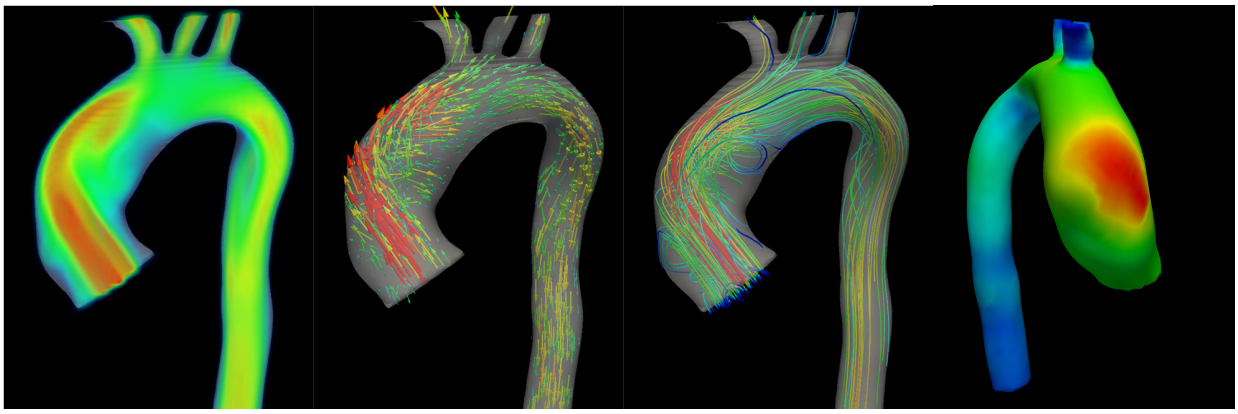

(b)

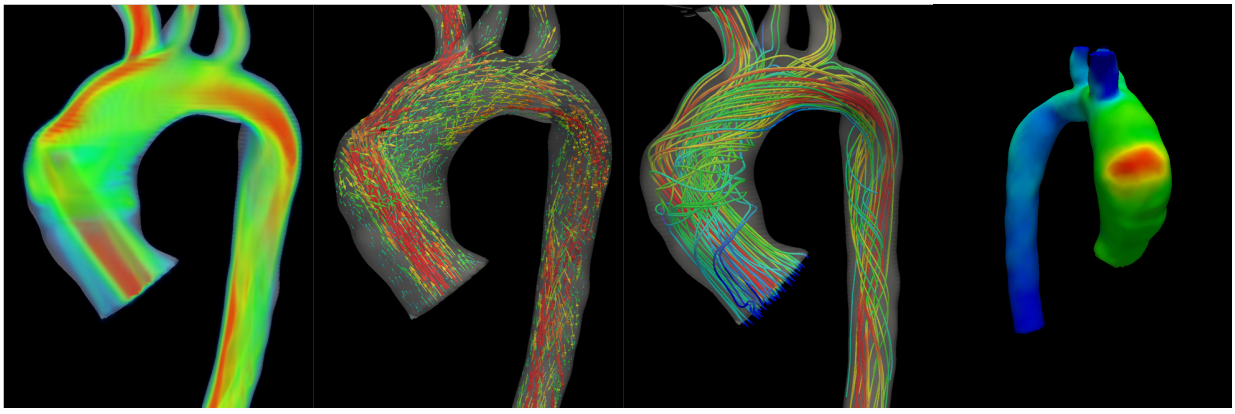

(c)

Figure 3.16.: Computed blood flow conditions in BAV patients (first, second and third columns show velocity and fourth column shows pressure). **(a)** normal control. **(b)** and **(c)** show BAV with mild and severe (respectively) aortic dilation as comorbidities.

However, certain blood flow patterns, hemodynamic indices and biomechanical interaction with the vessel walls may only be observed in 3D computations. Therefore initial, qualitative investigation of 3D flow patterns in CoA and BAV patients were carried out.

To obtain comprehensive flow information in three dimensions we solve the full 3D Navier-Stokes equations in the luminal aortic domain calculated, using the personalized outflow boundary conditions for pressure. We use an embedded boundary method for automatic transfer of the segmented triangular lumen mesh into a Cartesian domain. The embedding function is a signed-distance function computed using the Closest Point Transform [124]. The computational domain cells are tagged based on their relation with the inlet triangular mesh as follows: *Exterior* (no computation is taking place), *Interior* (computation is taking place), *Inlet*, *Outlet* and *Wall* (appropriate boundary conditions are imposed). The *Inlet* and *Wall* cells are all interior to the domain, while the *Outlet* cells are situated on the domain boundaries, by extending the lumen of each vessel in its centerline direction until it reaches the Cartesian boundary, based on [130]. Our embedded boundary Navier-Stokes solver uses a fractional step method [10] that computes in a first step an intermediate velocity field, using the nonlinear advection-diffusion equation for velocity, and then projects the intermediate velocity onto the field of divergence free and tangent to the vessel boundary vector fields. For the velocity advection we use second-order upwind, Van-Leer slope limiting methods, while for the diffusion force components we use a semi-implicit approach as in [104] which is first order accurate and unconditionally stable in 3D. We solve the pressure projection Poisson equation using an efficient implicit multi-grid preconditioned conjugate gradient solver. The boundary conditions for the velocity are Dirichlet in the *Inlet* cells, no-slip (Dirichlet) in the *Wall* cells, and Neumann in the *Outlet* cells [130].

For CoA computations, we use a variable-in-time flat inlet velocity profile, and outlet pressure boundary conditions provided by the corresponding axisymmetric 1D simulations (Section 3.4). For BAV computations we use a variable-in-time spatially constrained inlet velocity profile from PC-MRI to capture the asymmetric blood flow trough the aortic valve. The blood density and viscosity are set to literature based values for healthy individuals ($1.05 g/cm^3$ and $4 mPa \cdot s$).

The results from the 3D simulations for two patients are presented in Figure 3.15. There is a significant pressure gradient observable across the coarctation at peak systole, which gradually disappears towards the end of diastole. A volumetric visualization of the velocity magnitude at peak systole, late systole and end diastole are shown in the three figures at the right. The high velocity jet in the stenosis region is clearly visible as expected. Similar methodology can also be applied to the post-operative data, by taking into consideration the modified wall-stiffness introduced from the stent implantation. Preliminary results are shown in the bottom row of Figure 3.15. Here, the pressure gradients between AAo-DAo and TAA-DAo have been partially restored to normal values. A similar effect can also be noticed in the flow patterns: highest velocity in the aortic arch, and reduced Reynolds number.

Ascending aortic dilation is a widening of the ascending aorta and involves high risk of aortic rupture and dissection if untreated. It was shown, that the incidence of ascending aortic dilation is higher in bicuspid aortic valve (BAV) patients [188] in comparison to normal controls. In BAV two leaflets of the aortic valve are fused while in normal cases all three leaflets move and regulate blood flow independently. Due to its shape, BAV distorts the blood flow through the aortic valve. We have carried out 3D flow simulation as described above, Figure 3.16 shows detailed spatial distribution of velocity and pressure. In the BAV cases formation of a high speed jet is recognizable that is not present for normal aortic valve. The momentum transmitted by the jet onto the dilated aortic wall may correlate with the progression of dilation.

3.7.2. Integrated Clinical Prototype

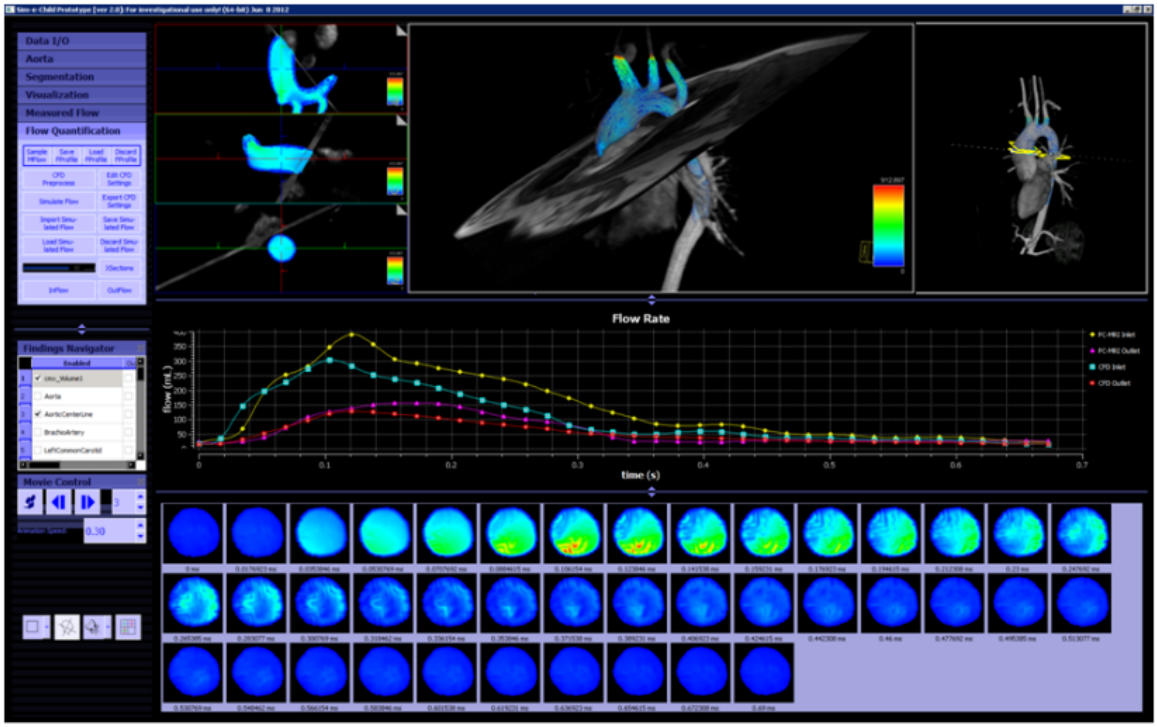

Figure 3.17.: Screen capture of integrated software prototype.

During the development of the image-based hemodynamic assessment workflow described in this chapter, a computer software prototype was also realized. All computational steps of complete CoA hemodynamic workflow (Figure 3.11) was realized in a single integrated clinical application prototype as shown in Figure 3.17. The software prototype allows browsing and selecting relevant MR images from DICOM, performing the complete model-based segmentation process (Section 3.2), allows morphology measurement, therapy planning, segmentation of PC-MRI slice, hemodynamic computations, interactive volumetric visualization and analysis of flow fields similar to

ideas outlined by Taylor et al. [190] in their seminal work about image-based predictive medicine.

CHAPTER 4

Peri-operative Image Fusion

Percutaneous structural heart disease (SHD) interventions start to gain wider acceptance in therapy as we have seen in Section 2.1.2. Image guidance is a key facilitator of minimally invasive cardiac interventions: the technical challenges posed by these operations are addressed by hybrid operating rooms (OR), where image guided navigation is becoming crucial part of therapeutic practice.

The current gold standard for image based interventional guidance is C-arm X-Ray Fluoroscopy (XRF, Section 2.2.3). 2D real-time fluoroscopic images are acquired using ionizing radiation requiring the interventional team to repeatedly absorb elevated doses. X-Ray visualizes metallic instruments (guide wires, catheters, stents) with excellent contrast, but soft tissue (the heart is composed entirely of muscles – soft tissue) and calcification is shown poorly if at all. Administration of contrast agents enables to display cavities (chambers, vessels) and delineate respective boundaries, but poses additional risk to the patient. Furthermore the presented projected view doesn't provide intuitive depth perception.

Intracardiac echocardiography (ICE) is an emerging, real-time, non-ionizing peri-operative modality with the promise of removing sedation or general anesthesia (GA) associated with Transesophageal Echocardiography (TEE) at comparable image quality (Sec. 2.2.2). High-risk cardiac patients tend to have a lower tolerance towards GA and intubation, thus avoiding these factors enables earlier hospital discharge. Recent technological advances enable real-time acquisition of 3D imaging data through ICE ultrasound catheters. This opens up the possibility to support interventionalists with additional live 3D images during the intervention, with excellent soft tissue contrast.

The desirable co-registration and fusion of intra-operative echocardiography and C-arm X-Ray fluoroscopy (XRF) aims to combine the complementary benefits of the two imaging systems for use in hybrid operating rooms. For this reason, the goal of this chapter is to propose an imaging system that could support the current and

emerging transcatheter SHD interventions in a hybrid OR setting with a focus on avoiding general anesthesia. The method is built around model-based 2D-3D registration (Sec. 4.1). We model an ICE catheter equipped with radiopaque ball marker fiducials (Sec. 4.2). The model is fitted to single-shot fluoroscopy images including the catheter (Sec. 4.3). The extracted fiducial projections are used as feature points to investigate 3D pose recovery (Sec. 4.4) and establish the registration transformation between XRF and ICE. Quantitative experimental results on synthetic digitally reconstructed radiographs (DRR) and *in-vivo* porcine images are demonstrated in Section 4.5. Finally, the feasibility of the image fusion system and clinical usefulness is discussed in Section 4.6.

4.1. Registration for Peri-operative Image Fusion

4.1.1. Interventional Image Fusion

Transcatheter procedures rely on interventional imaging for guidance. The effectiveness of fusing information from multiple live imaging modalities during cardiac procedures is well known and documented [196, 99, 52, 133].

In classical interventional cardiology the primary navigation aid is X-Ray, where catheters introduced into the vessels are well visible. However X-Ray shows no soft tissue, uses ionizing radiation and blood visualization requires use of radio-opaque contrast agents. With a long background in diagnostic cardiology, echocardiography is gaining a foothold in therapy due to ease of use, real-time imaging and excellent soft tissue contrast, but only has a limited spatial field of view. The complementary nature of these two modalities makes their concurrent application (fusion) a helpful guidance tool. Current drawback of TEE guidance is the need for general anesthesia and patient discomfort. Catheter based intracardiac echocardiography (ICE) has the promise of removing general anesthesia during SHD interventions [175, 147] and has already proved valuable during electrophysiology procedures (EP) [206]. However existing X-Ray—ICE image-fusion solutions rely on additional electromagnetic tracking (EMT) equipment for registration that might not be desirable in the already crowded operating theater. A purely image-based alternative method would be of interest.

Catheter detection in XRF is a well researched issue, automatic methods exists to extract various instruments [112, 113] at interactive rates. Wang et al. [204] describes a system for tracking an IVUS catheter in cine X-Ray to perform image registration. In other ultrasound-angiography registration scenarios the 3D pose of the transducer is required, too: the CartoSound [206, 186] system employs electromagnetic tracking built into the C-arm to localize the ICE catheter. Robotic self-tracking [114] has also been investigated for echo guidance. Often such external hardware setups are not feasible, and recently research interest was directed towards introducing purely image registration based systems for fusion of X-Ray with TEE [99, 52, 133] and ICE [155].

4.1.2. Image Registration

In this section we will review the mathematical formalism of medical image registration that serve the basis of fusion. Image registration estimates a transformation between two images. Assuming the fixed $\mathcal{F} : \Omega_{\mathcal{F}} \to \mathbb{R}$ and the moving $\mathcal{M} : \Omega_{\mathcal{M}} \to \mathbb{R}$ images and a set of transformations $\phi : \Omega_{\mathcal{M}} \to \Omega_{\mathcal{F}}$ image registration seeks to compute optimal parameters of a transformation ϕ^*

$$\phi^* = \arg\min_{\phi} \mathcal{E} \tag{4.1}$$

in a manner to minimize an "error" or "energy" $\mathcal{E}$ such that the underlying anatomy is correctly aligned. $\mathcal{E}$ quantifies the quality of fit, measured through a data term $\mathcal{D}$ depending on the alignment of corresponding information obtained by the transformation parameters.

In Eq. (4.1) $\mathcal{E}$ appears as the argument of minimization based on noisy measurements, resulting in an optimization problem.

Registration Data Term

As we have seen above, correspondence is a key factor in registration. How corresponding information is represented influences the data term. In the standard dichotomy introduced by the survey of Maintz and Viergever [116] two registration basis are mentioned: *extrinsic*, feature-based and *intrinsic*, voxel intensity-based. These approaches differ in their way of defining the data term.

Similarity Measures in Intensity-based Registration

Voxel intensity based registration approaches assume dense, pixel-wise correspondences across the fixed reference and moving template images to define a similarity measure directly on the gray values. Thus the similarity measure $\mathcal{D}_{SM}$ describes the quality of fit in the data term in the objective function of equation (4.1):

$$\phi^* = \arg\min_{\phi} \mathcal{D}_{SM}\left(\mathcal{F}, \phi\left(\mathcal{M}\right)\right) \qquad \mathcal{D}_{SM} : \Omega_{\mathcal{F}} \times \Omega_{\mathcal{M}} \to \mathbb{R} \tag{4.2}$$

where $\phi\left(\mathcal{M}\right)$ denotes interpolated value of a voxel at the transformed location ϕ in the moving image. A good similarity measure takes its minimum at the transformation ϕ where the alignment is best between the fixed and moving images. Most intensity-based registration algorithms rely on iterative optimization to solve equation (4.2). Some of the most distinguished similarity measures are: sum of squares of intensity differences (SSD), correlation coefficient (CC) and normalized mutual information (MI) based [71, 179].

Using the SSD similarity measure, the intensity differences are described at different ϕ transforms:

$$\mathcal{D}_{SM}^{SSD} = \frac{1}{N}\sum_{\mathbf{y}=\mathbf{1}}^{N}\left(\mathcal{F}(\mathbf{y}) - \mathcal{M}(\phi(\mathbf{y}))\right)^2 \qquad \forall \mathbf{y} \in \mathcal{F} \cap \phi(\mathcal{M}). \tag{4.3}$$

In order to make the area of overlap not influence the resulting measure, SSD is normalized over all voxels in the overlap region ($\mathcal{F} \cap \phi(\mathcal{M})$). It was shown that SSD is the optimal measure if the images only differ through Gaussian noise [71]. SSD is very sensitive to large voxel intensity differences between the fixed and moving images, due to this SSD is suitable only in a limited set of problems (e.g. consecutive slices of an MR volume).

In most registration tasks the above assumption of Gaussian differences does not hold. However if two images conform to a linear intensity relationship between them, an other similarity measure, the normalized cross correlation was shown to be the ideal measure [179].

$$\mathcal{D}_{SM}^{CC} = \frac{\sum_{\mathbf{y}}(\mathcal{F}(\mathbf{y}) - \bar{\mathcal{F}})(\phi(\mathcal{M}(\mathbf{y})) - \bar{\mathcal{M}})}{\sqrt{\sum_{\mathbf{y}}(\mathcal{F}(\mathbf{y}) - \bar{\mathcal{F}})\sum_{\mathbf{y}}(\phi(\mathcal{M}(\mathbf{y})) - \bar{\mathcal{M}})}} \qquad \forall \mathbf{y} \in \mathcal{F} \cap \phi(\mathcal{M}). \tag{4.4}$$

where $\bar{\mathcal{F}}$ and $\bar{\mathcal{M}}$ are the mean of voxel values in images $\mathcal{F}$ and transformed $\mathcal{M}$ in the overlap domain.

Especially in intra-modal registration both the Gaussian model of noise and linear intensity relations are too restrictive and different similarity measures were developed. An information theoretic approach to registration tries to minimize the shared amount of information between two images. This is expressed by the normalized mutual information:

$$\mathcal{D}_{SM}^{MI} = \frac{H(\mathcal{F}) + H(\phi(\mathcal{M}))}{H(\mathcal{F}, \phi(\mathcal{M}))} \tag{4.5}$$

where H is denoting the marginal and joint entropy of the two images. Mutual information was successfully applied to e.g. cranial MR-CT volume registration [179]. For further details on mutual information and entropy based similarity measures we recommend the book of *Medical Image Registration* [71].

Distance Measures in Feature-based Registration

In feature-based image registration geometric structures or segmented salient landmark points are identified in both images. Afterwards registration becomes the problem of finding i) a transformation to align and ii) a correspondence to match these feature points. In feature-based registration the data term is described with a distance measure $\mathcal{D}_{DM}$ defined over the discrete feature points. Following equation (4.1):

$$\phi^*, \mathcal{C}^* = \arg\min_{\phi,\mathcal{C}} \mathcal{D}_{DM}\left(\{\mathbf{f}_i\}, \{\mathbf{m}_i\}\right) \tag{4.6}$$

$$\mathcal{D}_{DM}\left(\{\mathbf{f}_i\},\{\mathbf{m}_i\}\right)=\sum_i d\left(\mathbf{f}_i,\phi(\mathcal{C}(\mathbf{f}_i,\{\mathbf{m}_j\}))\right)^2 \tag{4.7}$$

where $\mathbf{f}_i$ denote the features from $\mathcal{F}$ and $\mathbf{m}_i$ the features from $\mathcal{M}$, while $\mathcal{C}$ is the assignment of pair-wise correspondence. For data-points outside of the discrete features, the computed transform ϕ is extrapolated.

Euclidean Distance If the features are point-like, often the l^2 norm or Euclidean distance is used as $d(\cdot,\cdot)$ in Eq. (4.7). The l^2 norm of two n-dimensional points $\mathbf{p}$ and $\mathbf{q}$ is equal to the length of the straight segment connecting them[1][2]:

$$d(\mathbf{p},\mathbf{q})=\sqrt{\mathbf{p}^T\mathbf{q}}=\sqrt{(q_1-p_1)^2+(q_2-p_2)^2+\cdots+(q_n-p_n)^2}=\sqrt{\sum_{i=1}^{n}(q_i-p_i)^2}. \tag{4.8}$$

Hausdorff Distance Sometimes it is desirable to compare "maximum distance of a set to the nearest point in the other set" [164], especially when describing localization results. Given two sets of points $A=\{\mathbf{a}_1,\mathbf{a}_2,\ldots,\mathbf{a}_n\}$ and $B=\{\mathbf{b}_1,\mathbf{b}_2,\ldots,\mathbf{b}_n\}$ (say detection results and ground truth position), the one-sided Hausdorff distance from A to B is:

$$d_{H1}(A,B)=\max_{\mathbf{a}\in A}\min_{\mathbf{b}\in B}\|a-b\| \tag{4.9}$$

while the symmetric Hausdorff distance is defined as:

$$d_H(A,B)=\max(d_{H1}(A,B),d_{H1}(B,A)). \tag{4.10}$$

Transformations

Image registration problems may involve various geometrical transformations. Typical medical applications are covered by the following dimensionality of transformations: $2D-2D$, $2D-3D$ and $3D-3D$. A transformation $\phi:\Omega_{\mathcal{M}}\rightarrow\Omega_{\mathcal{F}}$ maps a point $\mathbf{x}$ in the domain of the moving image $\Omega_{\mathcal{M}}$ to an other point $\mathbf{x}'$ in the space of the fixed image $\Omega_{\mathcal{F}}$. Depending on the medical task, the most common class of transformations are: rigid, similarity, affine, projection, curved.

Many applications in medical image registration involve objects with rigid behavior. Examples are bones or objects attached to bony structures. Rigid transformations preserve all distances and are limited to translation and rotation. Rigid transformations may be illustrated in the form

$$\mathbf{x}'=T_{Rigid}(\mathbf{x})=\mathtt{R}\mathbf{x}+\mathbf{t} \tag{4.11}$$

[1] Alternatively the l^2 norm is denoted $d(\mathbf{p},\mathbf{q})=\|\mathbf{p}-\mathbf{q}\|$.
[2] Note that the l^2 norm is symmetric $d(\mathbf{p},\mathbf{q})=d(\mathbf{q},\mathbf{p})$.

where $\mathtt{R} \in SO(3)$ is a 3×3 orthogonal matrix and $\mathbf{t} \in \mathbb{R}^3$. Additionally to avoid reflections $det(\mathtt{R}) = 1$. A rigid transformation has six degrees of freedom, defined as translation along the three Cartesian coordinate axes $\mathbf{t} = (t_x, t_y, t_z)$ and three for rotation around the same axes (α, β, γ).

If uniform scaling is allowed in addition to a rigid transformation, we are arrive at similarity transformations:

$$\mathbf{x}' = T_{Similarity}(\mathbf{x}) = s\mathtt{R}\mathbf{x} + \mathbf{t} \tag{4.12}$$

where the scalar s is the isotropic scaling factor. A similarity transform may be described with 7 parameters.

Nonrigid transformations may occur in inter-patient registration of rigid objects or due to nonrigid anatomy. Anisotropic scaling and shearing in addition to a rigid transform define an affine mapping[3]:

$$\mathbf{x}' = \begin{bmatrix} x' \\ y' \\ z' \\ 1 \end{bmatrix} = T_{Affine}\mathbf{x} = \begin{bmatrix} \mathtt{A} & \mathbf{t} \\ \mathbf{0}^T & 1 \end{bmatrix} \mathbf{x} = \begin{bmatrix} a_{11} & a_{12} & a_{13} & t_x \\ a_{21} & a_{22} & a_{23} & t_y \\ a_{31} & a_{32} & a_{33} & t_z \\ 0 & 0 & 0 & 1 \end{bmatrix} \begin{bmatrix} x \\ y \\ z \\ 1 \end{bmatrix} \tag{4.13}$$

without restrictions on the elements of $\mathtt{A} \in \mathbb{R}^{3\times3}$. Affine transforms preserve parallelism and are useful to represent cases where an image may be skewed. Affine transformation require 12 parameters: a_{ij} $i = 1, 2, 3$ $j = 1, 2, 3$ and $\mathbf{t} = (t_x, t_y, t_z)$.

The most general linear transforms are projective transformation. Projective transformation are ubiquitous in 2D-3D registration problems (for example perspective projection in X-Ray images). Projective transformations preserve straightness of lines and planarity of surfaces [179]. General projective transformations may have up to 16 degrees of freedom and might require a 4×4 matrix):

$$\mathbf{x}' = \begin{bmatrix} x' \\ y' \\ z' \\ w' \end{bmatrix} = T_{Projection}\mathbf{x} = \begin{bmatrix} \mathtt{A} & \mathbf{t} \\ \mathbf{p}^T & \alpha \end{bmatrix} \begin{bmatrix} x \\ y \\ z \\ 1 \end{bmatrix} \tag{4.14}$$

Due to their importance in this work, we will look at projective transformations in more detail in Section 4.1.3.

Deformable or non-linear, curved mappings [71] are also possible (e.g. in deformable inter-patient organ registration), but fall outside of our investigation.

4.1.3. 2D-3D Registration

Perspective projections relate three dimensional objects to their planar projection images. In rigid 2D-3D registration Eq. (4.1) is solved where the data term describes

[3]Following the notation introduced in *Multiple View Geometry in Computer Vision* [64], both $\mathbf{x}$ and $\mathbf{x}'$ denote points in homogeneous coordinates when affine or projective transformations are discussed.

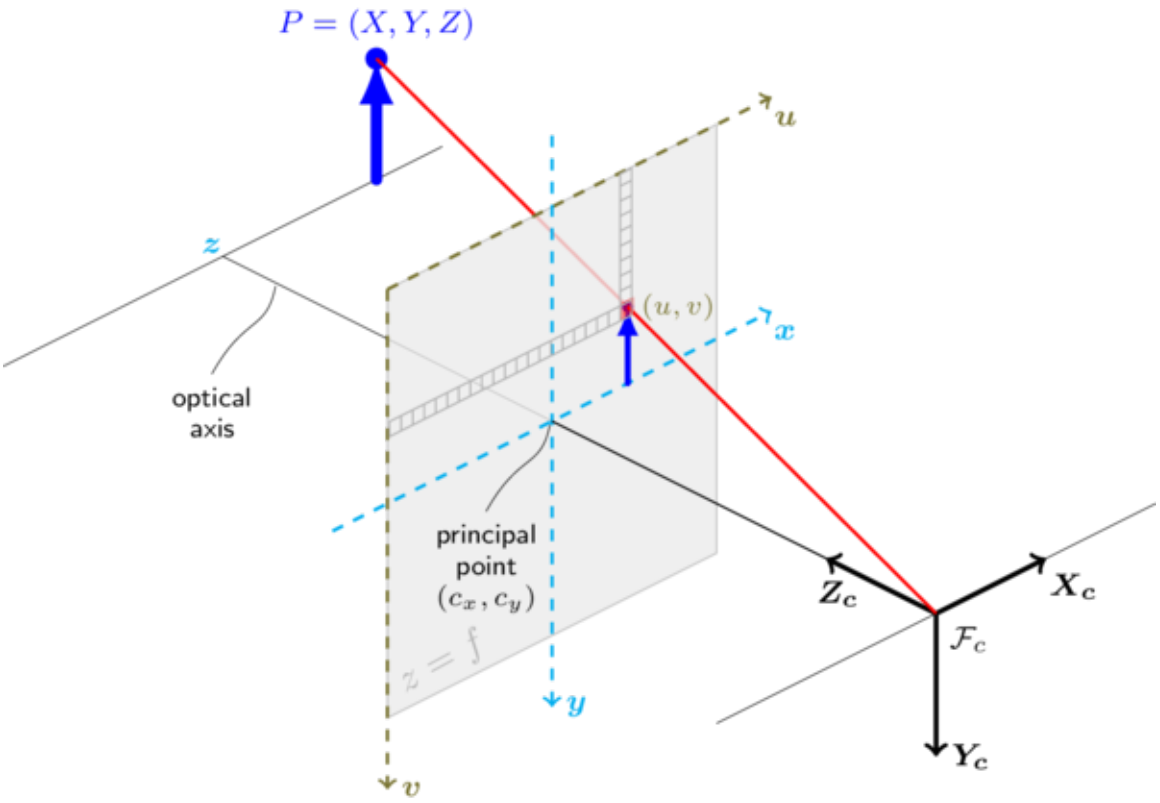

Figure 4.1.: The pinhole camera model assumes no skew and square pixels. Reproduced from [35].

a perspective projection P. Perspective projections are conveniently represented by a 3×4 matrix:

$$\phi = \mathtt{P} = \mathtt{K}\,[\mathtt{R}|\mathbf{t}] \tag{4.15}$$

where the right-hand side of Eq. (4.15) is composed of the intrinsic and extrinsic camera parameters. Here the intrinsic camera parameters are captured within the K calibration matrix:

$$\mathtt{K} = \begin{bmatrix} \alpha_x & s & c_x \\ 0 & \alpha_y & c_y \\ 0 & 0 & 1 \end{bmatrix} \tag{4.16}$$

where α_x and α_y are the scale factors in the x and y directions, s is the skew parameter and (c_x, c_y) are the coordinates of the principal point. The principal point is where the camera optical axis intersects the imaging plane.

In the pinhole camera model (Fig. 4.1) no skewness is assumed ($s = 0$) and pixels are presumed to be square ($\alpha_x = \alpha_y = focal\ length$)

$$\mathtt{K}_{pinhole} = \begin{bmatrix} f & 0 & c_x \\ 0 & f & c_y \\ 0 & 0 & 1 \end{bmatrix} \tag{4.17}$$

with f being the focal length of the camera. The extrinsic camera parameters $[\mathtt{R}|\mathbf{t}]$ describe a rigid transformation from world coordinate system to camera coordinate system.

The estimation of $\mathtt{P}$ within Eqs. (4.2) or (4.6) constitutes the rigid 2D-3D registration problem. For the interested reader Markelj et al. [120] provides a comprehensive survey of $2D$-$3D$ registration methods for image-guided interventions.

4.1.4. Feature-based 2D-3D Registration

Substituting Eq. (4.15) into Eq. (4.6) yields the general formulation of feature-based $2D$-$3D$ registration:

$$\phi^*, \mathcal{C}^* = \arg\min_{\phi,\mathcal{C}} \sum_i^n d\left(\mathbf{f}_i, \phi\left(\mathcal{C}\left(\mathbf{f}_i, \{\mathbf{m}_j\}\right)\right)\right)^2. \tag{4.18}$$

Due to its combinatorial nature[4], the correspondence estimation is often solved outside of the transformation estimation. Additionally, if in Equation 4.18 the camera calibration $\mathtt{K}$ is known, we are left to estimate the extrinsic camera parameters $[\mathtt{R}|\mathbf{t}]$ (next Section).

4.1.5. 2D-3D Pose Estimation, the PnP Problem

The estimation of the extrinsic camera parameters $[\mathtt{R}^*|\mathbf{t}^*]$

$$\mathtt{R}^*, \mathbf{t}^* = \arg\min_{\mathtt{R},\mathbf{t}} \sum_i^n d\left(\mathbf{x}'_i, \mathtt{K}\left[\mathtt{R}|\mathbf{t}\right]\mathbf{x}_i\right)^2 \tag{4.19}$$

means trying to determine the pose (orientation and position) of a calibrated camera from 2D-3D point correspondences. The 2D-3D pose estimation is known as Perspective-n-Point (PnP) problem in computer vision and (space) resection in photogrammetry. The PnP problem received much attention in the vision community, already at least since 1971 when the direct linear transform (DLT) method was formally published [3]. Since then various iterative (using weak perspective approximation [33], orthogonal iteration [111], semi-definite programs [170] or classical non-linear least squares [64, 109]) and direct, closed-form (employing virtual control points [102] and polynomial systems [70, 218, 96, 135]) solutions were proposed showing the practical importance and fundamental difficulty of the problem.

Even though closed form solutions exists, iterative methods [33, 54, 73] tend to achieve more robust matches with noisy 2D marker projections. These methods operate under the assumption, that 2D-3D point correspondences are known *a priori*, while [29] solves the simultaneous pose and correspondence estimation problem.

[4]It may be very difficult to compute the gradient in combinatorial problems.

To solve the PnP problem at least three points are required. If at least $n \geq 4$ point correspondences are available PnP becomes a non-linear problem with the number of solutions dependent on n and the point constellation. Each point correspondence gives two equations to the system of residuals defined in Eq. (4.19) due to scaling ambiguity in the projection.

In the next sections we provide a brief overview of three different approaches to solve the PnP problem.

DLT

The direct linear transformation (DLT) method estimates the intrinsic and extrinsic matrices jointly [3]. We are following Hartley et al. [64] to introduce the overview of DLT. In the right hand side of Eq. (4.19) we calculate the distance of the measured and projected point correspondences. Assuming no measurement noise and perfect perspective projection matrix $\mathtt{P}$ the following holds[5]:

$$\mathbf{x}'_i = \mathtt{P}\mathbf{x}_i : \forall i \in \{1, 2, \ldots, n\} \tag{4.20}$$

where $\mathbf{x}'_i =\in \mathbb{P}^2$, $\mathbf{x}_i =\in \mathbb{P}^3$. In Eq. (4.20) both sides $\mathbf{x}'_i$ and $\mathtt{P}\mathbf{x}_i$ are homogeneous vectors, defined up to a magnitude scale factor. Based on the observation that the vectors are pointing in the same direction but are not necessary equal, we may write

$$\mathbf{x}'_i \times \mathtt{P}\mathbf{x}_i = \mathbf{0}. \tag{4.21}$$

Moreover using the notation of $\mathbf{p}^{iT} \in \mathbb{R}^{1\times 4}$ being the rows of $\mathtt{P}$:

$$\mathtt{P}\mathbf{x}_i = \begin{pmatrix} \mathbf{p}^{1T}\mathbf{x}_i \\ \mathbf{p}^{2T}\mathbf{x}_i \\ \mathbf{p}^{3T}\mathbf{x}_i \end{pmatrix}, \quad s.t. \quad \mathtt{P} = \begin{bmatrix} \mathbf{p}^{1T} \\ \mathbf{p}^{2T} \\ \mathbf{p}^{3T} \end{bmatrix} \tag{4.22}$$

and writing the matrix form of the cross product in Eq. (4.21) yields

$$\begin{bmatrix} \mathbf{0}^T & -w'_i\mathbf{x}_i^T & y'_i\mathbf{x}_i^T \\ w'_i\mathbf{x}_i^T & \mathbf{0}^T & -x'_i\mathbf{x}_i^T \\ -y'_i\mathbf{x}_i^T & x'_i\mathbf{x}_i^T & \mathbf{0}^T \end{bmatrix} \begin{pmatrix} \mathbf{p}^1 \\ \mathbf{p}^2 \\ \mathbf{p}^3 \end{pmatrix} = \mathbf{0}. \tag{4.23}$$

Here the column vector $\mathbf{p}$ contains the elements of the desired projection matrix $\mathtt{P}$:

$$\mathbf{p} = \begin{pmatrix} \mathbf{p}^1 \\ \mathbf{p}^2 \\ \mathbf{p}^3 \end{pmatrix}, \ \mathbf{p} \in \mathbb{R}^{12\times 1}. \tag{4.24}$$

We may not need the third equation of Eq. (4.23), as only the first two equations are linearly independent, yielding

$$\begin{bmatrix} 0 & 0 & 0 & 0 & -w'_ix_i & -w'_iy_i & -w'_iz_i & -w'_iw_i & y'_ix_i & y'_iy_i & y'_iz_i & y'_iw_i \\ w'_ix_i & w'_iy_i & w'_iz_i & w'_iw_i & 0 & 0 & 0 & 0 & -x'_ix_i & -x'_iy_i & -x'_iz_i & -x'_iw_i \end{bmatrix} \mathbf{p} = \mathtt{A}_i\mathbf{p} = 0. \tag{4.25}$$

[5] $\mathbb{P}^d$ denoting the d dimensional projective space as in Hartley et al. [64].

where $\mathtt{A}_i \in \mathbb{R}^{2\times 12}$. Stacking $\mathtt{A}_i$ for all n point correspondences we obtain $\mathtt{Ap} = 0$, $\mathtt{A} \in \mathbb{R}^{2n\times 12}$. With $n \geq 6$ point correspondences, the equation system is over-determined ($\mathtt{P}$ has 12 entries and 11 degrees of freedom, ignoring scale) [64]. Due to noisy measurements of $\mathbf{x}'_i$ and $\mathbf{x}_i$, generally, there is no exact solution to $\mathtt{Ap} = 0$ besides the null solution. To avoid this, $||\mathtt{Ap}||$ is minimized with the constraint of $||\mathbf{p}|| = 1$. The solution to this linear least-squares problem is the last column of $\mathtt{V}$, where the singular value decomposition of $\mathtt{A}$ is $\mathtt{A} = \mathtt{UDV}^T$. The DLT method minimizes algebraic error with the residual $\mathtt{Ap}$, however this quantity is not geometrically meaningful. The derivation of the solution is further explained in A5.3 of [64].

POSIT

The "Pose from Orthography and Scaling with ITerations" (POSIT) algorithm [33] is an iterative estimation of the perspective projection under the weak-perspective assumption. A weak perspective approximates a full perspective with uniform scaling and an orthographic projection. Given a known camera calibration matrix $\mathtt{K}$, for each point correspondence $i = 1, 2, ..., n$ we may write:

$$\begin{pmatrix} w'_i u_i \\ w'_i v_i \\ w'_i \end{pmatrix} = \begin{pmatrix} x'_i \\ y'_i \\ w'_i \end{pmatrix} = \mathbf{x}'_i = \mathtt{P}\mathbf{x}_i = \begin{bmatrix} f & 0 & c_x \\ 0 & f & c_y \\ 0 & 0 & 1 \end{bmatrix} \begin{pmatrix} \mathbf{R}^{1T} & T_x \\ \mathbf{R}^{2T} & T_y \\ \mathbf{R}^{3T} & T_z \end{pmatrix} \mathbf{x}_i. \tag{4.26}$$

Further, assuming central projection, the principal point is at $(c_x, c_y)^T = (0, 0)^T$ (Fig. 4.1):

$$\begin{pmatrix} w'_i u_i \\ w'_i v_i \\ w'_i \end{pmatrix} = \begin{pmatrix} f\mathbf{R}^{1T} & fT_x \\ f\mathbf{R}^{2T} & fT_y \\ \mathbf{R}^{3T} & T_z \end{pmatrix} \mathbf{x}_i \tag{4.27}$$

where $\mathbf{R}^{iT} \in \mathbb{R}^{1\times 3}$ are the row vectors of the rotation matrix.

As the perspective projection is only defined up to a multiplicative factor, Eq. (4.27) could be rewritten by multiplying the projection matrix with $1/T_z$ and denoting $s = F/T_z$:

$$\begin{pmatrix} w'_i u_i \\ w'_i v_i \end{pmatrix} = \begin{pmatrix} s\mathbf{R}^{1T} & sT_x \\ s\mathbf{R}^{2T} & sT_y \end{pmatrix} \begin{pmatrix} x_i \\ y_i \\ z_i \\ 1 \end{pmatrix} \tag{4.28}$$

and

$$w'_i = \mathbf{R}^{3T} \cdot (x_i, y_i, z_i)^T / T_z + 1 \tag{4.29}$$

Assuming $w'_i = 1$, Eq. (4.28) describes a scaled orthographic projection [33]. In Eq. (4.28) there are 8 unknowns: $s\mathbf{R}^1, sT_x, s\mathbf{R}^2, sT_y$. If at least $n \geq 4$ non co-planar point correspondences are given, the equation system can be solved for $s, \mathbf{R}^1, \mathbf{R}^2, \mathbf{R}^3$, T_x, T_y, T_z. Starting with $w = 1$, we can solve the system of equations in (4.28), substitute the values into Eq. (4.29) to re-estimate w. This iteration is repeated until convergence.

Rotation parameterization

Central question in solving Eq. (4.19) is how to parameterize the rotation matrix. The nine elements of the 3×3 rotation matrix $\mathtt{R}$ only have three degrees of freedom and need to satisfy $\mathtt{R}\mathtt{R}^T = \mathtt{R}^T\mathtt{R} = \mathtt{I}^{3\times3}$, $det(\mathtt{R}) = 1$ and $\mathtt{R}^T = \mathtt{R}^{-1}$, where $\mathtt{I}^{3\times3}$ is the identity matrix. Various representations were proposed in the literature such as unconstrained 3×3 matrix, Cayley-Klein [70], unit- [96] or non-unit quaternion [218] or Rodrigues' form [64, 109]. Each has different strengths for the various solving strategies. Early works employed a two step approach, first relaxing the orthogonality constraint and in a second phase enforcing it. Cayley and quaternion representations are preferred if the problem is solved as a multivariate polynomial system, while Rodrigues' rotation formula uses trigonometric functions and avoids any singularities.

Rodrigues' form encodes a rotation around an arbitrary axis $\mathbf{a} = \frac{\mathbf{r}}{\|\mathbf{r}\|}$ with angle $\alpha = \|\mathbf{r}\|$. We define

$$\mathtt{C} = \begin{bmatrix} 0 & -a_z & a_y \\ a_z & 0 & -a_x \\ -a_y & a_x & 0 \end{bmatrix} \quad s.t. \quad \mathbf{a} = \begin{bmatrix} a_x \\ a_y \\ a_z \end{bmatrix} \tag{4.30}$$

and thus the rotation is expressed as

$$\mathtt{R}(\mathbf{r}) = \mathtt{I} + \sin\alpha\mathtt{C} + (1 - \cos\alpha)\mathtt{C}^2 \tag{4.31}$$

yielding

$$\mathtt{R}(\mathbf{r}) = \begin{bmatrix} \cos\alpha + a_x^2(1-\cos\alpha) & a_x a_y(1-\cos\alpha) - a_z\sin\alpha & a_y\sin\alpha + a_x a_z(1-\cos\alpha) \\ a_z\sin\alpha + a_x a_y(1-\cos\alpha) & \cos\alpha + a_y^2(1-\cos\alpha) & -a_x\sin\alpha + a_y a_z(1-\cos\alpha) \\ -a_y\sin\alpha + a_x a_z(1-\cos\alpha) & a_x\sin\alpha + a_y a_z(1-\cos\alpha) & \cos\alpha + a_z^2(1-\cos\alpha) \end{bmatrix}. \tag{4.32}$$

During minimization this formula enforces the special orthogonal group property on the elements of $\mathtt{R}$ without additional constraints. As a result it is ensured that $\mathtt{R}$ is an orthogonal rotation matrix.

We can now further specify the PnP optimization problem from Eq. (4.19) substituting the rotation matrix from Rodrigues' form (4.31) and Euclidean norm:

$$\mathbf{r}^*, \mathbf{t}^* = \arg\min_{\mathbf{r},\mathbf{t}} \sum_{i=1}^{n} \left\| \mathtt{K}\left[\mathtt{R}(\mathbf{r})|\mathbf{t}\right]\mathbf{x}_i - \mathbf{x}_i' \right\|^2 \tag{4.33}$$

where $\mathbf{r}, \mathbf{t} \in \mathbb{R}^3$.

Iterative refinement

The two previous methods approached the PnP minimization problem in Eq. (4.19) with simplifying assumptions. DLT minimizes a un-intuitive algebraic error, while POSIT iterates under an approximate weak-perspective assumption. However in

Algorithm 4: Iterative, gradient descent optimization

Data: given cost function F
Data: given initial parameter values $\mathbf{x}_0$
Data: given maximum number of iterations k_{MAX}
$k := 0$, $\mathbf{x} := \mathbf{x}_0$;
do
  find descent direction: $\mathbf{h}_d$;
  find a step length giving a good decrease in the cost: α;
  apply correction $\mathbf{x} := \mathbf{x} + \alpha\mathbf{h}_d$;
  $k := k + 1$;
while $k < k_{MAX}$ *and* $\|\mathbf{h}_d\| > \epsilon$;
Result: Pick $\mathbf{x}^* = \mathbf{x}$ as local minimizer

Eq. (4.33) the minimization is constructed over the geometrically meaningful distance between the measured and estimated image coordinates. This distance is the cumulative residual of the projection error of the feature points.

The classical approach to solve such non-linear least-squares problems are iterative, gradient-based methods [115]. See Algorithm 4 for overview of the general gradient descent method. Gradient-based minimization[6] attempts to find the parameter values $\mathbf{x}^*$ that result in the smallest energy (cost) starting from an initial parameter value $\mathbf{x}_0$ and using the first derivative (gradient) and maybe second derivative of the cost function F. The search for global optimum is very difficult and generally only local minimizers are attainable, depending on the initial value. The method searches for a local stationary point indicated by zero gradient.

Various approaches have been proposed to compute the descent direction $\mathbf{h}_d$. The Levenberg-Marquardt (LM) algorithm combines the steepest descent and Gauss-Newton methods for finding the descent direction. This approximation takes place without computing the Hessian containing the second derivatives [115]:

$$\left(\mathtt{J}^T\mathtt{J} + \mu\mathtt{I}\right)\mathbf{h}_{lm} = -\mathtt{J}^T f \tag{4.34}$$

where μ is a scalar damping parameter and $\mathtt{J} \in \mathbb{R}^{2n\times 6}$ is the Jacobian matrix containing the partial derivatives of the function components (residuals) of the cost function F, and n is the number of point correspondences. The Rodrigues' parameterization allows both symbolic and numeric differentiation to compute the Jacobian.

If the distribution of noise in the measurements follows Gaussian assumption, the least squares solution is the maximum likelihood (ML) estimate. The iterative refinement may be initialized by the output of the DLT or POSIT algorithms.

For further information on the PnP problem and non-linear least squares minimization see the books on *Multiple View Geometry in Computer Vision* [64] and *Methods for non-linear least squares problems (2ns ed.)* [115].

[6] During optimization we could also search for a maximizer.

4.1.6. Error Analysis

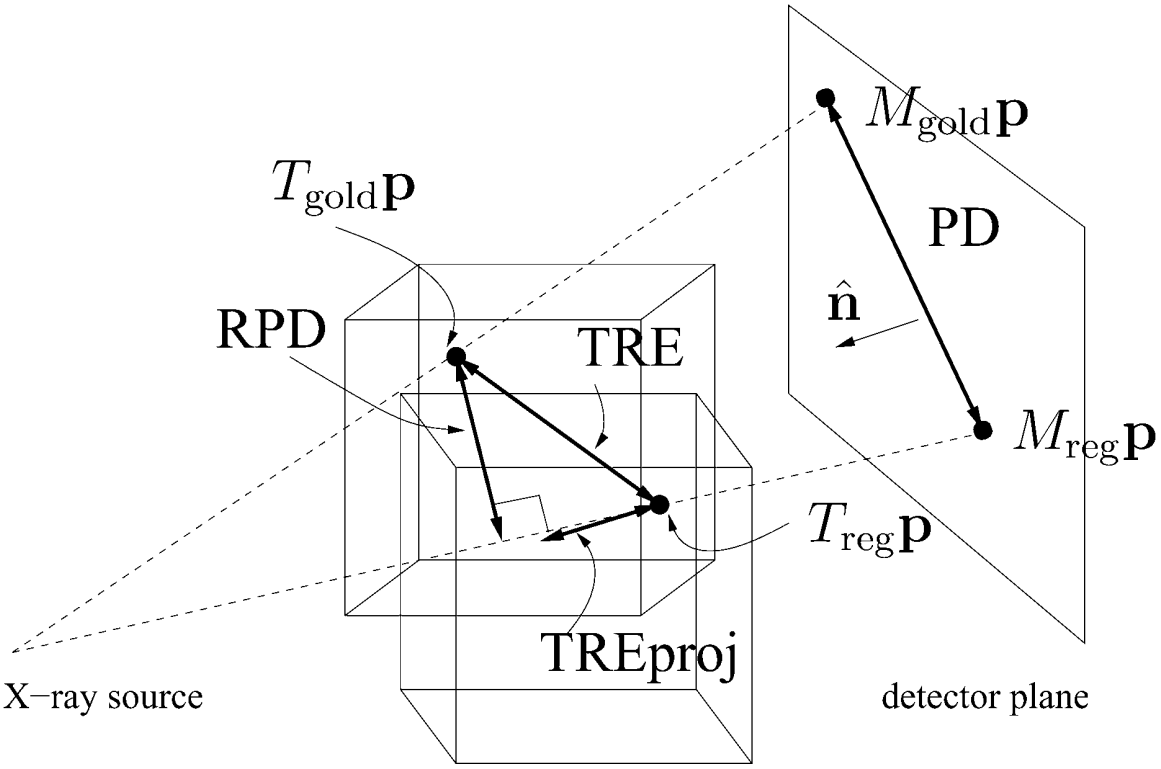

Figure 4.2.: Illustration of error measures. Reproduced from van de Kraats et al. [30].

To describe the quality and performance of an interventional fusion system and the underlying registration approach, we have to assess both the accuracy and the robustness of the method at hand.

A point-based, rigid registration algorithm accumulates error from multiple sources. The classical nomenclature introduced by Maurer et al. [125] defines the following metrics: i) fiducial localization error (FLE) describing the accuracy of localizing the fiducial markers used as registration points; ii) fiducial registration error (FRE) which is the root-mean-squared error of corresponding fiducial points after calculating alignment transformation and iii) target registration error (TRE) is representing the distance between corresponding points not used during registration. TRE is generally considered the clinically most important error measure of registration accuracy. Fitzpatrick et al. [43, 44, 42] investigated statistical properties of the target registration error in $3D-3D$ and proved that TRE and FRE are uncorrelated. This means that for truthful registration accuracy evaluation the FRE should not be used and the TRE needs to be computed.

In order to quantify registration accuracy, a reference of comparison has to be defined as well. van de Kraats et al. [30] developed a "gold standard" evaluation framework for $2D-3D$ registration between X-Ray and CT/MR. The authors' pro-

tocol established the ground truth results through a calibrated C-arm CT scan and implanted fiducial markers. The calibration means that the optimized projection parameters $\mathtt{P} = \mathtt{K}[\mathtt{R}|\mathbf{t}]$ are available for all X-Ray projection images used for 3D reconstruction of the C-arm CT volume. Key to the methodology is a $3D-3D$ rigid registration $\mathtt{T}_{3D-3D}$ to align the fiducial markers in C-arm CT and the target CT/MR. Assuming a projection image, van de Kraats et al. proposes the "gold standard" registration as $\mathtt{T}_{gold} = \begin{bmatrix} \mathtt{R} & \mathbf{t} \\ \mathbf{0}^T & 1 \end{bmatrix} \mathtt{T}_{3D-3D}$, $\mathtt{T}_{gold} \in \mathbb{R}^{4\times4}$.

Besides the above method, van de Kraats et al. [30] proposed three different accuracy measures specific of $2D$-$3D$ registration (see Figure 4.2). The evaluation is proposed to be carried out on a fixed set of k $3D$ points $\{\mathbf{p}_i\}, i = 1, 2, \ldots, k$ uniformly distributed in the volume of interest. The mean value of TRE (mTRE) over this set is computed as

$$mTRE = \frac{1}{k}\sum_{i=1}^{k} \|\mathtt{T}_{reg}\mathbf{p}_i - \mathtt{T}_{gold}\mathbf{p}_i\| \tag{4.35}$$

such that $\mathtt{T}_{reg} \in \mathbb{R}^{4\times4}$ is the registration transformation. mTRE is the normalized, accumulated Euclidean distances between points $\mathbf{p}_i$ transformed by the registration and "gold standard" mappings.

To quantify the registration error in the X-Ray image plane [30] proposed the projection of the TRE: mean projection distance (mPD) denoting the distance between the projections of the registered and "gold standard" points:

$$mPD = \frac{1}{k}\sum_{i=1}^{k} \|(\mathtt{M}_{reg}\mathbf{p}_i - \mathtt{M}_{gold}\mathbf{p}_i)\|\,. \tag{4.36}$$

where $\mathtt{M}_{gold} = \mathtt{T}_{proj}\mathtt{T}_{gold}$ and $\mathtt{M}_{reg} = \mathtt{T}_{proj}\mathtt{T}_{reg}$ with $\mathtt{T}_{proj} \in \mathbb{R}^{3\times4}$ denoting the known C-arm system calibration matrix (intrinsic projection parameters).

An other way to interpret the error is through the mean reprojection distance (mRPD) [123, 30]. mRPD measures the distance between the "gold standard" position of a point and a ray from the X-Ray source to the registered point position:

$$mRPD = \frac{1}{k}\sum_{i=1}^{k} \|D_{LP}(\mathbf{L}_i(XR\ source, \mathtt{T}_{reg}\mathbf{p}_i), \mathtt{T}_{gold}\mathbf{p}_i)\| \tag{4.37}$$

where D_{LP} is the $3D$ distance between a line and a point. Additionally we propose the metric "effective TRE". The effective value of TRE (ETRE) is computed by keeping only the TRE vector components which are parallel to the detector plane.

$$mETRE = \frac{1}{k}\sum_{i=1}^{k} \|(\mathtt{T}_{reg}\mathbf{p}_i - \mathtt{T}_{gold}\mathbf{p}_i)\cdot\hat{\mathbf{n}}_{\perp}\| \tag{4.38}$$

where $\cdot\hat{\mathbf{n}}_{\perp}$ denotes projection onto the imaging plane and $\hat{\mathbf{n}}$ is the negative projection direction (see Figure 4.3). The motivation behind this metric may be explained by

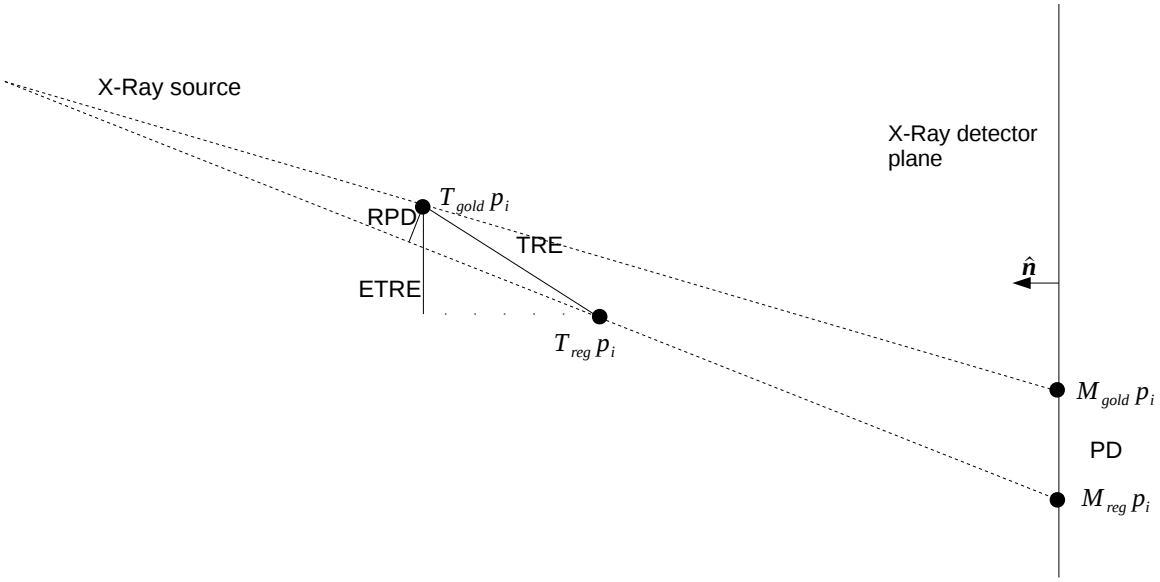

Figure 4.3.: Illustration of effective TRE accuracy measure in comparison to TRE and RDP.

the overlay nature the fusion system is expected to be used: ultrasound images (or ultrasound segmentation) are projected onto the XR image. In this scenario, the depth component of the error would visually "vanish".

Assessment of registration robustness is aimed at understanding the statistical properties of a registration method: what is the confidence value in the accuracy? Typically performed in a controlled experiment, the failure rate of the algorithm is evaluated under varying noise of the input data. In point-based $2D-3D$ registration, the sensitivity of the registration accuracy (TRE) on noisy fiducial localization (FLE) is of interest. Success is usually defined by a clinical user as a tolerance or threshold on e.g. TRE dictated by requirements of the envisaged procedure.

4.2. Model of Fiducials Equipped Ultrasound Catheter

4.2.1. Fiducials in Feature-based Registration

Even though during a cardiac intervention both fluoroscopy and echo image the same anatomy, due to the high-contrast dynamic clutter (e.g. catheters, guide-wires and tools in XRF) and the different principles of imaging, defining a practically useful similarity measure between these two modalities is a very difficult task. On the other hand, during an intervention the projection of the ICE catheter is captured in XRF images. Based on this observation, we will use features of the catheter itself that are visible in XRF to define correspondences and the registration data term: Equations

(4.6) and (4.7).

Point-based registration was extensively studied in the 1990s. Mauerer et al. [125] devised a system that allowed $3D-3D$ registration of CT and MR volumes. The authors have developed fiducial markers that were brightly visible both in CT and MR as point-like structures. Five of these fiducial markers were rigidly screwed to the skull. The space of correspondence was exhaustively searched, while $3D-3D$ point fitting was performed in the least-squares sense, for which closed-form solution exists [194]. Thorough evaluation showed that the system is accurate enough for neuro-surgical use.

Jain et al. [86] investigated robustness of fiducial designs for single-image X-Ray fluoroscopy tracking. The authors argue that non-spherical fiducials achieve higher registration accuracy due to more precise segmentation. Thereby Jain et al. introduced the FTRAC fiducial design consisting of carefully aligned ellipses, lines and points. FTRAC was realized as a rigidly attachable device with $30 \times 30 \times 50mm$ dimensions. Phantom-based accuracy studies indicated sum-mm translational and sub-degree rotational accuracy. The authors simulated $10 \times 10 \times 20mm$ FTRAC design with similar results.

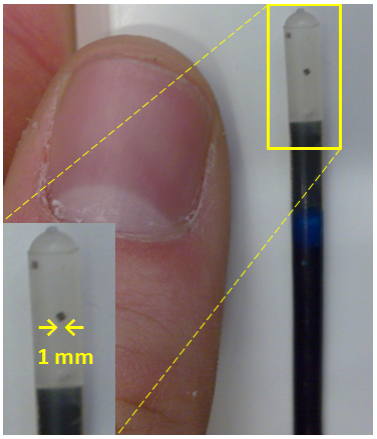

Figure 4.4.: Illustration of ball marker sizes in a prototype ICE catheter.

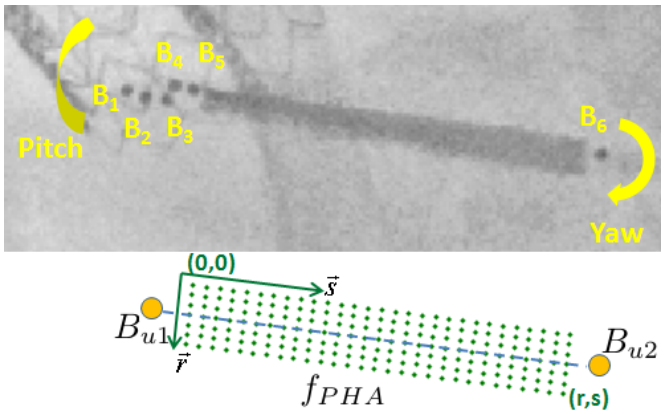

Figure 4.5.: (**a**)Typical view of ICE prototype in XRF. (**b**)Model used for 2D localization: steerable grid pattern defined by positions of $\{B_{u1}, B_{u2}\}$

4.2.2. Fiducial Marker Design

Even though we would have preferred to use state of the art fiducials, the catheter dimensions constrained the design. The fiducial configuration may not block the acoustic window of the ICE catheter and the fiducials must be compatible with catheter production diameter of $13F = 4.333mm$ and approximately $35mm$ long rigid tip.

Figure 4.6.: Volume rendered C-arm CT reconstruction of fiducials equipped prototype ICE catheter. The 3D constellation of the beads is visible. The metallic beads appear larger due to partial volume effect and interpolated transfer function.

To facilitate our needs, we have developed a prototype ICE catheter and fitted it with radiopaque ball markers (beads, Figures 4.4 and 4.6). Each marker is assigned a unique virtual identifier ($\mathbf{b}_i, i \in \{1, .., 6\}$), the empirical design of five distal and single proximal ball markers is shown in Figure 4.5 together with the phased array (PHA) transducer. The 3D catheter pose is parameterized as (x', y', z') position and rotation: around "long axis" of PHA (α_{Roll}), out-of-plane (β_{Pitch}) and in-plane (γ_{Yaw}).

4.3. Fitting the Model to Interventional X-Ray images

4.3.1. Overview

During cardiac interventions, multiple catheters, wires and tools are commonly visible in XRF. The C-arm may have arbitrary oblique angulations, dye injection could change contrast conditions. As opposed to TEE that is always directed down the esophagus, ICE might arrive from different directions to the target area, unrestricted in 6 degrees of freedom (DoF). In summary, it is expected that fluoroscopic images will not provide global context to support the detection problem.

Our automatic 2D catheter detection algorithm (Figure 4.7 and Algorithm 5) consists of (i) permissive ball marker detector and likelihood measure of PHA foreground/background, (ii) robust hypothesis fusion strategy and (iii) accurate hypothesis refinement.

In the last part, we discuss technical details for registration of ICE and XRF. Building on the catheter detection method, we use 2D location of ball markers from a single projection X-Ray for point correspondence determination and 3D pose estimation of ICE.

Throughout the method, we assume that the tip of the ICE catheter (including the ball markers and transducer) is rigid.

Algorithm 5: ICE-XRF fusion algorithm

Data: given XRF image I including the ICE catheter
Data: given 3D constellation of bead centroids in ICE catheter $\{\mathbf{x}_i\}$
Coarse 2D catheter localization in I using PBT inference:
$\boldsymbol{\theta}_B = \{(x, y), \gamma_{Yaw}, s_x\}$;
Refine detection of 2D bead centroids in neighborhood of $\boldsymbol{\theta}_B$: $\{\mathbf{b}'_i\}$;
for *each combination of correspondences* $\mathcal{C} = 1, 2, \ldots, 6!$ *in parallel* **do**
  Perform POSIT with given correspondence;
  to calculate initial estimate of $\mathbf{r}, \mathbf{t}$;
  Perform iterative refinement of $\mathbf{r}, \mathbf{t}$ using non-linear optimization with LM;
  Compute cumulative projection residual of beads:

$$\mathcal{E}_{\{\mathcal{C},\mathbf{r},\mathbf{t}\}} = \sum_{i=1}^{6} \left\| \mathtt{K}\,[\mathtt{R}(\mathbf{r})|\mathbf{t}]\,\mathbf{b}_{\mathcal{C}(i)} - \mathbf{b}'_i \right\|$$

Result: Pick $\{\mathcal{C}, \mathbf{r}, \mathbf{t}\}$ with smallest projection error $\mathcal{E}$.

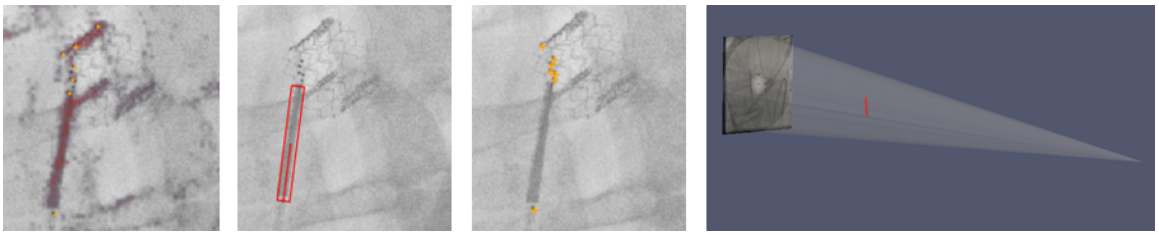

Figure 4.7.: (**a**)Initial ball marker estimates and likelihood measure of Phased Array (PHA) transducer foreground are integrated for (**b**)robust, coarse localization of catheter. (**c**)Ball marker locations are refined. (**d**)6 DoF 3D pose is estimated together with 2D-3D point correspondences.

4.3.2. Approximate 2D Catheter Localization

The goal of the first step is to define the region of the XRF image I containing the catheter. We search for catheter parameters $\boldsymbol{\theta}^*$ maximizing the posterior probability:

$$\boldsymbol{\theta}^* = \arg\max_{\boldsymbol{\theta}} p(\boldsymbol{\theta}|I) \tag{4.39}$$

It is difficult to provide an analytic solution for Eq. (4.39), as $\boldsymbol{\theta}$ is defined in the space of 2D projections of the 3D catheter/markers. Thus, for coarse localization, the catheter model is approximated as a line segment (Figure 4.7 **(b)**):

$$\boldsymbol{\theta} \approx \boldsymbol{\theta}_B = \{(x, y), \gamma_{Yaw}, s_x\} \tag{4.40}$$

where (x, y), γ_{Yaw}, s_x are 2D position, orientation and length of PHA. In contrast to TEE [133], the elongated shape of ICE catheter is not distinctive enough for these parameters to be estimated directly, hence we introduce a natural, parts based decomposition of $\boldsymbol{\theta}_B$. The segment is described as a pair of $\{\mathbf{b}_{u1}, \mathbf{b}_{u2}\}$ ball markers[7] and the likelihood $f_{PHA} = f\left(p\left(PHA|I\right), \mathbf{b}_{u1}, \mathbf{b}_{u2}\right)$ of the phased array located in between them:

$$\{(x, y), \gamma_{Yaw}, s_x\} = g\left(\mathbf{b}_{u1}, \mathbf{b}_{u2}, f_{PHA}\right) \tag{4.41}$$

with $(x, y) = \frac{1}{2}(\mathbf{b}_{u1} + \mathbf{b}_{u2})$, $\gamma_{Yaw} = \tan\left(\frac{\delta y}{\delta x}(\mathbf{b}_{u2} - \mathbf{b}_{u1})\right)$ and $s_x = \|\mathbf{b}_{u2} - \mathbf{b}_{u1}\|$. This hierarchical decomposition allows to rewrite the argument of Eq. (4.39) too:

$$p(\boldsymbol{\theta}|I) \approx p(\mathbf{b}_{u1}|I) \cdot p(\mathbf{b}_{u2}|I) \cdot f\left(p\left(PHA|I\right), \mathbf{b}_{u1}, \mathbf{b}_{u2}\right) \tag{4.42}$$

where $p(\mathbf{b}_i|I)$ and $p(PHA|I)$ refer to the posterior distribution of ball markers and the phased array in I, respectively.

Training the Model

The hierarchical decomposition defines the search spaces in more tractable terms. Our goal is to train two pixel wise classifiers, both employed in a sliding window approach: one bead detector for $p(\mathbf{b}_i|I)$ similar to [112], and secondly a classifier $p(PHA|I)$ for the likelihood of a pixel belonging to the phased array transducer. Both detectors are implemented as a cascade of two levels, where during training the second level is trained on false positives from the first level as negative examples. Probabilistic boosting trees [193] are constructed to a depth of three, and include 50 weak learners in each node. The weak learners are image responses of discrete Haar-like features. The detectors are implemented in the flexible integrated detection network (IDN) framework [177]. $p(\mathbf{b}_i|I)$ is trained on super-sampled 0.25 mm resolution images, while sub-sampled 1 mm is used for the PHA likelihood measure to smooth out the finer, rotationally variant structure of the phased array transducer.

Detection Procedure and Hypothesis Fusion

During detection, the goal is to estimate the segment $\boldsymbol{\theta}_B$ using the trained model on unseen images. Due to scattered background, both bead and transducer classifiers produce a high rate of false alarms. In order to reliably extract the ICE catheter, we exploit local context ($g(\cdot)$ in (4.41)) and fuse pairs of ball markers $\{\mathbf{b}_{u1}, \mathbf{b}_{u2}\}_k$ and PHA candidates.

The hypothesis fusion consists of the following steps: (i) the top 40 locations indicated by $p(\mathbf{b}_i|I)$ are clustered, (ii) $p(PHA|I)$ is evaluated on the whole image,

[7] At this point $\mathbf{b}_{u1}$ may be any of the five distal beads (ambiguities in perspective projection of various ICE poses hinder determination of exact distal marker id), also $\mathbf{b}_{u1}$ and $\mathbf{b}_{u2}$ may be swapped as the segment is invariant to 180° rotations).

producing a confidence map for the transducer likelihood and (iii) we select all possible pairs of marker hypotheses that satisfy the distance constraint[8] and finally (iv) the candidate pairs are scored by f_{PHA} a steerable filter (Figure 4.5**(b)**), defined on the likelihood map: first taking the maximum response in each "column" along $\overleftarrow{s}$, then the $10th$ percentile of the remaining single row, in order to penalize hypotheses with low max. response along the $\{\mathbf{b}_{u1}, \mathbf{b}_{u2}\}$ axis. This score is used to sort all $\boldsymbol{\theta}_B$ candidates in Eq. (4.39).

4.3.3. Search for Fiducials in 2D

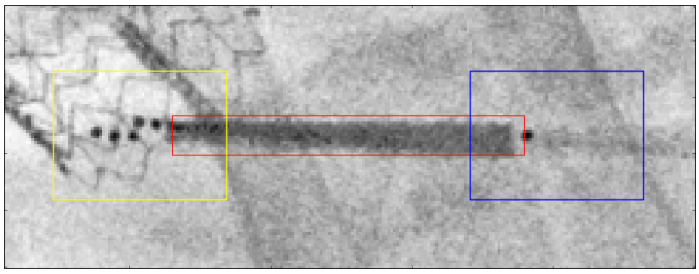

Figure 4.8.: Results of approximate localization ($\boldsymbol{\theta}_B$, red frame), and predicted search ranges for fiducial ball markers (V_{u1},V_{u2}; yellow and blue frames)

The approximated coarse location is used to anchor two bounding boxes enclosing the two tails (Figure 4.8) of the phased array: $\{V_{u1}, V_{u2}\}$. Searching within these reduced neighborhoods, we intend to accurately localize and determine the identity of the visible fiducial beads and decide which end of the catheter is the distal one. Under various projections, the ball markers start to touch each other and overlap, making the identification difficult. In order to be able to recover partially overlapping markers, we created a circular template image (with its diameter dictated by the smallest marker in our images). The template is overlayed $\{V_{u1}, V_{u2}\}$ in a sliding window manner, the response for each pixel is calculated as the correlation coefficient of the overlapping regions. Local peaks are extracted that are further apart than one pixel. The resulting peaks are treated as marker candidates. The distal end of the catheter and $\{\mathbf{b}_{dist_i}\}$ is indicated by more beads among the two neighborhoods. If more than one marker is present in the proximal area, we suppress the non maximum responses to keep the most likely one as $\mathbf{b}_{prox}$.

[8] from the C-arm we know the source-table distance that together with allowed catheter pitches (Figure 4.5**(a)**) limits the 2D span of the proximal and distal markers visible in the X-Ray projection

4.4. Pose estimation and Registration

Registration of ICE and XRF is establishing a spatial relationship between ICE voxels $P_{ICE\_vox}(x_I, y_I, z_I)$ and XRF pixels $P_{Fluoro}(u, v)$:

$$P_{Fluoro}(u, v) = T^{C-arm}_{\rightarrow Fluoro} T^{ICE\_cath}_{\rightarrow C-arm} T^{ICE\_vox}_{\rightarrow ICE\_cath} P_{ICE\_vox}(x_I, y_I, z_I) \tag{4.43}$$

Here, the cone-beam perspective projection, intrinsic parameters (defined in the pinhole camera model) and C-arm angulation are combined in $T^{C-arm}_{\rightarrow Fluoro}$, and are considered known from the calibrated C-arm system itself. Also, the geometric relationship between the ICE image and ICE catheter $T^{ICE\_vox}_{\rightarrow ICE\_cath}$ is considered known from calibration, leaving the 3D pose of the ICE catheter in the 3D C-arm coordinates $T^{ICE\_cath}_{\rightarrow C-arm}$ unknown in (4.43).

Estimation of $T^{ICE\_cath}_{\rightarrow C-arm}$ based on fiducial beads constitutes solving a feature-based $2D$-$3D$ registration problem defined in Eq. (4.18). Thus the purpose of pose estimation is to infer the rigid transform $T^{ICE\_cath}_{\rightarrow C-arm}$ consisting of a rotation $\mathtt{R}(\mathbf{r}) = (\alpha_{Roll}, \beta_{Pitch}, \gamma_{Yaw})^T$ and translation $\mathbf{t} \equiv (x', y', z')^T$. For this we need to determine the correspondence $\mathcal{C}$ between ball markers on the catheter $\left\{\mathbf{b}'_j\right\}$ and the extracted 2D marker projections $\{\mathbf{b}_i\}$.

We address the correspondence problem within $\{\mathbf{b}_{dist_i}\}$ with an exhaustive search: for each combinations of markers, we solve the PnP problem in Eq. (4.19). We execute a version of POSIT [33] and the results are used to initialize iterative optimization of pose using the Levenberg-Marquardt method (Sec. 4.1.5). The estimated pose of beads is projected to the X-Ray plane. Using the sum of 2D point-to-point ($\sum$P2P= $\mathcal{E}_{\{\mathcal{C},\mathbf{r},\mathbf{t}\}} = \sum_{i=1}^{6} \left\| \mathtt{K}\left[\mathtt{R}(\mathbf{r})|\mathbf{t}\right] \mathbf{x}_{\mathcal{C}(i)} - \mathbf{x}'_i \right\|$) distance, we pick the marker combination that yields the smallest residual. It is notable that each iteration of the combinatorial search is independent and may thus be performed concurrently.

4.5. Experiments and Results

4.5.1. Data Sets

Our learning based models require large amounts of examples to train a classifier. Manually labeling markers in real X-Ray sequences is a laborious task, and reliable 3D Ground Truth (GT) location of the markers would require a co-registered C-arm CT. As such data was not readily available, we synthesised Digitally Reconstructed Radiographs (DRR) from a 3D image of the catheter and background fluoroscopies without ICE. DRRs allow the 3D GT to be generated at the same time. We produced 11 000 ($0 \leq \alpha_{Roll} \leq 360, -30 \leq \beta_{Pitch} \leq 30, -180 \leq \gamma_{Yaw} \leq 180$) randomized images for training and 1 000 images for testing. In addition, we captured 641 XRF frames from an *in-vivo* porcine study and manually annotated the beads. 400 of these frames were used for training, the remaining 241 for testing. Example images are shown in Figure 4.9.

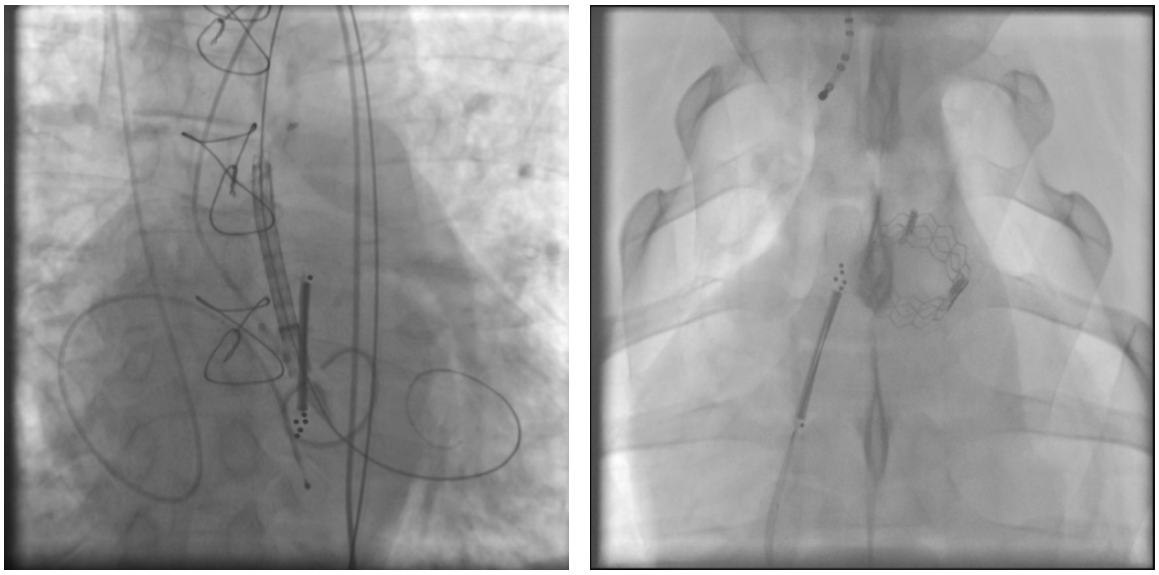

Figure 4.9.: Synthetic digitally reconstructed radiograph (DRR) and *in-vivo* porcine X-Ray images of the fiducial equipped prototype ICE catheter.

	synthetic	in-vivo
No. of Images	1000	241
Success/Rate	979/97.9%	235/97.5%
Avg±Std	1.20±0.55	1.10±0.58

Table 4.1.: 2D catheter $\boldsymbol{\theta}_B$ localization performance, translation error in mm.

Line segment detection accuracy is shown in Table 4.1. More than 97% of the cases are successfully ($\| (\delta x, \delta y) \| < 5\ mm$, $\gamma_{Yaw} < 5°$) detected which is comparable to the state of the art [113, 112].

For the rest of the evaluation, we have selected those cases, where hypothesis fusion and template matching was able to localize a single proximal (B_{Prox}) and five distal beads ($\|\{\mathbf{b}_{Dist_i}\}\| = 5$). These represent those cases where direct correspondence can be established, assuming beads do not overlap. 715 (71.5%) and 193 (80.0%) such cases were detected for DRR and *in-vivo* data, respectively. Native resolution of the tested X-Ray images is in the range of 0.3 to 0.4 mm, sub-pixel accuracy is achieved by our marker detection shown in Table 4.2. We also report the symmetric Hausdorff distance[9] of the marker localization to show the maximum distance of closest detections and closest ground truth.

To evaluate the accuracy for the envisioned image fusion application, we employ the target registration error (TRE). The target points are defined as the four corners of the sound cone at the depth of 50 mm. The effective value of TRE (ETRE) is computed by keeping only the TRE components which are parallel to the detector

[9]See Eq. (4.10) for definition.

	synthetic	in-vivo
No. of Images	715 (71.5%)	193 (80.0%)
Symmetric	0.31±1.55	0.22±0.19
Hausdorff	0.67±3.73	0.36±0.51

Table 4.2.: Point-to-point 2D marker localization performance, error in mm, displayed as mean±std. dev. Considered in images where $\boldsymbol{\theta}_B$ succeeded and $\|\{\mathbf{b}_{Dist_i}\}\| = 5$.

plane. Due to lacking 3D GT, we could only evaluate the 6 DoF pose estimation on the 715 DRR images for which all markers could be detected. 12 cases were excluded, where the sum of 2D point-to-point distance was above 1 mm. In the remaining 703 images the correspondence and 3D pose estimation performed well, yielding an average TRE of 8.06 ± 7.2 mm and ETRE of 2.81 ± 1.5 mm (Table 4.3).

	Roll °	Pitch °	Yaw °	Depth mm	TRE mm	ETRE mm
Mean±Std.	2.03±1.5	2.07±1.6	0.13±0.2	7.28±7.8	8.06±7.2	2.81±1.5
Median/P_{90}	1.76/4.21	1.68/4.37	0.10/0.25	4.74/17.93	5.54/17.58	2.59/4.84

Table 4.3.: 3D pose estimation accuracy on DRR cases where $\|\{\mathbf{b}_{Dist_i}\}\| = 5$. From 715, we excluded 12 cases where $\sum$P2P projection error is above 1 mm.

An other interesting error measure links the uncertainty of marker localization (FLE) to the accuracy of the target registration error (TRE). Using the synthetic DRR data-set, we have simulated the uncertainty of FLE by superimposing anisotropic Gaussian noise to the ground truth 2D marker locations and calculated the registration error. The results are tabulated in Table 4.4.

4.6. Discussion

The overall 2D marker detection error is lower for *in-vivo* data compared to synthetic. This is due to the fact, that the X-Ray sequences used as background for DRR generation are from actual cardiac interventions, and contain various other wires and

noise P2P	noise $\sum$P2P	Roll °	Pitch °	Yaw °	Depth mm	TRE mm
0.13±0.06	0.75±0.16	2.16±1.8	2.08±1.8	0.11±0.1	6.88±7.2	7.76±6.8
0.28±0.15	1.68±0.36	5.17±4.5	4.81±4.3	0.26±0.2	16.19±16.5	18.14±15.5
0.40±0.21	2.38±0.51	7.50±7.1	7.41±7.0	0.38±0.3	23.58±25.0	26.62±23.2
0.57±0.30	3.39±0.75	11.80±12.8	10.49±9.0	0.59±0.5	33.91±33.6	38.68±30.8

Table 4.4.: TRE as a function of increasing uncorrelated Gaussian noise in FLE shown as mean±std. dev.

tools that appear similar to the ICE catheter, while the porcine data featured less clutter.

The 3D TRE is non-isotropic: the depth direction contributes the major part of the error, as small inaccuracies of detected beads in the X-Ray detector plane are magnified along its normal. Similarly the large pitch error is related to imperfect depth recovery. When targets are displayed as overlays on the 2D XRF images, the depth error "disappears". To reflect this clinical scenario, we introduced the ETRE. The $2.81 \pm 1.5\ mm$ ETRE is comparable to the $5\ mm$ range envisaged by our interventional collaborators as clinically useful.

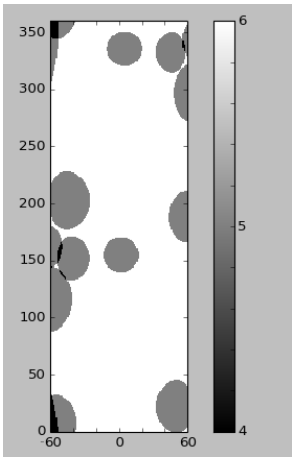

Figure 4.10.: Number of visible markers. The X and Y axes show roll and pitch, respectively in degrees.

Fitzpatrick et al. have shown that the 3D constellation of the fiducial markers influences the target registration error [44]. The empirical design of bead placements (Sec. 4.2.2) – due to the small elongated shape of the catheter tip – resulted in an almost collinear configuration with respect to the C-arm projection cone. Solving the PnP problem under collinear configuration is not possible in all six degrees of freedom, and a close to collinear geometry makes recovery of the rotation around the axis of collinearity difficult. This is consistent with our results showing large error in roll recovery. As an effect of the relative pose of the catheter and C-arm, in the projection image beads do overlap[10] and it becomes not possible to distinguish them based on their location XRF alone (Fig. 4.10).

The results in Table 4.4 indicate an almost linear relationship between the average FLE and average TRE.

In our investigation we have considered the both the C-arm calibration $T^{C-arm}_{\rightarrow Fluoro}$ and ultrasound calibration $T^{ICE\_vox}_{\rightarrow ICE\_cath}$ given. In reality these calibrations are not completely perfect either and should be included in an end-to-end error analysis.

[10]We define overlap as the projected fiducial centroids' distance smaller than a XRF pixel.

4.6.1. Clinical Application Scenarios

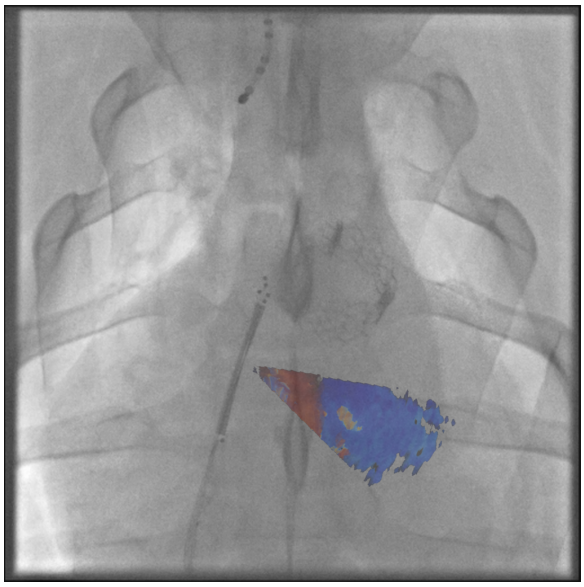

Figure 4.11.: Interventional fusion of Doppler-mode volumetric ICE and X-Ray fluoroscopy.

In Section 2.2.2 various interventional uses of ICE were described in SHD patients. The additional clinical value of the system outlined in this chapter could be realized by bringing information extracted from live echo images and combine it with X-Ray fluoroscopy at registered locations. For example, after the transcatheter implantation of heart valves, a crucial step involves checking for a good seal and looking for paravalvular leaks. Echocardiography could provide fusion of blood flow (Doppler echo) information (see Fig. 4.11) without contrast agent. Similarly, residual leaks and regurgitation may be overlaid on X-Ray at the registered location. Furthermore, after registration, segmented objects or soft-tissue landmarks (virtual landmarks) could be transferred to X-Ray that are otherwise not visible. Candidate methods include the recent work of Voigt et al. [201], where the feasibility of real-time ultrasound segmentation of soft tissue such as mitral heart valve (MV) was demonstrated.

CHAPTER 5

Conclusions

The focus of this dissertation has been image analysis based methods for treatment outcome prediction and intervention guidance in cardiovascular diseases (CVD). In this chapter the proposed models and thesis contributions are reviewed, limitations of the models are identified and possible future works outlined.

5.1. Summary

CVD is the leading cause of death in the USA and Europe. Invasive cardiovascular procedures have proven to be the riskiest and most expensive type of therapy. In Section 2 we have briefly reviewed the human cardiac anatomy and function, including pathological variations of congenital and structural heart disease. Adding to the background, cardiac imaging modalities (Sec. 2.2) were briefly surveyed. To address the burden of CHD and SHD, medicine is increasingly relying on personalized, predictive and less-invasive practices. Data-driven, advanced medical image analysis methods enable building knowledge from personalized anatomical, functional and computational models to support clinical decisions (Sec. 2.3).

In this spirit, in Section 3, our main contribution to the field is an end-to-end pipeline for image-based hemodynamic assessment of blood pressure drop in coarctation of the aorta without invasive catheterization. The system was shown to compare well against invasive blood pressure catheterization. The complete workflow is realized in a fast, automated system that can be integrated into a clinical setting, where manual interaction is required in a mostly supervisional manner. A set of validation experiments has shown that the proposed methods work on a wide variety of low-quality, retrospective data. Automatic thoracic aorta segmentation was applied on a population of 212 3D MR volumes, with mean point-to-mesh error of 3.00 ± 1.58 mm

and average computation time of $8s$. Good agreement between computed blood pressure drop $\triangle P$ and catheter measurements is shown through quantitative evaluation of corresponding retrospective pre- (2.38 ± 0.82 mm Hg) and post-operative (1.10 ± 0.63 mm Hg) data and virtual stenting (4.99 ± 3.00 mm Hg) setup of 6 CoA patients. The data stems from regular clinical practice of multiple cardiac centers in the USA and the EU and was not explicitly acquired for simulation studies. Furthermore, all data used for parameter personalization were acquired noninvasively, which is important considering the often young age of CoA patients. We have demonstrated that the framework is applicable to three stages of CoA care: preoperative severity assessment, post-stenting follow-up, and treatment outcome prediction through "virtual stenting". We believe that the presented non-invasive in-silico method has the potential — given more thorough clinical validation – to replace invasive pressure catheterization for CoA.

Advanced image guidance and information fusion in hybrid operating rooms enables emerging minimally invasive procedures and devices for SHD. The complementary imaging information from live fluoroscopy and echocardiography has the potential to guide structural heart disease interventions. Section 4 — to the best of our knowledge — discusses the first published method to automatically register intracardiac echocardiography with X-Ray fluoroscopy avoiding general anesthesia. Extraction of the echocardiography catheter relies on robust and fast machine learning methods. The registration method is agnostic to catheters as long as both ends are beads marked, and connected with a visible part in between, hence, general enough to be used for other devices. We provided quantitative evaluation on a number of real and synthetic images and arrived at convincing preliminary results. The method reached 8.06 ± 7.2 mm TRE on 703 cases with an in-plane component (effective TRE) of 2.81 ± 1.5 mm.

Through sections 3 and 4 we have shown how two image-based methods could reduce invasiveness in all four phases of CVD management. The question arises whether the two systems could be used together? We believe, yes, during percutaneous therapy of the coarctation of aorta, the image fusion system could be used. It should be noted however, the greater efficiency enabled by advanced guidance could benefit the treatment of more complicated (Sec. 2.1.2) forms of CVD, especially where X-Ray fluoroscopy alone is not sufficient.

5.2. Limitations and Future Works

5.2.1. Non-invasive Blood Pressure Drop Estimation

We have shown, that the presented models can be used to assess the blood pressure conditions of CoA. However, our method opens several technical and clinical questions.

Our pre-defined anatomic part and shape model based segmentation method applies

only to cases that exhibit shape variation, but do not change in topology. In complex congenital heart defects topological changes in the circulation cannot be ruled out, CoA often coincides with other aortic arch morbidities. The presented morphology model and lumen segmentation is not directly able to represent such pathological variations, thus extraction of diseased vessel anomalies (e.g. other than three supra-aortic arteries, loop of aorta, collateral circulation as shown on Fig. 2.3b) would be beneficial to be included in the system. Currently we do not handle such cases automatically.

Secondly, a single plane of velocity encoded cine PC-MR image might not be able to capture the flow of intercostal arteries and collateral vessels. If such arteries are present bypassing the coarctation site, possibly multiple PC-MR planes are required to capture their flow, and the clinical imaging protocol would have to be extended.

It would be interesting to quantify the sensitivity of the hemodynamic simulation results as a function of the accuracy of the segmented aorta and coarctation lumen surfaces, similar to [17].

5.2.2. Peri-operative Image Fusion

The current technique requires all 6 fiducial markers to be extracted from the X-Ray to allow pose recovery of the echocardiography catheter. It would be desirable to allow pose estimation with more or less number of detected fiducial hypotheses. Future work should be aimed at techniques to recover pose from only 3 or 4 visible distal markers, and to automatically exclude extraneous marker candidate outliers (e.g. using RANSAC).

The current fiducial bead constellation was developed empirically. With simple fiducials such as the spherical beads it should be possible to optimize the marker configuration geometry to minimize overlaps in projection images. Once the catheter is navigated to scan the desired part of the anatomy, it would be interesting to understand what are the most optimal C-arm angulations to look at the catheter to minimize the target registration error?

Moreover, investigation of propagation of temporal information (catheter tracking) across consecutive XRF images would be desirable to increase detection rate in challenging backgrounds.

APPENDIX A

Publications

A.1. Publications as First Author

A.1.1. Journal

- K. Ralovich, L. Itu, D. Vitanovski, P. Sharma, R. Ionasec, V. Mihalef, W. Krawtschuk, Y. Zheng, A. Everett, G. Pongiglione, B. Leonardi, R. Ringel, N. Navab, T. Heimann, D. Comaniciu: Non-invasive Hemodynamic Assessment, Treatment Outcome Prediction and Follow-up of Aortic Coarctation from MR Imaging, *Medical Physics*, 42: 2143-2156, 2015

A.1.2. Conference

- K. Ralovich, M. John, E. Camus, N. Navab, T. Heimann: 6DoF Catheter Detection, Application to Intracardiac Echocardiography, *Medical Image Computing and Computer-Assisted Intervention - MICCAI 2014*, 2014

- K. Ralovich, L. Itu, V. Mihalef, P. Sharma, R. Ionasec, D. Vitanovski, W. Krawtschuk, A. Everett, R. Ringel, N. Navab, D. Comaniciu: Hemodynamic Assessment of Pre- and Post-Operative Aortic Coarctation from MR Images *Proceedings of the 15th International Conference on Medical Image Computing and Computer Assisted Interventions (MICCAI), Nice, France, October 2012*, 2012

- K. Ralovich, L. Itu, V. Mihalef, P. Sharma, R. Ionasec, D. Vitanovski, A. Everett, W. Krawtschuk, M. Suehling, N. Navab, D. Comaniciu: Non-invasive Assessment of Aortic Coarctation through Blood Flow Computation and MRI

VPH2012 Integrative approaches to computational biomedicine - The Virtual Physiological Human Initiative Scientific Sessions 2012, 2012

- K. Ralovich, V. Mihalef, P. Sharma, L. Itu, D. Vitanovski, R. Ionasec, M. Suehling, A. Everett, G. Pongiglione, N. Navab, D. Comaniciu: Modeling and Simulation Framework for Hemodynamic Assessment of Aortic Coarctation Patients *ISMRM '12: Proceedings of the 20th Scientific Meeting and Exhibition of International Society for Magnetic Resonance in Medicine*, 2012
- K. Ralovich, R. Ionasec, V. Mihalef, P. Sharma, B. Georgescu, A. Everett, N. Navab, D. Comaniciu: *Computational Fluid Dynamics Framework for Large-Scale Simulation in Pediatric Cardiology, Computational Biomechanics for Medicine VI (CBM6) MICCAI Workshop*, 2011

A.2. Publications as Co-author

A.2.1. Journal

- L. Itu, P. Sharma, K. Ralovich, V. Mihalef, R. Ionasec, A. Everett, R. Ringel, A. Kamen, D. Comaniciu: Non-Invasive Hemodynamic Assessment of Aortic Coarctation: Validation with In Vivo Measurements; *Annals of Biomedical Engineering*, 2013
- M. Sofka, K. Ralovich, J. Zhang, K. Zhou,: Progressive Data Transmission for Anatomical Landmark Detection in a Cloud; *Methods of Information in Medicine, 2012, Invited Paper.*, 2012

A.2.2. Conference

- D. Vitanovski, K. Ralovich, Razvan Ioan Ionasec, Yefeng Zheng, M. Suehling, W. Krawtschuk, J. Hornegger, D. Comaniciu: Personalized Learning-based Segmentation of Thoracic Aorta and Main Branches for Diagnosis and Treatment Planning *IEEE International Symposium on Biomedical Imaging, Barcelona, Spain*, 2012
- M. Sofka, K. Ralovich, N. Birkbeck, J. Zhang, K. Zhou: Integrated Detection Network (IDN) For Pose And Boundary Estimation *In Medical Images IEEE International Symposium on Biomedical Imaging: From Nano to Macro (ISBI 2011), Chicago, Illinois, USA, March 30 - April 2, 2011*, 2011
- M. Sofka, K. Ralovich, J. Zhang, K. Zhou,: Progressive Data Transmission for Hierarchical Detection in a Cloud *Proceedings of the 2nd International Workshop on High-Performance Medical Image Computing for Image-Assisted Clinical Intervention and Decision-Making (HP-MICCAI 2010), Bejing, China, 22 Sep 2010.*, 2010

APPENDIX B

Patents, Invention Disclosures

B.1. Granted Patents

- 8 811 697, Progressive Data Transmission for Hierarchical Detection in a Cloud, United States Patent, `http://www.freepatentsonline.com/8811697.pdf`

- 9 135 699 $B2$, Hemodynamic Assessment of Pre- and Post-Operative Aortic Coarctation from MR Images, United States Patent
`http://www.freepatentsonline.com/9135699.pdf`

(12) **United States Patent**
Sofka et al.

(10) **Patent No.: US 8,811,697 B2**
(45) **Date of Patent: Aug. 19, 2014**

(54) **DATA TRANSMISSION IN REMOTE COMPUTER ASSISTED DETECTION**

(75) Inventors: **Michal Sofka**, Franklin Park, NJ (US); **Kristof Ralovich**, Princeton, NJ (US); **Jingdan Zhang**, Plainsboro, NJ (US); **Shaohua Kevin Zhou**, Plainsboro, NJ (US); **Gianluca Paladini**, Skillman, NJ (US); **Dorin Comaniciu**, Princeton Junction, NJ (US)

(73) Assignee: **Siemens Aktiengesellschaft**, Munich (DE)

(*) Notice: Subject to any disclaimer, the term of this patent is extended or adjusted under 35 U.S.C. 154(b) by 411 days.

(21) Appl. No.: **13/080,891**

(22) Filed: **Apr. 6, 2011**

(65) **Prior Publication Data**

US 2011/0243407 A1 Oct. 6, 2011

Related U.S. Application Data

(60) Provisional application No. 61/321,222, filed on Apr. 6, 2010.

(51) **Int. Cl.**
G06K 9/00 (2006.01)
G06K 9/62 (2006.01)
G06T 7/00 (2006.01)

(52) **U.S. Cl.**
CPC ***G06K 9/6256*** (2013.01); *G06T 2207/20016* (2013.01); ***G06F 19/231*** (2013.01); *G06T 2200/16* (2013.01); ***G06T 7/0012*** (2013.01)
USPC **382/128**; 382/131; 382/132; 382/154; 382/240

(58) **Field of Classification Search**
USPC 382/128, 131, 132, 133, 154, 240
See application file for complete search history.

(56) **References Cited**

U.S. PATENT DOCUMENTS

6,314,452	B1 *	11/2001	Dekel et al.	709/203
6,891,973	B1 *	5/2005	Atsumi et al.	382/232
2005/0129271	A1 *	6/2005	Shi et al.	382/100
2010/0119137	A1	5/2010	Schwing et al.	
2010/0240996	A1	9/2010	Ionasec et al.	

OTHER PUBLICATIONS

Tu Z. Probabilistic Boosting-Tree: Learning Discriminative Models for Classification, Recognition, and Clustering. In: CVPR. vol. 2; 2005. p. 1589-1596.

Viola P, Jones MJ. Rapid object detection using a boosted cascade of simple features. In: CVPR. vol. 1; 2001. p. 511-518.

Schnitzspan P, Fritz M, Roth S, Schiele B. Discriminative structure learning of hierarchical representations for object detection. In: CVPR; 2009. p. 2238-2245.

Zhang W, Zelinsky G, Samaras D. Real-time Accurate Object Detection using Multiple Resolutions. In: ICCV; 2007.

(Continued)

Primary Examiner — Tom Y Lu

(57) **ABSTRACT**

For cloud-based computer assisted detection, hierarchal detection is used, allowing detection on data at progressively greater resolutions. Detected locations at coarser resolutions are used to limit the data transmitted at greater resolutions. Data is only transmitted for neighborhoods around the previously detected locations. Subsequent detection using higher resolution data refines the locations, but only for regions associated with previous detection. By limiting the number and/or size of regions provided at greater resolutions based on the previous detection, the progressive transmission avoids transmission of some data. Additionally, or alternatively, lossy compression may be used without or with minimal reduction in detection sensitivity.

20 Claims, 2 Drawing Sheets

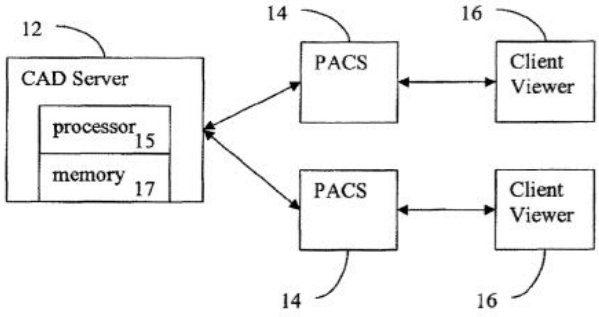

Figure B.1.: Granted US Patent 8 811 697

(12) **United States Patent**
Ralovich et al.

(10) **Patent No.: US 9,135,699 B2**
(45) **Date of Patent: Sep. 15, 2015**

(54) **METHOD AND SYSTEM FOR HEMODYNAMIC ASSESSMENT OF AORTIC COARCTATION FROM MEDICAL IMAGE DATA**

(71) Applicants: **Kristof Ralovich**, Munich (DE); **Lucian Mihai Itu**, Brasov (RO); **Viorel Mihalef**, Keasbey, NJ (US); **Puneet Sharma**, Monmouth Junction, NJ (US); **Razvan Ioan Ionasec**, Princeton, NJ (US); **Dime Vitanovski**, Erlangen (DE); **Waldemar Krawtschuk**, Erlangen (DE); **Dorin Comaniciu**, Princeton Junction, NJ (US)

(72) Inventors: **Kristof Ralovich**, Munich (DE); **Lucian Mihai Itu**, Brasov (RO); **Viorel Mihalef**, Keasbey, NJ (US); **Puneet Sharma**, Monmouth Junction, NJ (US); **Razvan Ioan Ionasec**, Princeton, NJ (US); **Dime Vitanovski**, Erlangen (DE); **Waldemar Krawtschuk**, Erlangen (DE); **Dorin Comaniciu**, Princeton Junction, NJ (US)

(73) Assignee: **Siemens Aktiengesellschaft**, Munich (DE)

(*) Notice: Subject to any disclaimer, the term of this patent is extended or adjusted under 35 U.S.C. 154(b) by 315 days.

(21) Appl. No.: **13/826,307**

(22) Filed: **Mar. 14, 2013**

(65) **Prior Publication Data**

US 2013/0243294 A1 Sep. 19, 2013

Related U.S. Application Data

(60) Provisional application No. 61/611,057, filed on Mar. 15, 2012.

(51) **Int. Cl.**
G06K 9/00 (2006.01)
G06T 7/00 (2006.01)

(52) **U.S. Cl.**
CPC ***G06T 7/0012*** (2013.01); *G06T 2207/10076* (2013.01); *G06T 2207/10096* (2013.01); *G06T 2207/30104* (2013.01)

(58) **Field of Classification Search**
None
See application file for complete search history.

(56) **References Cited**

U.S. PATENT DOCUMENTS

5,150,292	A *	9/1992	Hoffmann et al.	600/431
5,579,767	A *	12/1996	Prince	600/420
5,953,444	A *	9/1999	Joseph et al.	382/131
7,860,290	B2	12/2010	Gulsun et al.	
7,953,266	B2	5/2011	Gulsun et al.	
8,098,918	B2	1/2012	Zheng et al.	
8,386,188	B2	2/2013	Taylor et al.	

(Continued)

OTHER PUBLICATIONS

"Effects of exercise and respiration on hemodynamic efficiency in cfd simulations of the total cavopulmonary connection," Marsden A. L., et al, Annals of Biomedical Engineering, vol. 35, No. 2, Feb. 2007, pp. 250-263.*

(Continued)

Primary Examiner — Wenpeng Chen

(57) **ABSTRACT**

A method and system for non-invasive hemodynamic assessment of aortic coarctation from medical image data, such as magnetic resonance imaging (MRI) data is disclosed. Patient-specific lumen anatomy of the aorta and supra-aortic arteries is estimated from medical image data of a patient, such as contrast enhanced MRI. Patient-specific aortic blood flow rates are estimated from the medical image data of the patient, such as velocity encoded phase-contrasted MRI cine images. Patient-specific inlet and outlet boundary conditions for a computational model of aortic blood flow are calculated based on the patient-specific lumen anatomy, the patient-specific aortic blood flow rates, and non-invasive clinical measurements of the patient. Aortic blood flow and pressure are computed over the patient-specific lumen anatomy using the computational model of aortic blood flow and the patient-specific inlet and outlet boundary conditions.

29 Claims, 8 Drawing Sheets

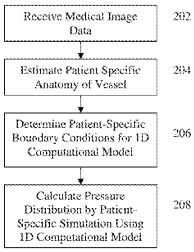

Figure B.2.: Granted US Patent 9 135 699

B.2. Patent Applications

- *US* 20160287214 *A*1, Three-dimensional volume of interest in ultrasound imaging, United States Patent Application
  `http://www.freepatentsonline.com/20160287214.pdf`

US 20160287214A1

(19) **United States**

(12) **Patent Application Publication**

Ralovich et al.

(10) **Pub. No.: US 2016/0287214 A1**

(43) **Pub. Date: Oct. 6, 2016**

(54) **THREE-DIMENSIONAL VOLUME OF INTEREST IN ULTRASOUND IMAGING**

(71) Applicant: **Siemens Medical Solutions USA, Inc.**, Malvern, PA (US)

(72) Inventors: **Kristof Ralovich**, Erlangen (DE); **Tobias Heimann**, Erlangen (DE); **Wilko Gerwin Wilkening**, Mountain View, CA (US)

(21) Appl. No.: **14/673,583**

(22) Filed: **Mar. 30, 2015**

Publication Classification

(51) **Int. Cl.**

A61B 8/08 (2006.01)

A61B 8/00 (2006.01)

(52) **U.S. Cl.**

CPC . ***A61B 8/483*** (2013.01); ***A61B 8/08*** (2013.01); ***A61B 8/5215*** (2013.01); ***A61B 8/463*** (2013.01); ***A61B 8/469*** (2013.01)

(57) **ABSTRACT**

A volume of interest is ultrasonically imaged. An object of interest is automatically located from a volume scan. In one approach, a geometric bounding box surrounding the object is found by a classifier. In another approach, an option for zooming to the object is indicated to the user. A scan region is defined around the object or the bounding box automatically, whether in response to user selection of the option or not. The scan region is shaped based on the ultrasound scan format, but is smaller than the volume. The volume of interest defined by the scan region is used to generate images with a greater temporal and/or spatial resolution than scanning of the entire original volume.

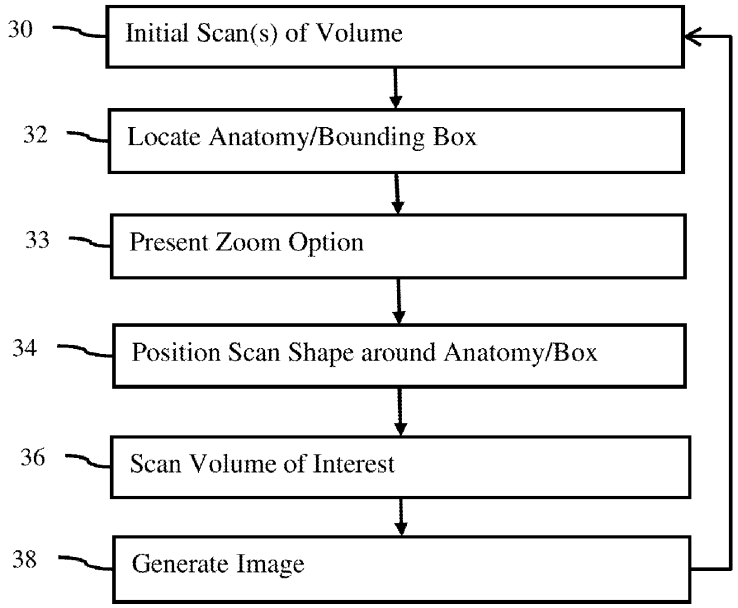

Figure B.3.: US Patent Application 2016/028 7214 *A*1

B.3. Invention Disclosures

- Sparse Ultrasound Acquisition with Image-defined 3D "Volume of Interest" 2014E17199 DE
- Sparse Ultrasound Acquisition with "Smart" Focus 2014E09822 DE
- Spatial Compounding of 2D and 3D Volume ICE, based on catheter pose tracking from Fluoroscopy 2014E09820 DE
- 6DoF Catheter Detection for Intracardiac Echocardiography 2014E05374 DE
- Computational Fluid Dynamics Framework for Large-Scale Simulation in Pediatric Cardiology 2011E27119 US 201127
- Progressive Data Transmission for Anatomical Landmark Detection in a Cloud 2011E22168 US 201122
- Integrated Detection Toolkit (IDTK) for Multiple Object Detection 2011E01050 US 201101
- Integrated Detection Network (IDN) for Pose and Boundary Estimation in Medical Images 2010E25957 US 201026

APPENDIX C

Notation and Nomenclature

S_i	segment i in axisymmetric model of arterial tree
A_{DiAo}	cross sectional area at diaphragm level
A_c	coarctation minimum cross sectional area
L_c	coarctation (pre-operative S_7) length
p	arterial pressure
q (Q)	flow rate, time-varying (constant, averaged)
t	time
x	location along centerline
α	the momentum-flux correction coefficient
ω	Womersley number
ρ	$= 1.055\ g/cm^3$, blood density
μ	$= 4.5\ mPa \cdot s$, dynamic viscosity
K_R	friction parameter (Eq. 3.33)
K_t	$= 1.52$, turbulence coefficient (Eq. 3.39)
K_u	$= 1.2$, inertance coefficient (Eq. 3.39)
E	Young's modulus
h_i	wall thickness of segment i
θ_o	similarity transform of part o
T_{CoA}	stenosis rate (morphologic)
H_R	heart rate
$\overline{P_A}$	mean arterial pressure
$\overline{P_{sy}}$ $(\overline{P_{di}})$	the systolic (diastolic) cuff pressures (arm)
n	number of PC-MR frames (per cardiac cycle)
c	pressure wave speed

Bibliography

[1] Medical electrical equipment - part 2-34: Particular requirements for the basic safety and essential performance of invasive blood pressure monitoring equipment. In *IEC 60601-2-34*. IEC/ANSI, November 2011. [Accessed: Jun. 10, 2014].

[2] Abbott. Figure of Mitraclip device. `https://www.vascular.abbott/us/products/structural-heart/mitraclip-mitral-valve-repair/_jcr_content/subsectiontoppar/productdetails/images/1/image.img.png/1479415459200.png`, 2008. Accessed: 2015-09-10.

[3] YI Abdel-Aziz. Karara. hm (1971) direct linear transformation from comparator coordinates into object-space coordinates in close-range photogrammetry. *Proceedings of the ASP/UI Symposium on Close-Range Photogrammetry. Falls Church. VA: American Society of Photogrammetry*, 1971.

[4] Alexus Allman at Slideplayer. Figure of thoracic aorta. `http://player.slideplayer.com/4/1417426/data/images/img14.jpg`, 2015. Accessed: 2015-11-10.

[5] Eric Pierce at Wikipedia. Diagram of the human heart. `https://en.wikipedia.org/wiki/Atrium_(heart)#/media/File:Diagram_of_the_human_heart_(cropped).svg`, 2006. Accessed: 2015-01-13.

[6] Emile AM Bacha and Ziyad M Hijazi. Hybrid procedures in pediatric cardiac surgery. In *Seminars in Thoracic and Cardiovascular Surgery: Pediatric Cardiac Surgery Annual*, volume 8, pages 78–85. Elsevier, 2005.

[7] Jan Balzer, Malte Kelm, and Harald P. Kühl. Real-time three-dimensional transoesophageal echocardiography for guidance of non-coronary interventions in the catheter laboratory. *European Heart Journal - Cardiovascular Imaging*, 10(3):341–349, 2009.

[8] Thomas Bartel, Nikolaos Bonaros, Ludwig Müller, Guy Friedrich, Michael Grimm, Corinna Velik-Salchner, Gudrun Feuchtner, Florian Pedross, and Silvana Müller. Intracardiac echocardiography: a new guiding tool for transcatheter aortic valve replacement. *Journal of the American Society of Echocardiography*, 24(9):966–975, 2011.

[9] Herbert Bay, Tinne Tuytelaars, and Luc Van Gool. Surf: Speeded up robust features. *Computer vision–ECCV 2006*, pages 404–417, 2006.

[10] J. B. Bell, P. Colella, and H. M. Glaz. A second-order projection method for the incompressible Navier-Stokes equations. *J. Comput. Phys.*, 1989.

[11] H. Bentall and A. De Bono. A technique for complete replacement of the ascending aorta. *Thorax*, 23(4), 1968.

[12] Guillaume Bouchard and Bill Triggs. The tradeoff between generative and discriminative classifiers. In *16th IASC International Symposium on Computational Statistics (COMPSTAT'04)*, pages 721–728, 2004.

[13] Michael A Bowes, Graham R Vincent, Christopher B Wolstenholme, and Philip G Conaghan. A novel method for bone area measurement provides new insights into osteoarthritis and its progression. *Annals of the rheumatic diseases*, 74(3):519–525, 2015.

[14] Y. Boykov and V. Kolmogorov. An experimental comparison of min-cut/max-flow algorithms for energy minimization in vision. *Pattern Analysis and Machine Intelligence, IEEE Transactions on*, 26(9):1124 –1137, 2004.

[15] Herng-Hua Chang, Gary R. Duckwiler, Daniel J. Valentino, and Woei Chyn Chu. Computer-assisted extraction of intracranial aneurysms on 3d rotational angiograms for computational fluid dynamics modeling. *Medical Physics*, 36(12):5612–5621, 2009.

[16] Weijia Chen, Lucian Itu, Puneet Sharma, and Ali Kamen. Uncertainty quantification in medical image-based hemodynamic computations. In *Biomedical Imaging (ISBI), 2014 IEEE 11th International Symposium on*, pages 433–436, April 2014.

[17] Weijia Chen, Lucian Itu, Puneet Sharma, and Ali Kamen. Uncertainty quantification in medical image-based hemodynamic computations. In *Biomedical Imaging (ISBI), 2014 IEEE 11th International Symposium on*, pages 433–436, April 2014.

[18] Dorin Comaniciu, Bogdan Georgescu, Ali Kamen, Tommaso Mansi, and Viorel Mihalef. System and method for estimating artery compliance and resistance from 4d cardiac images and pressure measurements, October 11 2016. US Patent 9,462,952.

[19] Jessica Shih Coogan, Frandics Pak Chan, Charles Anthony Taylor, and Jeffrey Allan Feinstein. Computational fluid dynamic simulations of aortic coarctation comparing the effects of surgical- and stent-based treatments on aortic compliance and ventricular workload. *Catheterization and Cardiovascular Interventions*, 77(5):680–691, 2011.

[20] T. Cootes. Active shape models-their training and application. *Computer Vision and Image Understanding*, 61(1):38–59, 1995.

[21] Volcano Corporation. Figure of volcano IVUS catheter. `http://www.volcanocorp.com/products/image-gallery.php`, 2013. Accessed: 2014-04-23.

[22] Volcano Corporation. Figure of volcano IVUS workstation. `https://photos.medwrench.com/equipmentPhotos/12000/12634-14575-m.jpg`, 2013. Accessed: 2014-04-23.

[23] C. Crafoord and G. Nylin. Congenital coarctation of the aorta and its surgical treatment. *J. Thoracic Surg.*, 14:347, 1946.

[24] Alain Cribier, Helene Eltchaninoff, Assaf Bash, Nicolas Borenstein, Christophe Tron, Fabrice Bauer, Genevieve Derumeaux, Frederic Anselme, François Laborde, and Martin B Leon. Percutaneous transcatheter implantation of an aortic valve prosthesis for calcific aortic stenosis. *Circulation*, 106(24):3006–3008, 2002.

[25] David Cristinacce and Tim Cootes. Automatic feature localisation with constrained local models. *Pattern Recognition*, 41(10):3054–3067, 2008.

[26] Colin Cunnington, Simon A Hampshaw, and Vaikom S Mahadevan. Utility of real-time three-dimensional intracardiac echocardiography for patent foramen ovale closure. *echocardiography*, 26:135–9, 2005.

[27] Navneet Dalal and Bill Triggs. Histograms of oriented gradients for human detection. In *Computer Vision and Pattern Recognition, 2005. CVPR 2005. IEEE Computer Society Conference on*, volume 1, pages 886–893. IEEE, 2005.

[28] Curt J. Daniels, Michael J. Landzberg, and Robert H. Beekman. Structural heart disease. *Journal of the American College of Cardiology*, 65(20):2260–2261, 2015.

[29] Philip David, Daniel Dementhon, Ramani Duraiswami, and Hanan Samet. Softposit: Simultaneous pose and correspondence determination. *IJCV*, 59:259–284, 2004.

[30] Everine B De Kraats, Graeme P Penney, Dejan Tomaževič, Theo Van Walsum, and Wiro J Niessen. Standardized evaluation methodology for 2-d-3-d registration. *Medical Imaging, IEEE Transactions on*, 24(9):1177–1189, 2005.

[31] Jose Suarez de Lezo, Manuel Pan, Miguel Romero, Alfonso Medina, Jose Segura, Mercedes Lafuente, Djordje Pavlovic, Enrique Hernendez, Francisco Melian, and Jose Espada. Immediate and follow-up findings after stent treatment for severe coarctation of aorta. *The American Journal of Cardiology*, 83(3):400 – 406, 1999.

[32] Pierre Del Moral, Arnaud Doucet, and Ajay Jasra. Sequential monte carlo samplers. *Journal of the Royal Statistical Society: Series B (Statistical Methodology)*, 68(3):411–436, 2006.

[33] Daniel F. DeMenthon and Larry S. Davis. Model-based object pose in 25 lines of code. In *ECCV'92*, pages 335–343. 1992.

[34] OpenCV dev team. Figure of haar-like features. `https://docs.opencv.org/2.4/_images/haarfeatures.png`, 2013. Accessed: 2014-11-14.

[35] OpenCV dev team. Figure of pinhole camera model. `https://docs.opencv.org/2.4/_images/pinhole_camera_model.png`, 2013. Accessed: 2014-12-03.

[36] Helen Dolk, Maria Loane, Ester Garne, and European Surveillance of Congenital Anomalies (EUROCAT) Working Group. Congenital heart defects in europe: Prevalence and perinatal mortality, 2000 to 2005. *Circulation*, 123(8):841–849, 2011.

[37] Peter Ewert, Hashim Abdul-Khaliq, Bjoern Peters, Nicole Nagdyman, Stephan Schubert, and Peter E. Lange. Transcatheter therapy of long extreme subatretic aortic coarctations with covered stents. *Catheterization and Cardiovascular Interventions*, 63(2):236–239, 2004.

[38] Francesco Fulvio Faletra, Alamelu Ramamurthi, Maria Cristina Dequarti, Laura Anna Leo, Tiziano Moccetti, and Natesa Pandian. Artifacts in three-dimensional transesophageal echocardiography. *Journal of the American Society of Echocardiography*, 27(5):453–462, 2014.

[39] Mohamed Eid Fawzy, Mahmoud Awad, Walid Hassan, Yusuf Al Kadhi, Mohamed Shoukri, and Fadel Fadley. Long-term outcome (up to 15 years) of balloon angioplasty of discrete native coarctation of the aorta in adolescents and adults. *J Am Coll Cardiol*, 43(6):1062–1067, 2004.

[40] David Faxon. Transcatheter aortic valve implantation coming of age. 124:e439–40, 10 2011.

[41] Enrico Ferrari, Christopher Sulzer, Carlo Marcucci, Elena Rizzo, Piergiorgio Tozzi, and Ludwig K von Segesser. Transapical aortic valve implantation without angiography: proof of concept. *The Annals of thoracic surgery*, 89(6):1925–1932, 2010.

[42] J. Michael Fitzpatrick. Fiducial registration error and target registration error are uncorrelated, 2009.

[43] J Michael Fitzpatrick, Jay B West, and Calvin R Maurer Jr. Predicting error in rigid-body point-based registration. *Medical Imaging, IEEE Transactions on*, 17(5):694–702, 1998.

[44] J.M. Fitzpatrick and J.B. West. The distribution of target registration error in rigid-body point-based registration. *Medical Imaging, IEEE Transactions on*, 20(9):917–927, Sept 2001.

[45] E. Flehmann and et al. Towards patient specific catheter selection: computation of aortic geometry based on fused mri data. In *Proceedings of the 6th international conference on Functional imaging and modeling of the heart*, pages 145–152, 2011.

[46] Consortium for Open Medical Image Computing. Grand challenges in biomedical image analysis, 2007.

[47] Alejandro F Frangi, Wiro J Niessen, and Max A Viergever. Three-dimensional modeling for functional analysis of cardiac images, a review. *IEEE transactions on medical imaging*, 20(1):2–5, 2001.

[48] Alejandro F. Frangi, Zeike A. Taylor, and Ali Gooya. Precision imaging: more descriptive, predictive and integrative imaging. *Medical Image Analysis*, 33:27 – 32, 2016. 20th anniversary of the Medical Image Analysis journal (MedIA).

[49] Yoav Freund and Robert E Schapire. A decision-theoretic generalization of on-line learning and an application to boosting. *J. Comput. Syst. Sci.*, 55(1):119–139, August 1997.

[50] Jerome Friedman, Trevor Hastie, and Robert Tibshirani. *The elements of statistical learning*, volume 1. Springer series in statistics New York, 2001.

[51] D. Gallo, G. Santis, F. Negri, D. Tresoldi, R. Ponzini, D. Massai, M.A. Deriu, P. Segers, B. Verhegghe, G. Rizzo, and U. Morbiducci. On the use of in vivo measured flow rates as boundary conditions for image-based hemodynamic models of the human aorta: Implications for indicators of abnormal flow. *Annals of Biomedical Engineering*, 40(3):729–741, 2012.

[52] Gang Gao, Graeme Penney, Yingliang Ma, Nicolas Gogin, Pascal Cathier, Aruna Arujuna, Geraint Morton, Dennis Caulfield, Jaswinder Gill, C Aldo Rinaldi, et al. Registration of 3d trans-esophageal echocardiography to x-ray fluoroscopy using image-based probe tracking. *Medical image analysis*, 16(1):38–49, 2012.

[53] L.J. Garbini and W.T. Wilser. Multi-twisted acoustic array for medical ultrasound, June 26 2012. US Patent 8,206,305.

[54] Valeria Garro, Fabio Crosilla, and Andrea Fusiello. Solving the pnp problem with anisotropic orthogonal procrustes analysis. *2011 3DIMPVT*, 0:262–269, 2012.

[55] Alan S Go, Dariush Mozaffarian, Véronique L Roger, Emelia J Benjamin, Jarett D Berry, William B Borden, Dawn M Bravata, Shifan Dai, Earl S Ford, Caroline S Fox, et al. Heart disease and stroke statistics–2013 update: a report from the american heart association. *Circulation*, 127(1):e6, 2013.

[56] Colin Goodall. Procrustes methods in the statistical analysis of shape. *Journal of the Royal Statistical Society. Series B (Methodological)*, pages 285–339, 1991.

[57] Leonid Goubergrits, Eugenie Riesenkampff, Pavlo Yevtushenko, Jens Schaller, Ulrich Kertzscher, Anja Hennemuth, Felix Berger, Stephan Schubert, and Titus Kuehne. Mri-based computational fluid dynamics for diagnosis and treatment prediction: Clinical validation study in patients with coarctation of aorta. *Journal of Magnetic Resonance Imaging*, pages n/a–n/a, 2014.

[58] L. Grady. Random walks for image segmentation. *IEEE Transactions on Pattern Analysis and Machine Intelligence*, 28(11):1768–1783, Nov 2006.

[59] Leo Grady, Saurabh Datta, Oliver Kutter, Christophe Duong, Wolfgang Wein, Stephen H. Little, Stephen R. Igo, Shizhen Liu, and Mani Vannan. *Regurgitation Quantification Using 3D PISA in Volume Echocardiography*, pages 512–519. Springer Berlin Heidelberg, Berlin, Heidelberg, 2011.

[60] Saša Grbić, Razvan Ionasec, Yang Wang, Tommaso Mansi, Bogdan Georgescu, Matthias John, Jan Boese, Yefeng Zheng, Nassir Navab, and Dorin Comaniciu. Model-based fusion of multi-modal volumetric images: application to transcatheter valve procedures. In *International Conference on Medical Image Computing and Computer-Assisted Intervention*, pages 219–226. Springer Berlin Heidelberg, 2011.

[61] K. Hameeteman and et al. Evaluation framework for carotid bifurcation lumen segmentation and stenosis grading. *Medical Image Analysis*, 15:477–488, 2011.

[62] Sachin Hansalia, Navin C. Nanda, Naveen Bandarupalli, and Mohit Gupta. Live/real time three-dimensional transthoracic echocardiographic assessment of aortic dissection rupture into right ventricular outflow tract: A case report and review of the literature. *Echocardiography*, 26(1):100–106, 2009.

[63] D A Harrison, P R McLaughlin, C Lazzam, M Connelly, and L N Benson. Endovascular stents in the management of coarctation of the aorta in the adolescent and adult: one year follow up. *Heart*, 85(5):561–566, 2001.

[64] Richard Hartley and Andrew Zisserman. *Multiple View Geometry in Computer Vision*. Cambridge university press, 2003.

[65] Paul A Heidenreich, Justin G Trogdon, Olga A Khavjou, Javed Butler, Kathleen Dracup, Michael D Ezekowitz, Eric Andrew Finkelstein, Yuling Hong, S Claiborne Johnston, Amit Khera, et al. Forecasting the future of cardiovascular disease in the united states a policy statement from the american heart association. *Circulation*, 123(8):933–944, 2011.

[66] T. Heimann, B. van Ginneken, M. A. Styner, Y. Arzhaeva, V. Aurich, C. Bauer, A. Beck, C. Becker, R. Beichel, G. Bekes, F. Bello, G. Binnig, H. Bischof, A. Bornik, P. M. M. Cashman, Y. Chi, A. Cordova, B. M. Dawant, M. Fidrich, J. D. Furst, D. Furukawa, L. Grenacher, J. Hornegger, D. KainmÜller, R. I. Kitney, H. Kobatake, H. Lamecker, T. Lange, J. Lee, B. Lennon, R. Li, S. Li, H. P. Meinzer, G. Nemeth, D. S. Raicu, A. M. Rau, E. M. van Rikxoort, M. Rousson, L. Rusko, K. A. Saddi, G. Schmidt, D. Seghers, A. Shimizu, P. Slagmolen, E. Sorantin, G. Soza, R. Susomboon, J. M. Waite, A. Wimmer, and I. Wolf. Comparison and evaluation of methods for liver segmentation from ct datasets. *IEEE Transactions on Medical Imaging*, 28(8):1251–1265, Aug 2009.

[67] Tobias Heimann, Peter Mountney, Matthias John, and Razvan Ionasec. Learning without labeling: Domain adaptation for ultrasound transducer localization. In *MICCAI 2013*. 2013.

[68] Katrin Hemmann, Margarita Sirotina, Salvatore De Rosa, Joachim R. Ehrlich, Henrik Fox, Johannes Weber, Anton Moritz, Andreas M. Zeiher, Ilona Hofmann, Volker Schächinger, Mirko Doss, Horst Sievert, Stephan Fichtlscherer, and Ralf Lehmann. The STS score is the strongest predictor of long-term survival following transcatheter aortic valve implantation, whereas access route (transapical versus transfemoral) has no predictive value beyond the periprocedural phase. *Interactive CardioVascular and Thoracic Surgery*, 2013.

[69] Martha Hernández-González, Sergio Solorio, Ignacio Conde-Carmona, Alberto Rangel-Abundis, Mariano Ledesma, Jaime Munayer, Felipe David, José Ortegón, Santiago Jimanez, Agustín Sánchez-Soberanis, Carlos Meléndez, Sergio

Claire, Juan Gomez, Raúl Teniente-Valente, and Carlos Alva. Intraluminal aortoplasty vs. surgical aortic resection in congenital aortic coarctation: A clinical random study in pediatric patients. *Archives of Medical Research*, 34(4):305 – 310, 2003.

[70] Joel A Hesch and Stergios I Roumeliotis. A direct least-squares (dls) method for pnp. In *Computer Vision (ICCV), 2011 IEEE International Conference on*, pages 383–390. IEEE, 2011.

[71] Derek LG Hill, Philipp G Batchelor, Mark Holden, and David J Hawkes. Medical image registration. *Physics in medicine and biology*, 46(3):R1, 2001.

[72] Julien I. E. Hoffman and Samuel Kaplan. The incidence of congenital heart disease. *J Am Coll Cardiol*, 39(12):1890–1900, 2002.

[73] Kenneth R Hoffmann and Jacqueline Esthappan. Determination of three-dimensional positions of known sparse objects from a single projection. *Medical physics*, 1997.

[74] Berthold KP Horn. Closed-form solution of absolute orientation using unit quaternions. *JOSA A*, 4(4):629–642, 1987.

[75] P R Hoskins. Accuracy of maximum velocity estimates made using doppler ultrasound systems. *Br J Radiol*, 69(818):172–177, 1996.

[76] R. James Housden, YingLiang Ma, Aruna Arujuna, Niels Nijhof, Pascal Cathier, Geert Gijsbers, Roland Bullens, Jaswinder Gill, C. Aldo Rinaldi, Victoria Parish, and Kawal S. Rhode. Extended-field-of-view three-dimensional transesophageal echocardiography using image-based x-ray probe tracking. *Ultrasound in Medicine & Biology*, 39(6):993 – 1005, 2013.

[77] El-Sayed H Ibrahim, Kevin R Johnson, Alan B Miller, Jean M Shaffer, and Richard D White. Research measuring aortic pulse wave velocity using high-field cardiovascular magnetic resonance: comparison of techniques. 2010.

[78] ADAM Inc. Figure of invasive blood-pressure catheteriation. `http://slu.adam.com/graphics/images/en/18143.jpg`, 2013. Accessed: 2014-09-08.

[79] NuMED Inc. Figure of balloon-in-balloon device. `http://www.numedforchildren.com/nu_images/bib_PTA.jpg`, 2014. Accessed: 2014-05-11.

[80] NuMED Inc. Figure of cheatham-platinum (cp) stent. `http://www.numedforchildren.com/nu_images/CPstent.jpg`, 2014. Accessed: 2014-05-11.

[81] NuMED Inc. Figure of cp stent mounted on delivery catheter. `http://www.numedforchildren.com/nu_images/Mounted%20CP%20Stent2.jpg`, 2014. Accessed: 2014-05-11.

[82] Razvan Ioan Ionasec, Ingmar Voigt, Bogdan Georgescu, Yang Wang, Helene Houle, Fernando Vega-Higuera, Nassir Navab, and Dorin Comaniciu. Patient-specific modeling and quantification of the aortic and mitral valves from 4-d cardiac ct and tee. *IEEE transactions on medical imaging*, 29(9):1636–1651, 2010.

[83] Razvan Ioan Ionasec, Yang Wang, Bogdan Georgescu, Ingmar Voigt, Nassir Navab, and Dorin Comaniciu. Robust motion estimation using trajectory spectrum learning: Application to aortic and mitral valve modeling from 4d tee. In *Computer Vision, 2009 IEEE 12th International Conference on*, pages 1601–1608. IEEE, 2009.

[84] Lucian Itu, Puneet Sharma, Kristóf Ralovich, Viorel Mihalef, Razvan Ionasec, Allen Everett, Richard Ringel, Ali Kamen, and Dorin Comaniciu. Non-invasive hemodynamic assessment of aortic coarctation: Validation with in vivo measurements. *Annals of Biomedical Engineering*, 41(4):669–681, 2013.

[85] Tommi Jaakkola and David Haussler. Exploiting generative models in discriminative classifiers. In *Advances in neural information processing systems*, pages 487–493, 1999.

[86] Ameet Kumar Jain, Tabish Mustafa, Yu Zhou, Clif Burdette, Gregory S. Chirikjian, and Gabor Fichtinger. Ftrac-a robust fluoroscope tracking fiducial. *Medical Physics*, 32(10):3185–3198, 2005.

[87] Marie-Pierre Jolly, Christoph Guetter, and Jens Guehring. Cardiac segmentation in mr cine data using inverse consistent deformable registration. In *ISBI*, pages 484–487, 2010.

[88] Michael Kass, Andrew Witkin, and Demetri Terzopoulos. Snakes: Active contour models. *International journal of computer vision*, 1(4):321–331, 1988.

[89] Ghassan S Kassab and Yuan-Cheng B Fung. The pattern of coronary arteriolar bifurcations and the uniform shear hypothesis. *Annals of biomedical engineering*, 23(1):13–20, 1995.

[90] Leslie I Katzel and Shari R Waldstein. Prevalence of cardiovascular diseace. *Neuropsychology of Cardiovascular Disease*, page 3, 2001.

[91] H. Kim, I. Vignon-Clementel, C. Figueroa, J. LaDisa, K. Jansen, J. Feinstein, and C. Taylor. On coupling a lumped parameter heart model and a three-dimensional finite element aorta model. *Annals of Biomedical Engineering*, 37:2153–2169, 2009. 10.1007/s10439-009-9760-8.

[92] Susan S Kim, Ziyad M Hijazi, Roberto M Lang, and Bradley P Knight. The use of intracardiac echocardiography and other intracardiac imaging tools to guide noncoronary cardiac interventions. *Journal of the American College of Cardiology*, 53(23):2117–2128, 2009.

[93] Richard Kirk. Figure of end-to-end anastomosis. `http://www.crkirk.com/Thumbnail/common/coarct/e-e.gif`, 2004. Accessed: 2014-09-08.

[94] Richard Kirk. Figure of subclavian flap. `http://www.crkirk.com/Thumbnail/common/coarct/subclavian.gif`, 2004. Accessed: 2014-09-08.

[95] Chad Kliger, Ignacio Cruz-Gonzalez, and Carlos E Ruiz. The present and future of intracardiac echocardiography for guiding structural heart disease interventions. *Revista Española de Cardiología*, 65(09):791–794, 2012.

[96] Laurent Kneip, Hongdong Li, and Yongduek Seo. Upnp: An optimal o (n) solution to the absolute pose problem with universal applicability. In *European Conference on Computer Vision*, pages 127–142. Springer, 2014.

[97] Elizabeth A. Krupinski and Yulei Jiang. Anniversary paper: Evaluation of medical imaging systems. *Medical Physics*, 35(2):645–659, 2008.

[98] John F Jr LaDisa, C Alberto Figueroa, Irene E Vignon-Clementel, Hyun Jin Kim, Nan Xiao, Laura M Ellwein, Frandics P Chan, Jeffrey A Feinstein, and Charles A Taylor. Computational simulations for aortic coarctation: representative results from a sampling of patients. *Journal of biomechanical engineering*, 2011.

[99] P. Lang, P. Seslija, M. W. A. Chu, D. Bainbridge, G. M. Guiraudon, D. L. Jones, and T. M. Peters. Us - fluoroscopy registration for transcatheter aortic valve implantation. *IEEE Transactions on Biomedical Engineering*, 59(5):1444–1453, May 2012.

[100] Roberto M Lang, Luigi P Badano, Wendy Tsang, David H Adams, Eustachio Agricola, Thomas Buck, Francesco F Faletra, Andreas Franke, Judy Hung, Leopoldo Pérez de Isla, et al. Eae/ase recommendations for image acquisition and display using three-dimensional echocardiography. *Journal of the American Society of Echocardiography*, 25(1):3–46, 2012.

[101] VS Lee, CE Spritzer, BA Carroll, LG Pool, MA Bernstein, SK Heinle, and JR MacFall. Flow quantification using fast cine phase-contrast mr imaging, conventional cine phase-contrast mr imaging, and doppler sonography: in vitro and in vivo validation. *Am. J. Roentgenol.*, 169(4):1125–1131, 1997.

[102] Vincent Lepetit, Francesc Moreno-Noguer, and Pascal Fua. Epnp: An accurate o (n) solution to the pnp problem. *International journal of computer vision*, 81(2):155, 2009.

[103] David Lesage, Elsa D Angelini, Isabelle Bloch, and Gareth Funka-Lea. A review of 3d vessel lumen segmentation techniques: Models, features and extraction schemes. *Medical image analysis*, 13(6):819–845, 2009.

[104] J. Li, Y. Renardy, and M. Renardy. Numerical simulation of breakup of a viscous drop in simple shear flow through a volume-of-fluid method. *Phys. Fluids*, 2000.

[105] A Lindinger, G Schwedler, and H-W Hense. Prevalence of congenital heart defects in newborns in germany: Results of the first registration year of the pan study (july 2006 to june 2007). *Klinische Pädiatrie*, 222(05):321–326, 2010.

[106] H. Ling, S.K. Zhou, Yefeng Zheng, Bogdan Georgescu, Michael Suehling, and Dorin Comaniciu. Hierarchical, learning-based automatic liver segmentation. In *Proceedings of Conference on Computer Vision and Pattern Recognition*, pages 1–8. IEEE Computer Society, June 2008.

[107] Geert Litjens, Robert Toth, Wendy van de Ven, Caroline Hoeks, Sjoerd Kerkstra, Bram van Ginneken, Graham Vincent, Gwenael Guillard, Neil Birbeck, Jindang Zhang, et al. Evaluation of prostate segmentation algorithms for mri: the promise12 challenge. *Medical image analysis*, 18(2):359–373, 2014.

[108] Joachim Lotz, Christian Meier, Andreas Leppert, and Michael Galanski. Cardiovascular flow measurement with phase-contrast mr imaging: Basic facts and implementation. *Radiographics*, 22(3):651–671, 2002.

[109] Manolis Lourakis and Xenophon Zabulis. Model-Based Pose Estimation for Rigid Objects. In Mei Chen, Bastian Leibe, and Bernd Neumann, editors, *Computer Vision Systems*, volume 7963 of *Lecture Notes in Computer Science*, pages 83–92. Springer Berlin Heidelberg, 2013.

[110] David G Lowe. Object recognition from local scale-invariant features. In *Computer vision, 1999. The proceedings of the seventh IEEE international conference on*, volume 2, pages 1150–1157. Ieee, 1999.

[111] C-P Lu, Gregory D Hager, and Eric Mjolsness. Fast and globally convergent pose estimation from video images. *IEEE Transactions on Pattern Analysis and Machine Intelligence*, 22(6):610–622, 2000.

[112] Xiaoguang Lu, T. Chen, and D. Comaniciu. Robust discriminative wire structure modeling with application to stent enhancement in fluoroscopy. In *CVPR 2011*, page 1121.

[113] Ying Liang Ma, Nicolas Gogin, Pascal Cathier, R James Housden, Geert Gijsbers, Michael Cooklin, Mark O., Jaswinder G., C Aldo R., Reza R., and Kawal S Rhode. Real-time x-ray fluoroscopy-based catheter detection and tracking for cardiac electrophysiology interventions. *Medical Physics*, 2013.

[114] YingLiang Ma, Graeme P Penney, Dennis Bos, Peter Frissen, C Aldo Rinaldi, Reza Razavi, and Kawal S Rhode. Hybrid echo and x-ray image guidance for cardiac catheterization procedures by using a robotic arm: a feasibility study. *Physics in Medicine and Biology*, 2010.

[115] Kaj Madsen, Hans Bruun Nielsen, and Ole Tingleff. Methods for non-linear least squares problems (2ns ed.). 2004.

[116] JB Antoine Maintz and Max A Viergever. A survey of medical image registration. *Medical image analysis*, 2(1):1–36, 1998.

[117] Tommaso Mansi, Ingmar Voigt, Benedetta Leonardi, Xavier Pennec, Stanley Durrleman, Maxime Sermesant, Hervé Delingette, Andrew Mayall Taylor, Younes Boudjemline, Giacomo Pongiglione, et al. A statistical model for quantification and prediction of cardiac remodelling: Application to tetralogy of fallot. *IEEE transactions on medical imaging*, 30(9):1605–1616, 2011.

[118] Tommaso Mansi, Ingmar Voigt, E Assoumou Mengue, R Ionasec, Bogdan Georgescu, Thilo Noack, Joerg Seeburger, and Dorin Comaniciu. Towards patient-specific finite-element simulation of mitralclip procedure. In *International Conference on Medical Image Computing and Computer-Assisted Intervention*, pages 452–459. Springer, Berlin, Heidelberg, 2011.

[119] Song Shou Mao, Nasir Ahmadi, Birju Shah, Daniel Beckmann, Annie Chen, Luan Ngo, Ferdinand R Flores, Matthew J Budoff, et al. Normal thoracic aorta diameter on cardiac computed tomography in healthy asymptomatic adults: impact of age and gender. *Academic radiology*, 15(7):827–834, 2008.

[120] P. Markelj, D. Tomaževič, B. Likar, and F. Pernuš. A review of 3D/2D registration methods for image-guided interventions. *Medical Image Analysis*, 2010.

[121] Michael Markl, Alex Frydrychowicz, Sebastian Kozerke, Mike Hope, and Oliver Wieben. 4d flow mri. *Journal of Magnetic Resonance Imaging*, 36(5):1015–1036, 2012.

[122] Michael Markl, Philip Kilner, and Tino Ebbers. Comprehensive 4d velocity mapping of the heart and great vessels by cardiovascular magnetic resonance. *Journal of Cardiovascular Magnetic Resonance*, 13(1):7, 2011.

[123] Yoshitaka Masutani, Takeyoshi Dohi, Fumitaka Yamane, Hiroshi Iseki, and Kintomo Takakura. Interactive virtualized display system for intravascular neurosurgery. In *CVRMed-MRCAS'97*, pages 427–435. Springer, 1997.

[124] Sean Mauch. Efficient algorithms for solving static Hamilton-Jacobi equations. *PhD Thesis*, 2003.

[125] Calvin R Maurer, J Michael Fitzpatrick, Matthew Y Wang, Robert L Galloway, Robert J Maciunas, and George S Allen. Registration of head volume images using implantable fiducial markers. *IEEE transactions on medical imaging*, 16(4):447–462, 1997.

[126] Tim McInerney and Demetri Terzopoulos. Deformable models in medical image analysis: a survey. *Medical image analysis*, 1(2):91–108, 1996.

[127] BVM Medical. Figure of coa repair via balloon expandable graft covered stent. `https://www.youtube.com/watch?v=bokJwL_Zu3Q`. Accessed: 2014-09-18.

[128] St. Jude Medical. Figure of amplatzer duct occluder. `https://www.sjmglobal.com/~/media/galaxy/hcp/featured-products/structural-heart/amplatzer-duct-occluder-2/amplatzer_duct-occluder-ii_hero_650_v2.jpg`, 2012. Accessed: 2015-09-10.

[129] Medtronic. Figure of CoreValve prosthetic valve. `http://www.whichmedicaldevice.com/uploads/products/large/medtronic-corevalve.jpg`, 2014. Accessed: 2015-09-10.

[130] Viorel Mihalef, Razvan Ioan Ionasec, Puneet Sharma, Bogdan Georgescu, Ingmar Voigt, and et al. Patient-specific modelling of whole heart anatomy, dynamics and haemodynamics from four-dimensional cardiac ct images. In *Interface Focus*, volume 1, pages 286–296, 2011.

[131] Viorel Mihalef, Dimitris Metaxas, Mark Sussman, Vassilios Hurmusiadis, and Leon Axel. Atrioventricular blood flow simulation based on patient-specific data. In *Proceedings of the 5th International Conference on Functional Imaging and Modeling of the Heart*, FIMH '09, pages 386–395, Berlin, Heidelberg, 2009. Springer-Verlag.

[132] Sven Möbius-Winkler, Marcus Sandri, Norman Mangner, Phillip Lurz, Ingo Dähnert, and Gerhard Schuler. The watchman left atrial appendage closure device for atrial fibrillation. *Journal of visualized experiments: JoVE*, (60), 2012.

[133] Peter Mountney, Razvan Ionasec, Markus Kaizer, Sina Mamaghani, Wen Wu, Terrence Chen, Matthias John, Jan Boese, and Dorin Comaniciu. Ultrasound and fluoroscopic images fusion by autonomous ultrasound probe detection. In *MICCAI 2012*, pages 544–551. 2012.

[134] JP Mynard and P Nithiarasu. A 1d arterial blood flow model incorporating ventricular pressure, aortic valve and regional coronary flow using the locally conservative galerkin (lcg) method. *Communications in Numerical Methods in Engineering*, 24(5):367–417, 2008.

[135] Gaku Nakano. Globally optimal dls method for pnp problem with cayley parameterization. In *BMVC*, pages 78–1, 2015.

[136] D. Neumann, S. Grbić, M. John, N. Navab, J. Hornegger, and R. Ionasec. Probabilistic sparse matching for robust 3d/3d fusion in minimally invasive surgery. *IEEE Transactions on Medical Imaging*, 34(1):49–60, Jan 2015.

[137] Andrew Y Ng and Michael I Jordan. On discriminative vs. generative classifiers: A comparison of logistic regression and naive bayes. In *Advances in neural information processing systems*, pages 841–848, 2002.

[138] M Nichols, N Townsend, R Luengo-Fernandez, J Leal, A Gray, P Scarborough, and M Rayner. European cardiovascular disease statistics 2012. *European Heart Network, Brussels, European Society of Cardiology, Sophia Antipolis*, page P104, 2012.

[139] Inc. Nucleus Communications. Figure of cuff-based blood pressure measurement. `https://www.cardiosmart.org/resource/media/medical/hw/h5551017.jpg`, 2003. Accessed: 2014-09-08.

[140] Department of Economic and Social Affairs Population Division. World population ageing 2013. ST/ESA/SER.A/348., 2013.

[141] Timo Ojala, Matti Pietikäinen, and David Harwood. A comparative study of texture measures with classification based on featured distributions. *Pattern recognition*, 29(1):51–59, 1996.

[142] M S Olufsen, C S Peskin, W Y Kim, E M Pedersen, A Nadim, and J Larsen. Numerical simulation and experimental validation of blood flow in arteries with structured-tree outflow conditions. *Annals of Biomedical Engineering*, 28(11):1281–1299, 2000.

[143] IC Omeje, R Poruban, M Šagát, M Nosál, and V Hraška. Surgical treatment of aortic coarctation. *Images in paediatric cardiology*, 6(2):18, 2004.

[144] Michael Oren, Constantine Papageorgiou, Pawan Sinha, Edgar Osuna, and Tomaso Poggio. Pedestrian detection using wavelet templates. In *Computer Vision and Pattern Recognition, 1997. Proceedings., 1997 IEEE Computer Society Conference on*, pages 193–199. IEEE, 1997.

[145] Stanley Osher and James A Sethian. Fronts propagating with curvature-dependent speed: algorithms based on hamilton-jacobi formulations. *Journal of computational physics*, 79(1):12–49, 1988.

[146] A.D. Pasqua and et al. Comparison of contrast and noncontrast magnetic resonance angiography for quantitative analysis of thoracic arteries in young

patients with congenital heart defects. *Ann Pediatr Cardiology*, 4(1):36–40, 2011.

[147] Johannes Patzelt, Juergen Schreieck, Estelle Camus, Meinrad Gawaz, Peter Seizer, and Harald F. Langer. Percutaneous mitral valve edge-to-edge repair using volume intracardiac echocardiography-first in human experience. *CASE*, 1(1):41 – 43, 2017.

[148] Olivier Pauly, Ben Glocker, Antonio Criminisi, Diana Mateus, Axel Möller, Stephan Nekolla, and Nassir Navab. Fast multiple organ detection and localization in whole-body mr dixon sequences. *Medical Image Computing and Computer-Assisted Intervention–MICCAI 2011*, pages 239–247, 2011.

[149] N J Pelc, R J Herfkens, A Shimakawa, and D R Enzmann. Phase contrast cine magnetic resonance imaging. *Magnetic Resonance Quarterly*, 7(4):229–254, 1991.

[150] Caroline Petitjean and Jean-Nicolas Dacher. A review of segmentation methods in short axis cardiac mr images. *Medical image analysis*, 15(2):169–184, 2011.

[151] Kristóf Ralovich, Razvan Ionasec, Viorel Mihalef, Puneet Sharma, Bogdan Georgescu, Allen Everett, Nassir Navab, and Dorin Comaniciu. Computational fluid dynamics framework for large-scale simulation in pediatric cardiology. pages 97–106, 2012.

[152] Kristóf Ralovich, Lucian Itu, Viorel Mihalef, Puneet Sharma, Razvan Ionasec, Dime Vitanovski, Allen Everett, Waldemar Krawtschuk, Suehling Michael, Nassir Navab, and Dorin Comaniciu. Non-invasive assessment of aortic coarctation through blood flow computation and mri. In *VPH2012: Integrative approaches to computational biomedicine - The Virtual Physiological Human Initiative Scientific Sessions 2012*. 2012.

[153] Kristóf Ralovich, Lucian Itu, Viorel Mihalef, Puneet Sharma, Razvan Ionasec, Dime Vitanovski, Waldemar Krawtschuk, Allen Everett, Richard Ringel, Nassir Navab, and Dorin Comaniciu. Hemodynamic assessment of pre- and post-operative aortic coarctation from mr images. In *Medical Image Computing and Computer-Assisted Intervention - MICCAI 2012*, pages 486–493. Springer, 2012.

[154] Kristóf Ralovich, Lucian Itu, Dime Vitanovski, Puneet Sharma, Razvan Ionasec, Viorel Mihalef, Waldemar Krawtschuk, Yefeng Zheng, Allen Everett, Giacomo Pongiglione, Benedetta Leonardi, Richard Ringel, Nassir Navab, Tobias Heimann, and Dorin Comaniciu. Non-invasive hemodynamic assessment, treatment outcome prediction and follow-up of aortic coarctation from mr imaging. 2014.

[155] Kristóf Ralovich, Matthias John, Estelle Camus, Nassir Navab, and Tobias Heimann. 6dof catheter detection, application to intracardiac echocardiography. In *Medical Image Computing and Computer-Assisted Intervention–MICCAI 2014*, pages 635–642. Springer International Publishing, 2014.

[156] Kristóf Ralovich, Viorel Mihalef, Puneet Sharma, Lucian Itu, Dime Vitanovski, Razvan Ionasec, Suehling Michael, Allen Everett, Giacomo Pongiglione, Nassir Navab, and Dorin Comaniciu. Modeling and simulation framework for hemodynamic assessment of aortic coarctation patients. In *ISMRM '12: Proceedings of the 20th Scientific Meeting and Exhibition of International Society for Magnetic Resonance in Medicine*. International Society for Magnetic Resonance in Medicine, 2118 Milvia Street, Berkeley, USA, 2012.

[157] Nils Raschke. Figure of windkessel effect. `http://www.biologieunterricht.info/_Media/preview_tafelbild_wk.jpg`, 2009. Accessed: 2014-07-19.

[158] Reza Razavi, Derek LG Hill, Stephen F Keevil, Marc E Miquel, Vivek Muthurangu, Sanjeet Hegde, Kawal Rhode, Michael Barnett, Joop van Vaals, David J Hawkes, and Edward Baker. Cardiac catheterisation guided by MRI in children and adults with congenital heart disease. *The Lancet*, 362(9399):1877 – 1882, 2003.

[159] Mansour Razminia, Atul Trivedi, Janos Molnar, Monther Elbzour, Mayra Guerrero, Yasser Salem, Aziz Ahmed, Sandeep Khosla, and David L Lubell. Validation of a new formula for mean arterial pressure calculation: the new formula is superior to the standard formula. *Catheterization and cardiovascular interventions official journal of the Society for Cardiac Angiography Interventions*, 63(4):419–425, 2004.

[160] Philippe Reymond, Yvette Bohraus, Fabienne Perren, Francois Lazeyras, and Nikos Stergiopulos. Validation of a patient-specific one-dimensional model of the systemic arterial tree. *American Journal of Physiology-Heart and Circulatory Physiology*, 301(3):H1173–H1182, 2011.

[161] Yoram Richter and Elazer R. Edelman. Cardiology is flow. *Circulation*, 113(23):2679–2682, 2006.

[162] Richard E Ringel. Covered cheatham platinum cp stents for the prevention or treatment of aortic wall injury associated with coarctation of the aorta COAST II, 2010. [Accessed Feb. 22, 2012].

[163] Richard E Ringel and Kathy Jenkins. Coarctation Of the Aorta Stent Trial (COAST), 2007. [Accessed Mar. 10, 2011].

[164] Günter Rote. Computing the minimum hausdorff distance between two point sets on a line under translation. *Information Processing Letters*, 38(3):123–127, 1991.

[165] V Rubio-Alvarez, R Limon, and J Soni. [intracardiac valvulotomy by means of a catheter.]. *Archivos del Instituto de Cardiologia de Mexico*, 23(2):183–192, 1953.

[166] Wilhelm Conrad Röntgen. Über eine neue art von strahlen: Vorläufige mittheilung. *Aus den Sitzungsberichten der Würzburger Physik.-medic. Gesellschaft*, 1895.

[167] Nashef SA, Roques F, Michel P, Gauducheau E, Lemeshow S, and Salamon R. European system for cardiac operative risk evaluation (euroscore). *Eur J Cardiothorac Surg*, 16(1):9–13, July 1999.

[168] Deeb N Salem, Patrick T O'Gara, Christopher Madias, and Stephen G Pauker. Valvular and structural heart disease: American college of chest physicians evidence-based clinical practice guidelines. *CHEST Journal*, 133(6_suppl):593S–629S, 2008.

[169] Steven L Schwartz, Linda D Gillam, Andrew R Weintraub, Brenda W Sanzobrino, Jeffrey A Hirst, Tsui-Leih Hsu, John P Fisher, Gerald Marx, David Fulton, Raymond G McKay, et al. Intracardiac echocardiography in humans using a small-sized (6F), low frequency (12.5 mhz) ultrasound catheter methods, imaging planes and clinical experience. *Journal of the American College of Cardiology*, 21(1):189–198, 1993.

[170] Gerald Schweighofer and Axel Pinz. Globally optimal O(n) solution to the pnp problem for general camera models. In *BMVC*, pages 1–10, 2008.

[171] Boston Scientific. Figure of Watchman device. `http://www.bostonscientific.com/content/dam/bostonscientific/Rhythm%20Management/portfolio-group/WATCHMAN/WATCHMAN_HighRes_TransparentBackground.image.460.0.jpg`, 2009. Accessed: 2015-09-10.

[172] Joerg Seeburger, Michael Andrew Borger, Heinz Tschernich, Sergej Leontjev, David Holzhey, Thilo Noack, Joerg Ender, and Friedrich Wilhelm Mohr. Transapical beating heart mitral valve repair. *Circulation: Cardiovascular Interventions*, 3(6):611–612, 2010.

[173] Philipp Seegerer, Tommaso Mansi, Marie-Pierre Jolly, Dominik Neumann, Bogdan Georgescu, Ali Kamen, Elham Kayvanpour, Ali Amr, Farbod Sedaghat-Hamedani, Jan Haas, et al. Estimation of regional electrical properties of the

heart from 12-lead ecg and images. In *International Workshop on Statistical Atlases and Computational Models of the Heart*, pages 204–212. Springer, Cham, 2014.

[174] Puneet Sharma, Lucian Itu, Xudong Zheng, Ali Kamen, Dominik Bernhardt, Constantin Suciu, and Dorin Comaniciu. A framework for personalization of coronary flow computations during rest and hyperemia. In *Engineering in Medicine and Biology Society (EMBC), 2012 Annual International Conference of the IEEE*, pages 6665–6668. IEEE, 2012.

[175] Frank E. Silvestry, Mitul B. Kadakia, Judi Willhide, and Howard C. Herrmann. Initial experience with a novel real-time three-dimensional intracardiac ultrasound system to guide percutaneous cardiac structural interventions: A phase 1 feasibility study of volume intracardiac echocardiography in the assessment of patients with structural heart disease undergoing percutaneous transcatheter therapy. *Journal of the American Society of Echocardiography*, 27(9):978 – 983, 2014.

[176] Gregory M Soares and Timothy P Murphy. Clinical interventional radiology: parallels with the evolution of general surgery. In *Seminars in interventional radiology*, volume 22, pages 10–14. Copyright© 2005 by Thieme Medical Publishers, Inc., 333 Seventh Avenue, New York, NY 10001, USA., 2005.

[177] Michal Sofka, Kristóf Ralovich, Neil Birkbeck, Jigndan Zhang, and S.Kevin Zhou. Integrated detection network (idn) for pose and boundary estimation in medical images. In *Proceedings of the 8th International Symposium on Biomedical Imaging (ISBI 2011)*, Chicago, IL, 30 Mar – 2 Apr 2011.

[178] Michal Sofka, Jingdan Zhang, Sara Good, S. Kevin Zhou, and Dorin Comaniciu. Automatic detection and measurement of structures in fetal head ultrasound volumes using sequential estimation and integrated detection network (IDN). *IEEE Transactions on Medical Imaging*, 33(5):1054–1070, May 2014.

[179] Milan Sonka, J Michael Fitzpatrick, and Barry R Masters. Handbook of medical imaging, volume 2: Medical image processing and analysis. *Optics & Photonics News*, 13:50–51, 2002.

[180] Frederick G. St. Goar, James I. Fann, Jan Komtebedde, Elyse Foster, Mehmet C. Oz, Thomas J. Fogarty, Ted Feldman, and Peter C. Block. Endovascular edge-to-edge mitral valve repair. *Circulation*, 108(16):1990–1993, 2003.

[181] Brooke N Steele, Jing Wan, Joy P Ku, Thomas JR Hughes, and Charles A Taylor. In vivo validation of a one-dimensional finite-element method for predicting blood flow in cardiovascular bypass grafts. *Biomedical Engineering, IEEE Transactions on*, 50(6):649–656, 2003.

[182] Mikkel B Stegmann and David Delgado Gomez. A brief introduction to statistical shape analysis. *Informatics and mathematical modelling, Technical University of Denmark, DTU*, 15(11), 2002.

[183] Daniel H Steinberg, Stephan Staubach, Jennifer Franke, and Horst Sievert. Defining structural heart disease in the adult patient: current scope, inherent challenges and future directions. *European Heart Journal Supplements*, 12(suppl E):E2–E9, 2010.

[184] N Stergiopulos, DF Young, and TR Rogge. Computer simulation of arterial flow with applications to arterial and aortic stenoses. *Journal of biomechanics*, 25(12):1477–1488, 1992.

[185] Qi Sun, Alexandra Groth, and Til Aach. Comprehensive validation of computational fluid dynamics simulations of in-vivo blood flow in patient-specific cerebral aneurysms. *Medical Physics*, 39(2):742–754, 2012.

[186] Yiyong Sun, Samuel Kadoury, Yong Li, Matthias John, Jeff Resnick, Gerry Plambeck, Rui Liao, Frank Sauer, and Chenyang Xu. Image guidance of intracardiac ultrasound with fusion of pre-operative images. In Nicholas Ayache, Sébastien Ourselin, and Anthony Maeder, editors, *Medical Image Computing and Computer-Assisted Intervention MICCAI 2007*, volume 4791 of *Lecture Notes in Computer Science*, pages 60–67. Springer Berlin Heidelberg, 2007.

[187] Kartik S. Sundareswaran, Diane de Zelicourt, Shiva Sharma, Kirk R. Kanter, Thomas L. Spray, Jarek Rossignac, Fotis Sotiropoulos, Mark A. Fogel, and Ajit P. Yoganathan. Correction of pulmonary arteriovenous malformation using image-based surgical planning. *J Am Coll Cardiol Img*, 2(8):1024–1030, 2009.

[188] Thomas M Tadros, Michael D Klein, and Oz M Shapira. Ascending aortic dilatation associated with bicuspid aortic valve. *Circulation*, 119(6):880–890, 2009.

[189] David Tanous, Lee N Benson, and Eric M Horlick. Coarctation of the aorta: evaluation and management. *Current Opinion in Cardiology*, 24, 2009.

[190] Charles A. Taylor, Mary T. Draney, Joy P. Ku, David Parker, Brooke N. Steele, Ken Wang, and Christopher K. Zarins. Predictive medicine: Computational techniques in therapeutic decision-making. *Computer Aided Surgery*, 4(5):231–247, 1999.

[191] Charles A Taylor, Timothy A Fonte, and James K Min. Computational fluid dynamics applied to cardiac computed tomography for noninvasive quantification of fractional flow reserve. *Journal of the American College of Cardiology*, 61(22):2233–2241, 2013.

[192] B D Thanopoulos, L Hadjinikolaou, G N Konstadopoulou, G S Tsaousis, F Triposkiadis, and P Spirou. Stent treatment for coarctation of the aorta: intermediate term follow up and technical considerations. *Heart*, 84(1):65–70, 2000.

[193] Zhuowen Tu. Probabilistic boosting-tree: learning discriminative models for classification, recognition, and clustering. In *ICCV 2005*, volume 2, pages 1589–1596. IEEE.

[194] Shinji Umeyama. Least-squares estimation of transformation parameters between two point patterns. *IEEE Transactions on pattern analysis and machine intelligence*, 13(4):376–380, 1991.

[195] Israel Valverde, Cristina Staicu, Heynric Grotenhuis, Alberto Marzo, Kawal Rhode, Yubing Shi, Alistair Brown, Aphrodite Tzifa, Tarique Hussain, Gerald Greil, Patricia Lawford, Reza Razavi, Rod Hose, and Philipp Beerbaum. Predicting hemodynamics in native and residual coarctation: preliminary results of a rigid-wall computational-fluid-dynamics model (rw-cfd) validated against clinically invasive pressure measures at rest and during pharmacological stress. *Journal of Cardiovascular Magnetic Resonance*, 13:1–4, 2011. 10.1186/1532-429X-13-S1-P49.

[196] Bas L van der Hoeven, Martin J Schalij, and Victoria Delgado. Multimodality imaging in interventional cardiology. *Nature Reviews Cardiology*, 9(6):333–346, 2012.

[197] IE Vignon-Clementel, CA Figueroa, KE Jansen, and CA Taylor. Outflow boundary conditions for 3d simulations of non-periodic blood flow and pressure fields in deformable arteries. *Computer methods in biomechanics and biomedical engineering*, 13(5):625–640, 2010.

[198] P. Viola and M. Jones. Rapid object detection using a boosted cascade of simple features. In *Proceedings of the 2001 IEEE Computer Society Conference on Computer Vision and Pattern Recognition. CVPR 2001*, volume 1, pages I–511–I–518 vol.1, 2001.

[199] D. Vitanovski, K. Ralovich, R. Ionasec, Yefeng Zheng, M. Suehling, W. Krawtschuk, J. Hornegger, and D. Comaniciu. Personalized learning-based segmentation of thoracic aorta and main branches for diagnosis and treatment planning. In *Biomedical Imaging (ISBI), 2012 9th IEEE International Symposium on*, pages 836–839, May 2012.

[200] Ingmar Voigt, Tommaso Mansi, Razvan Ioan Ionasec, Etienne Assoumou Mengue, Helene Houle, Bogdan Georgescu, Joachim Hornegger, and Dorin Comaniciu. Robust physically-constrained modeling of the mitral valve and subvalvular apparatus. In *International Conference on Medical Image Computing*

and Computer-Assisted Intervention, pages 504–511. Springer Berlin Heidelberg, 2011.

[201] Ingmar Voigt, Mihai Scutaru, Tommaso Mansi, Bogdan Georgescu, Noha El-Zehiry, Helene Houle, and Dorin Comaniciu. Robust live tracking of mitral valve annulus for minimally-invasive intervention guidance. In *International Conference on Medical Image Computing and Computer-Assisted Intervention*, pages 439–446. Springer, 2015.

[202] Joris W.J. Vriend and Barbara J.M. Mulder. Late complications in patients after repair of aortic coarctation: implications for management. *International journal of cardiology*, 101:399–406, June 2005.

[203] Christian Wachinger, Wolfgang Wein, and Nassir Navab. Three-dimensional ultrasound mosaicing. In *International Conference on Medical Image Computing and Computer-Assisted Intervention (MICCAI)*, Brisbane, Australia, October 2007.

[204] Peng Wang, Terrence Chen, Olivier Ecabert, Simone Prummer, Martin Ostermeier, and Dorin Comaniciu. Image-based device tracking for the co-registration of angiography and intravascular ultrasound images. In *MICCAI 2011*, pages 161–168. 2011.

[205] Shijun Wang and Ronald M. Summers. Machine learning and radiology. *Medical Image Analysis*, 16(5):933 – 951, 2012.

[206] Biosense Webster. Cartosound module soundstar catheter, February 2014.

[207] Walter C Willett, Jeffrey P Koplan, Rachel Nugent, Courtenay Dusenbury, Pekka Puska, and Thomas A Gaziano. Prevention of chronic disease by means of diet and lifestyle changes. 2006.

[208] Walter T Wilser, Stephen R Barnes, and Lex Garbini. Helical acoustic array for medical ultrasound, May 28 2013. US Patent 8,449,467.

[209] Dijia Wu, Michal Sofka, Neil Birkbeck, and S Kevin Zhou. Segmentation of multiple knee bones from ct for orthopedic knee surgery planning. In *International Conference on Medical Image Computing and Computer-Assisted Intervention*, pages 372–380. Springer, 2014.

[210] Pradeep K. Yadav, David R. Holmes, Sharif A. Halim, John P. Vavalle, and Michael J. Mack. Training in structural heart interventions. *Journal of the American College of Cardiology*, 64(21):2296–2298, 2014.

[211] Lin Yang, Bogdan Georgescu, Yefeng Zheng, Yang Wang, Peter Meer, and Dorin Comaniciu. Prediction based collaborative trackers (pct): A robust and

accurate approach toward 3d medical object tracking. *IEEE transactions on medical imaging*, 30(11):1921–1932, 2011.

[212] Z. Yefeng, Barbu A., Georgescu B., Scheuering M., and Comaniciu D. Four-chamber heart modeling and automatic segmentation for 3-d cardiac ct volumes using marginal space learning and steerable features. *IEEE Transactions on Medical Imaging*, 27(11):1668–1681, Nov. 2008.

[213] M Zamir, P Sinclair, and T H Wonnacott. Relation between diameter and flow in major branches of the arch of the aorta. *Journal of Biomechanics*, 25(11):1303–1310, 1992.

[214] F. Zhao and et al. Automated 4d segmentation of aortic magnetic resonance images. In *The 17th British Machine Vision Association*, volume 1, pages 247–257, September 2006.

[215] Y. Zheng. *Marginal Space Learning for Medical Image Analysis: Efficient Detection and Segmentation of Anatomical Structures*. SpringerLink : Bücher. Springer, 2014.

[216] Yefeng Zheng, Matthias John, Rui Liao, Jan Boese, Uwe Kirschstein, Bogdan Georgescu, S. Kevin Zhou, Jörg Kempfert, Thomas Walther, Gernot Brockmann, and Dorin Comaniciu. Automatic aorta segmentation and valve landmark detection in c-arm ct: application to aortic valve implantation. In *Proceedings of the 13th international conference on Medical image computing and computer-assisted intervention: Part I*, pages 476–483, Berlin, Heidelberg, 2010. Springer-Verlag.

[217] Yefeng Zheng, David Liu, Bogdan Georgescu, Hien Nguyen, and Dorin Comaniciu. 3d deep learning for efficient and robust landmark detection in volumetric data. In *International Conference on Medical Image Computing and Computer-Assisted Intervention*, pages 565–572. Springer, 2015.

[218] Yinqiang Zheng, Yubin Kuang, Shigeki Sugimoto, Kalle Åström, and Masatoshi Okutomi. Revisiting the pnp problem: A fast, general and optimal solution. In *Computer Vision (ICCV), 2013 IEEE International Conference on*, pages 2344–2351. IEEE, 2013.

[219] Shaohua Kevin Zhou, Jinghao Zhou, and Dorin Comaniciu. A boosting regression approach to medical anatomy detection. In *Computer Vision and Pattern Recognition, 2007. CVPR'07. IEEE Conference on*, pages 1–8. IEEE, 2007.

[220] Xiaowei Zhou, Can Yang, and Weichuan Yu. Automatic mitral leaflet tracking in echocardiography by outlier detection in the low-rank representation. In *Computer Vision and Pattern Recognition (CVPR), 2012 IEEE Conference on*, pages 972–979. IEEE, 2012.

Index

List of Figures

List of Tables

List of Algorithms